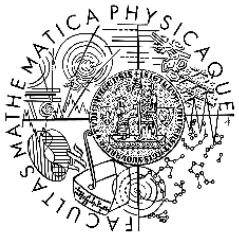

FACULTY
OF MATHEMATICS
AND PHYSICS
Charles University

DOCTORAL THESIS

Suren A. Ali-Ogly

LOW TEMPERATURE PLASMA AND NANOPARTICLES: EFFECTS OF GAS FLOW AND SURFACES

Department of Macromolecular Physics

Supervisor of the doctoral thesis: Mgr. Jaroslav Kousal, PhD.

Study programme: Physics

Specialization: F4 – Biophysics, Chemical and Macromolecular Physics

Prague 2023

I declare that I carried out this doctoral thesis independently, and only with the cited sources, literature and other professional sources.

I understand that my work relates to the rights and obligations under the Act No. 121/2000 Coll., the Copyright Act, as amended, in particular the fact that the Charles University has the right to conclude a license agreement on the use of this work as a school work pursuant to Section 60 paragraph 1 of the Copyright Act.

In Prague, data.....

signature

Acknowledgements

I would like to express my deepest gratitude to my parents, Andrei Khizirovich and Tatiana Vladimirovna, for their unwavering love, support, and patience throughout my academic journey. I am also grateful to my brothers, Egor, Ilia, and Tigran, for their emotional support and encouragement during my studies.

I extend my sincere appreciation to my colleagues Mgr. Pavel Pleskunov PhD., Mgr. Daniil Nikitin PhD., and Mgr. Zdenek Krtouš for their valuable insights, guidance, and for sharing their experiences with me. I am also thankful to Kateryna Biliak, Mariia Protsak, Natalia Khomiakova, Vladislav Ivaniuzhenkov, Marco Tosca, RNDr. Tereza Košutová, Anna Kuzminova, PhD., Ing. Vaidulych Mykhailo PhD, and RNDr. Hana Libenská for accompanying me on this research journey and providing emotional support.

I would like to express my gratitude to doc. Mgr. Jan Hanuš, Ph.D. and RNDr. Pavel Solař, Ph.D. for imparting their technical knowledge and skills, which significantly contributed to my growth as a researcher. Special thanks go to my supervisor, Mgr. Jaroslav Kousal, PhD., for his continuous guidance, professional support, and mentorship.

I am also deeply grateful to prof. Ing. Andrey Shukurov, Ph.D. and prof. RNDr. Hynek Biederman, DrSc., for their invaluable assistance in shaping and confining my research, as well as helping me navigate the complex world of academia.

I would like to extend my thanks to my endocrinologist, MUDr. Mária Petrusová, for her unwavering support and assistance during challenging times. Her encouragement helped me remain strong and focused on my goals.

Lastly, I am grateful to Bc. Veronika Červenková for providing the much-needed motivation and engaging in remarkable discussions during the final phases of my work. Her support was instrumental in the successful completion of my thesis.

Title: Low temperature plasma and nanoparticles: effects of gas flow and surfaces

Author: Ing. Suren A. Ali-Ogly, B.Eng

Department / Institute: Department of Macromolecular Physics / Charles University

Supervisor of the doctoral thesis: Mgr. Jaroslav Kousal, PhD, Department of Macromolecular Physics / Charles University

Abstract: This PhD thesis investigates the role of carrier gas flow in the magnetron-based gas aggregation cluster source and its impact on nanoparticle transportation. The research encompasses both theoretical and experimental aspects of low-temperature plasma interaction with surfaces and material engineering applications. Numerical models and computational fluid dynamics simulations are employed to understand the underlying physics of nanoparticles motion in gas aggregation cluster sources. The study demonstrates that carrier gas flow, particularly its velocity and inlet configuration, significantly influences the nanoparticles trap region and their residence time in the plasma. Brownian diffusion is identified as a critical factor affecting the spatial behaviour of NPs, contributing to both their escape and loss in gas aggregation cluster sources. The deposition of thin films using magnetron sputtering of PLA, a promising polymer material, is shown to facilitate nanoparticle adhesion. This research enhances our understanding of non-electromagnetic aspects of nanoparticles behaviour in gas aggregation cluster sources, highlighting the value of computational fluid dynamics in optimising carrier gas flow performance in magnetron-based gas aggregation cluster source systems.

Keywords: low-temperature plasma, nanoparticles, gas flow, magnetron-based gas aggregation cluster source, computational fluid dynamics, CFD, optimisation

Název práce: Nízkoteplotní plazma a nanočástice: vliv efektu proudění a povrchu

Autor: Ing. Suren A. Ali-Ogly, B.Eng.

Katedra / Ústav: Katedra Makromolekulární Fyziky / Univerzita Karlova

Vedoucí doktorské práce: Mgr. Jaroslav Kousal, PhD.

Abstrakt: Tato doktorská práce se zabývá rolí proudu plynu v plynovém agregačním zdroji nanočástic založeném na magnetronu a jeho vlivu na transport nanočástic. Výzkum zahrnuje teoretické i experimentální aspekty interakce nízkoteplotního plazmatu s povrchy a aplikace v materiálovém inženýrství. Numerické modely a simulace výpočetní dynamiky tekutin se používají k porozumění základním fyzikálním principům pohybu nanočástic v agregačním zdroji nanočástic. Studie ukazuje, že proud nosného plynu, zejména jeho rychlost a konfigurace vstupu, významně ovlivňuje oblast záchytu nanočástic a jejich dobu setrvání v plazmatu. Brownovská difuze je identifikována jako kritický faktor ovlivňující prostorové chování nanočástic, což přispívá k jejich úniku i ztrátě v systému zdroje nanočástic. Je ukázán vliv depozice tenkých vrstev pomocí magnetronového naprašování PLA, slibného polymerního materiálu, na usnadnění adheze nanočástic. Tento výzkum rozšiřuje naše porozumění neelektromagnetickým aspektům chování nanočástic v agregačním zdroji nanočástic na bázi magnetronu a zdůrazňuje hodnotu simulace dynamiky tekutin pro optimalizaci proudění nosného plynu v agregačních zdrojích.

Klíčová slova: nízkoteplotní plazma, nanočástice, proud plynu, plynový agregační zdroj nanočástic, výpočetní dynamika tekutin, optimalizace

Table of Contents

Aims of Doctoral Thesis

This Doctoral thesis aims to investigate the phenomenon of the low-temperature plasma interaction with surfaces of various materials and how the processes may be controlled in order to be applicable in an industry-wide range. Several application methods of low-temperature plasma generation

and interaction with the object's surface were studied and experimented with. The main focus during the four years of PhD studies was on the investigation of nanoparticles' spatial behaviour in gas aggregation cluster sources with plasma-assisted vapour phase deposition. For the successful realisation of these aims, the following objectives were established:

- Identify processes that occur in plasma-surface interactions and find control parameters for such processes.
- Build numerical models for simulations of the physics of nanoparticles motion within the GAS, but not limited to GAS.

1. Introduction

Low-temperature plasma applications in material engineering have been explored since the first half of the 20th century, with applications ranging from direct surface treatment to generating new materials like plasma-polymers and nanoparticles (NPs). Although extensive research has been conducted in this field, many aspects still require further study and understanding. This work aims to contribute to our knowledge of plasma-assisted and plasma-based methods in material engineering.

The first part of this work, the theoretical section, focuses on plasma physics fundamentals and plasma-surface interaction processes. We will discuss the state-of-the-art in plasma-based material engineering and synthesis, specifically concentrating on methods and techniques used for generating plasma-polymers and nanoparticles.

The second part, the experimental section, presents the diagnostic methods employed during the research and describes the conducted experiments. Notably, it was observed during experiments with gas aggregation cluster sources (GAS) that inert gas flow significantly influenced NPs' motion. Understanding and visualizing gas flow is crucial for optimizing GAS performance.

The efficiency of NP embedding into plasma polymers strongly depends on GAS parameters. Based on previous studies, we hypothesized that the interaction of NPs with the substrate could be governed by their kinetic energy. Optimizing this energy is necessary to prevent NPs from rebounding off the substrate. Given the author's expertise in computational fluid dynamics (CFD) modelling, further experiments on Ag/PLA nanocomposites will be conducted by a collaborator during their PhD work, while the author investigates NP transport within and outside the GAS. This research will provide a deeper understanding of a problem that has not been extensively explored so far, focusing on the non-electromagnetic aspects of the phenomena and their influence on plasma-based material engineering.

1.1. Fundamentals of Plasma Physics

In popular culture, “Plasma” is often called a fourth state of matter, which goes after the gaseous state. This, whatsoever, is a misleading description, and the term Plasma describes a more complicated concept. According to Bittencourt [1], plasma is a macroscopic substance containing many interacting free-charged particles (electrons, ionized atoms or molecules) among neutral particles, which exhibit collective behaviour due to the long-range electromagnetic forces. However, be aware that not all media containing charged particles can be classified as plasma. For a media containing charged and neutral particles, specific criteria should be satisfied to be called Plasma. These criteria are derived from the following conditions:

1. Macroscopic neutrality (or quasi-neutrality) of a medium
2. Charged and neutral particles exhibit collective behaviour.
3. Stability of macroscopic space charge neutrality. Simply saying – collisions of charged particles with neutral particles over a fixed period.

In the absence of external disturbances, a plasma is macroscopically neutral. This means that under equilibrium conditions with no external forces present, in a volume of the plasma sufficiently large to contain a large number of particles and yet sufficiently small compared to the characteristic lengths for variation of macroscopic parameters such as density and temperature, the net resulting electric charge is zero. In the interior of this volume, i.e., plasma, the microscopic space charge fields cancel each other, and no net space charge exists over a macroscopic region.

Departures from macroscopic electrical neutrality can naturally occur only over distances in which a balance is obtained between the thermal particle energy, which tends to disturb the electrical neutrality, and the electrostatic potential energy resulting from any charge separation, which tends to restore the electrical neutrality. This distance is of the order of a characteristic length parameter of the plasma, called the Debye length. In the absence of external forces, the plasma cannot support departures from macroscopic neutrality over larger distances than this since the charged particles can move freely to neutralize any regions of excess space charge in response to the large coulomb forces that appear.

The Debye length is an important physical parameter for the description of a plasma. It provides a measure of the distance over which the influence of the electric field of an individual charged particle is felt by the other charged particles inside the plasma. The charged particles arrange themselves in such a way as to effectively shield any electrostatic fields within the order of the Debye length. This shielding of electrostatic fields is a consequence of the collective effects of the plasma particles. Calculation of the distance was first published by Debye in 1923 [2].

$$\lambda_D = \left(\frac{(\epsilon_0 \cdot kT)}{(n_e e^2)} \right)^{\frac{1}{2}} \quad (1)$$

Where $\lambda_D$is a Debye length, ϵ_0 is the permittivity of free vacuum, k Is the Boltzmann constant, T is the temperature, n_e is the electron number density, and e is the electron charge.

As mentioned before, the Debye length can also be regarded as a measure of the distance over which fluctuating electric potentials may appear in a plasma, corresponding to a conversion of the thermal particle kinetic energy into electrostatic potential energy.

When a boundary surface is introduced in a plasma, the perturbation produced extends only up to a distance of the order of λ_D from the surface. In the neighbourhood of any surface inside the plasma, there is a layer of a width of the order of λ_D, known as the plasma sheath, inside which the condition of macroscopic electrical neutrality may not be satisfied. Beyond the plasma sheath region, there is the plasma region, where macroscopic neutrality is maintained, or quasineutrality, i.e. $n_i \cong n_e$, where n_i is the number density of positively charged ions.

A criterion, for instance, for an ionized gas to be plasma, is that the plasma should be dense enough so that λ_D is much smaller than the characteristic length L (e.g. vacuum chamber)

$$\lambda_D \ll L \quad (2)$$

Debye shielding is valid only when there is a sufficient amount of charged particles in a given volume. If only two charged particles are in the sheath region, Debye shielding would not be a statistically valid concept [3]. In order for the ionized

volume inside the "Debye sphere" (with a radius equal to λ_D) to be called plasma it should, therefore, satisfy the criterion to maintain a collective behaviour:

$$n_e \lambda_D^3 \gg 1 \tag{3}$$

Another important plasma property is the stability of its macroscopic space charge neutrality. When a plasma is instantaneously disturbed from the equilibrium condition, the resulting internal space-charge fields give rise to collective particle motions that tend to restore the original charge neutrality. These collective motions are characterized by a natural oscillation frequency known as the *plasma frequency.* Since these collective oscillations are high-frequency oscillations, the ions, because of their heavy mass, are, to a certain extent, unable to follow the motion of the electrons. The electrons oscillate collectively about the heavy ions, the necessary collective restoring force being provided by the ion-electron coulomb attraction. [1]. The angular frequency of electron collective oscillation, also called *plasma frequency,* is given by:

$$\omega = \left(\frac{n_e e^2}{m_e \epsilon_0} \right)^{0.5} \tag{4}$$

Collisions between electrons and neutral particles have a damping effect on plasma frequency. If the electron-neutral collision frequency is ν_{ne}, then it should be smaller than the electron plasma frequency $\nu_{pe}\left(¿ \frac{\omega}{2\pi} \right)$. Otherwise, due to frequent collisions with neutrals, electrons will be influenced mainly by neutral particle motion. Therefore, a medium can be treated as a neutral gas.

$$\nu_{pe} > \nu_{ne} \tag{5}$$

From the statement above, we may derive the third and final criterion. If τ represents the average time an electron travels between collision with neutrals ($\tau = 1/\nu_{ne}$), then this average time τ must be large enough compared to the characteristic time during which physical plasma parameters change. Mathematically it can be interpreted as the following equation.

$$\omega\tau > 1 \tag{6}$$

Another important plasma property that is essential for this work is plasma temperature. One must be careful with the term “temperature” when discussing plasma. For example, ordinary fluids in thermal equilibrium have atoms’ velocity distributed with Maxwell-Gaussian distribution [4].

$$f(v) = A e^{\frac{-0.5 m v^2}{kT}} \tag{7}$$

Where A is a normalisation factor.

A temperature, then, in this case, determines the width of the distribution. In a weakly ionized plasma, where appears one charged particle per 10^6 neutral particles [5], the electron may have a temperature of 10 000 °K. In contrast, neutral particles may stay at a much lower room temperature, and ions as well may have a different temperature than electrons and neutrals. In low pressure, electrons, ions, and neutrals may move and collide with each other. Still, due to the low concentration of particles in a volume, their collision is infrequent to equalize the temperatures. However, each species collides with its kind more frequently and may have a Maxwell-Gaussian distribution. This is an essential characterisation parameter for what is usually referred to as a Low-Temperature plasma. Contrarily, species may fail to form a Maxwell-Gaussian distribution for each species in a very hot plasma and can be treated by kinetic theory.

For better observation, for example, interstellar plasma may have a Debye length varying in tens of meters while having temperature being around $10^1 - 10^4$ K, and electron number density being as low $10^{-4} m^{-3}$ with plasma frequency between $10^4 - 10^8 rad/s$. Whereas in thermonuclear plasma, Debye length is much shorter that could be as low as 10^{-6}m, but at a higher temperature around $10^5 - 10^8$ K and electron number density between $10^{18} - 10^{22} m^{-3}$, with plasma frequency being as high as $10^{12} rad/s$. [1], [6]–[8].

So, it can be stated that plasma may come in different “shapes and forms”, mainly described by electron number density n_e and thermal energy KT_e. Therefore, the application of plasma utilizes an extensive range of n and KT_e.

The earliest work with plasmas was that of Langmuir, Tonks, and their collaborators in the 1920s. This research was inspired by the need to develop vacuum tubes that could carry large currents and therefore had to be filled with ionized gases. The

research was done with weakly ionized glow discharges and positive columns, typically with KTe = 2 eV and $10^{14} < n < 10^{18}$ m^{-3}. It was here that the shielding phenomenon was discovered; the sheath surrounding an electrode could be seen visually as a dark layer. Gas discharges were encountered in mercury rectifiers, hydrogen thyratrons, ignitrons, spark gaps, welding arcs, neon and fluorescent lights, and lightning discharges.

For instance, plasma is used to control thermonuclear fusion reactions for power generation. In short, the fusion of two light nuclei forms a single heavier nucleus whose mass will be less than the total initial mass. The mass difference is then appearing as a tremendous amount of energy (according to Einstein's law $E=mc^2$, where c is the speed of light). To control the fusion, it is required to generate a plasma with very high temperatures ($KT_e > 10\,keV$) to hold particles together long enough for fusion reactions to take place. A high temperature is required to generate sufficient kinetic energy (from thermal energy), so two positively charged nuclei can overcome the electrostatic coulomb repulsion.

Another intriguing plasma physics utilisation is studying the earth's environment in space, for instance, the effect of solar wind on earth's magnetosphere. However, it is not limited only to our planet. Since plasma is a big part of interstellar and interplanetary space, plasma physics plays a vital role in astrophysics.

Plasma can also be used as propulsion of a rocket engine. The plasma rocket engine is accomplished by having electric and magnetic fields applied perpendicular to each other. Due to Lorenz's force, plasma can be accelerated out of the rocket. Although the net force is small compared to chemical propulsion systems, the plasma propulsion system can consistently produce thrust over a long period, which is a good fit for interplanetary space travel.

Our group (Macromolecular Physics department of Charles University) utilizes plasma to interact with surfaces for material engineering, i.e. surface modification, sputtering, thin layer deposition, and creation of new materials such as plasma polymers and nanoparticle clusters. This work will primarily focus on these phenomena and their subsequent challenges.

1.2. Physics of Plasma-Surface Interaction

Plasma consists of electrons, positive and negative ions, neutrals, radicals, metastables, and all of them, in one way or another, interact with solid surfaces (but are not limited to solid) surrounding plasma. Such surfaces are usually walls, substrates, targets etc. Many underlying processes of plasma-surface interaction are still not thoroughly examined and precisely described, therefore, research in this field continues nowadays [9]. Figure 1 shows a simplified overview of the interaction between plasma species and bulk surface material. Figure 2 shows the most significant energetic particle–solid interactions that control the properties of thin films deposited from particles within the energy range relevant for thin-film deposition. Plasma-Surface interactions include effects such as chemical removal, sputtering (both processes of surface etching), physical deposition, chemical bonding, surface heating due to ion and electron bombardment, evaporation due to heating, surface atoms excitation, surface activation, structural rearrangement in bulk material, surface particles recombination, and ion implantation.

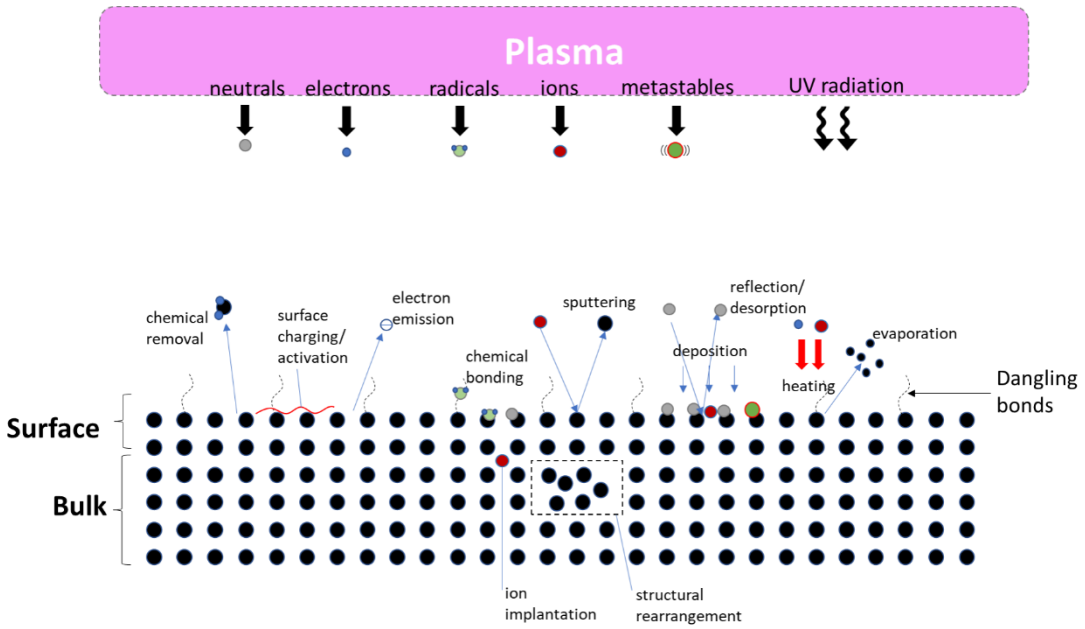

Figure 1. Simplified schematic illustration of Plasma-Surface interaction

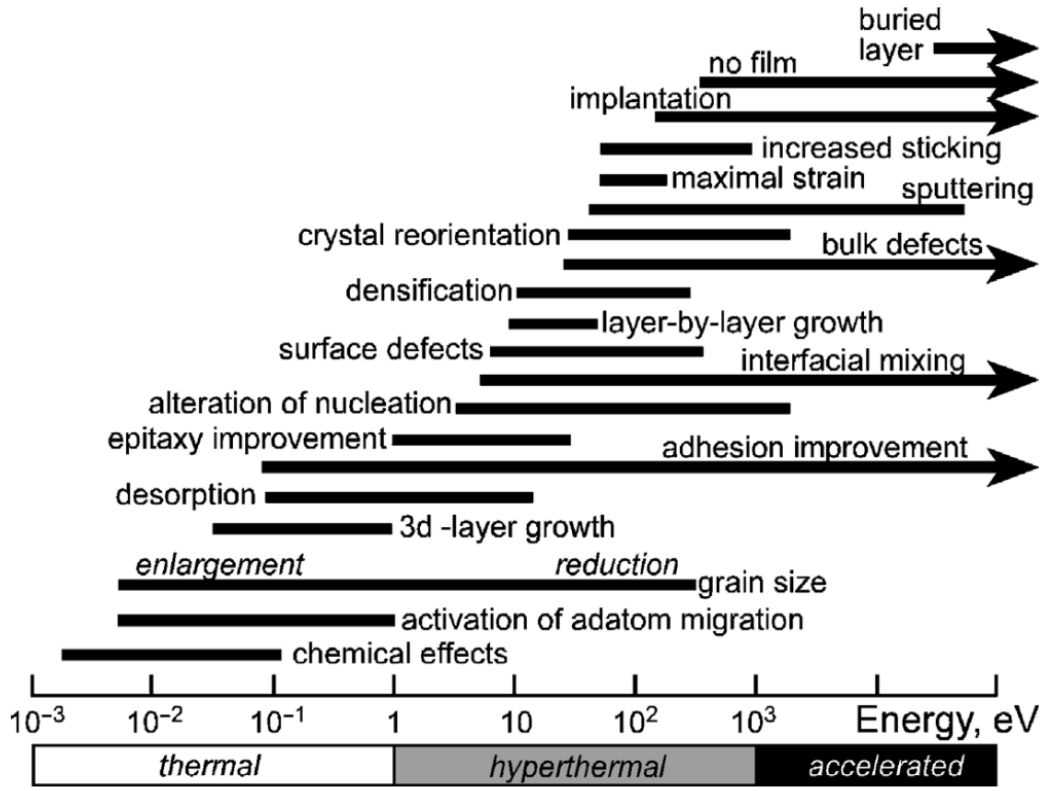

Figure 2. Energy ranges for particle-solid interactions that most significantly influence the thin film properties. Adopted from ref. [10]

Sputtering

Ion bombardment of the solid surfaces leads to the erosion of the aforementioned surfaces, and this event is usually referred to as sputtering. It is important to note that not only does ion bombardment of the surfaces lead to a sputtering, but any kind of particles, including electrons and photons (for certain classes of material), may lead to erosion, although the efficiency and sputtering yield values greatly vary. Sputtering can be analytically described by the binary collision approximation (BCA) model. Unlike evaporation, particles formerly bound to a solid in BCA are unbounded by direct projectile impingement (*direct knock-on*) or by transferred kinetic energy from other atoms due to a series of collisions (*collision cascade*) originated by the projectile. The interaction between projectile ions (or particles in general) gives rise to two processes, *kinetic* and *potential processes*. Whereas kinetic generally describes energy and momentum exchange, and as for potential, there exist various modes for interaction potential. For interaction potential, there is *repulsive potential* (dominated by Coulomb force in small internuclear separation) that is also screened by surrounding electrons, and there is *attractive potential* that exists in stable molecules

at certain intermediate internuclear distances [9], [11], [12] [13] [14], [15] [16]. The ratio between the number of sputtered atoms to the number of incident ions defines sputtering yield.

$$Y\left(E_0\right)=\frac{N_{sputterd\ atoms}}{N_{incident\ ions}} \tag{8}$$

Chemical removal

It is important to distinguish concepts of physical and chemical sputtering. The former category invokes a transfer of kinetic energy from the incident particle to target atoms and subsequent ejection of those atoms through the target surface, which have acquired enough kinetic energy to overcome the binding forces exerted by the target. The latter category invokes a chemical reaction induced by the impinging particles, producing an unstable compound at the target surface. [11] [17]

Ion implantation

If the projectile ion is fast enough (has sufficient kinetic energy), it can deposit on the solid surface, or the ion can implant into the solid. The range of the incident projectile in the solid strongly depends on incident kinetic energy. Since the deceleration of the ion, due to nuclear and electron stopping power, in the matter is not happening in a straight line, there are usually two quantities used to describe ion implantation. Mean projected range (along incident direction), spread (transverse distribution), depth (normal to mean surface level). Ion impanation in solids can be predicted via the Transport of Ions in Matter (TRIM) code. [9], [18], [19]

Backscattering of ions

At low incident energies, ions may escape deposition or implantation and backscatter from the surface. Analogically to sputtering yield, there exists a backscattering parameter called the reflection parameter. The reflection parameter is defined by a ratio of the number of reflected particles to the number of incident particles. At low energy, impingement ions can not overcome the repulsive part of interaction potential, which prevents the ion from entering the solid. [9], [20]–[22].

$$R\left(E_0,\theta_{inc}\right)=\frac{N_{reflected}}{N_{incident}} \tag{9}$$

Electron emission

Interaction of some plasma species (neutrals, ions, electrons) that are of sufficient energy with solid surfaces may, among other effects, provoke an emission of electrons. This process leads to the ejection of electrons of surface atoms. Similarly to sputtering, the process leading the electron ejection can be divided into kinetic and *potential processes*. The potential emission results from the Auger-type transition at the surface involving band electrons that are transferred to high-lying vacant states of the projectile. The potential emission is restricted particles carrying large potential energy into a collision and to atomic particles which are either ionized or excited [9].

Electron emission via the kinetic process is done in three stages [23]:

1. projectile interaction with electrons of the solid creating freely mobile excited electrons
2. migration of some excited electrons to the surface
3. some of the electrons escape through the potential barrier at the surface.

Electron emission may appear due to electron impact (also secondary electron emission), or impacted electron may be reflected (backscattered) or due to the impact of ions or clusters.

Deposition – Adsorption, diffusion

Particles from the plasma (gas phase) when losing sufficiently enough energy bound at the surface. The bonds are usually of electromagnetic nature. In general, adsorption can be divided into two major categories: physisorption and chemisorption. When the noble gas is attached to the metal surface at low temperature by van der Waals interaction, it is referred to as physisorption. Conversely, chemisorption is bound by the valence forces of the exchanging electronic orbitals of adsorbed particles and substrate surface atoms, e.g., CO, on metals. Differences between physisorption and chemisorption can also be described in terms of the amount of released adsorption energy E_{ads}. Typical physisorption takes place for $E_{ads}<0.5\,eV$, whereas chemisorption is usually $E_{ads}>0.5\,eV$, i.e., chemisorption forms a stronger bond between adsorbed particles and the surface. In addition, the impinging molecules can also dissociate while approaching the substrate surface, and only fragments of the original molecule may be adsorbed. This process is referred to as dissociative

chemisorption. An example of such a process is the passivation of metals by hydrogen molecules [9]. Factors that determine which process will occur are usually: the energy of the incoming particle, the incident angle of that particle, degree of coverage (ratio of the density of adsorbed particles on the surface to the available surface density of the substrate, or if simplified vacant sites in the surface).

Physiosorbed particles, while on the surface, may diffuse towards stronger bonds on the surface. The main factors responsible for the migration of the particles on the surface are the crystal structure and chemical composition of the substrate.

Desorption

Adsorbed particles may leave the surface after some time (residence time). Desorption energy is transferred by the lattice due to thermal desorption or by collisions with other energetic particles. For thermal desorption, the main factor of influence is the substrate surface temperature. In contrast, the collisional desorption's residence time mostly depends on the flux of the energetic particles and characteristic cross-section (collision cross-section).

Reflection and Excitation

If the energy of an incoming particle is insufficient for the sputtering or implantation but at the same time is too high for the adsorption to occur, then the particle will be reflected. In this case, we talk about an elastic collision, which subsequently will heat the surface until the thermal equilibrium between the solid surface and the gas phase[24].

However, for hot surfaces, the energy transport is incomplete. For diatomic or polyatomic molecules, the energy transfer also involves the excitation of vibrational and rotational modes.

Activation

Bombarding the surface by energetic particles can induce a collision cascade in the lattice of the substrate's surface. This will then lead to breaking chemical bonds with neighbouring atoms, generating dangling bonds on the surface. Dangling bonds are likely to react with the incoming particles to form a strong bond. Hence, the surface reactivity is increased substantially with activation processes on the surface.[9], [24]

1.3. Plasma Polymerisation

One of the methods of plasma-based material engineering is the creation and utilisation of plasma polymers. Plasma polymers, which consist of intricately interconnected (cross-linked) and extensively ramified monomer networks (refer to Figure 3), which are synthesized from the fragmentation of gaseous precursor under the low temperature plasma influence. are created through the fragmentation of gaseous precursors under the impact of low-temperature plasma. The first intentional studies of plasma polymerization were carried out in the 1950s [25], [26]. In the latter half of the 20th century, there was a surge in scientific curiosity surrounding plasma polymers and the associated polymerization mechanisms. A comprehensive overview of plasma polymerization processes, including research and historical context, can be found in[5], [27]–[29]. In this context, we will provide just a concise explanation of the idea.

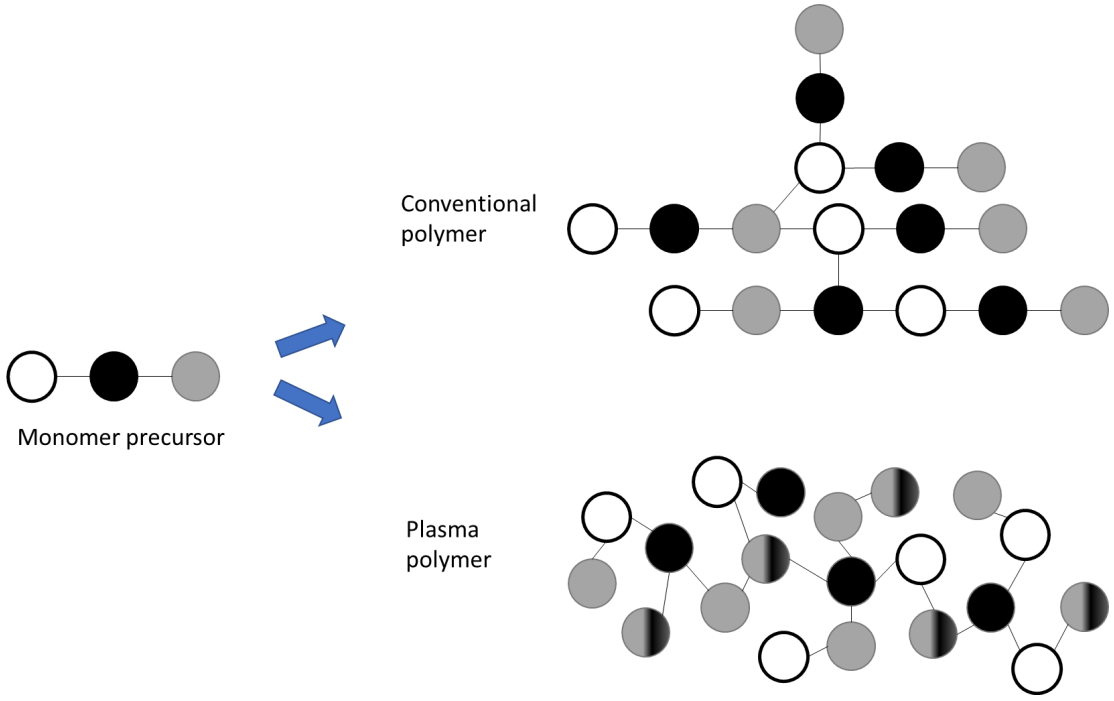

Figure 3. Diagram of potential polymers. A contrast between traditional polymers and plasma polymers.

Plasma polymers are commonly found as deposits on solid surfaces of electrical discharge devices that work with organic vapours activated by plasma. Several mechanisms have been proposed to explain the interaction between plasma and monomer molecules during plasma polymerization. Lam [30] introduced an early, straightforward, yet successful concept known as free-radical plasma polymerization.

In this concept, during the initial activation phase, electrons inelastically interact with the precursor molecule, exciting it and potentially causing molecular dissociation, which produces free radicals. During the subsequent propagation phase, radicals attach to undamaged precursor molecules by opening unsaturated carbon bonds, leading to an increase in molar mass. Lastly, in the termination phase, the growth of polymer chains is halted when radicals recombine. Refer to Figure 4 for a visual representation of Lam's concept.

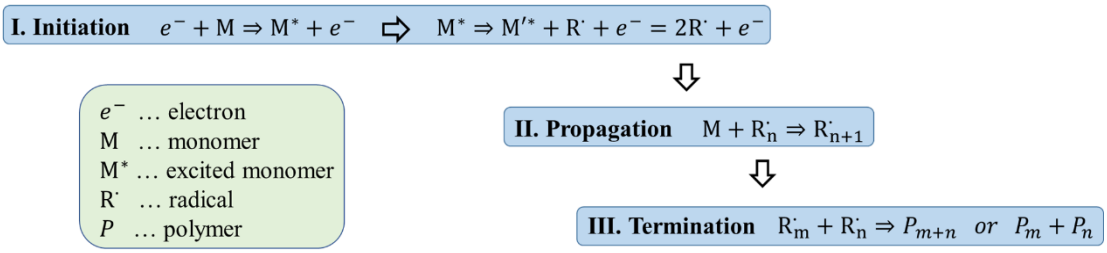

Figure 4. Free-radical mechanism of plasma polymerization concept by Lam, adapted from [30]

Later on, Yasuda [31] introduced a more complex concept of the plasma polymerisation process (see Figure 5). Yasuda suggested that the polymerisation mechanism is a rapid step-growth process that happens in two major cycles. Cycle 1 is equivalent to the standard free-radical mechanism introduced by Lam [30], where monofunctional activated species ($M\bullet$) are involved in the repeated activation of the reaction products. Cycle 2 involves difunctional species ($\bullet M \bullet$) species, the monomer species containing together cationic and radical propagating centres or dual radicals. Difunctional species allow the simultaneous growth of polymeric chains in multiple directions.

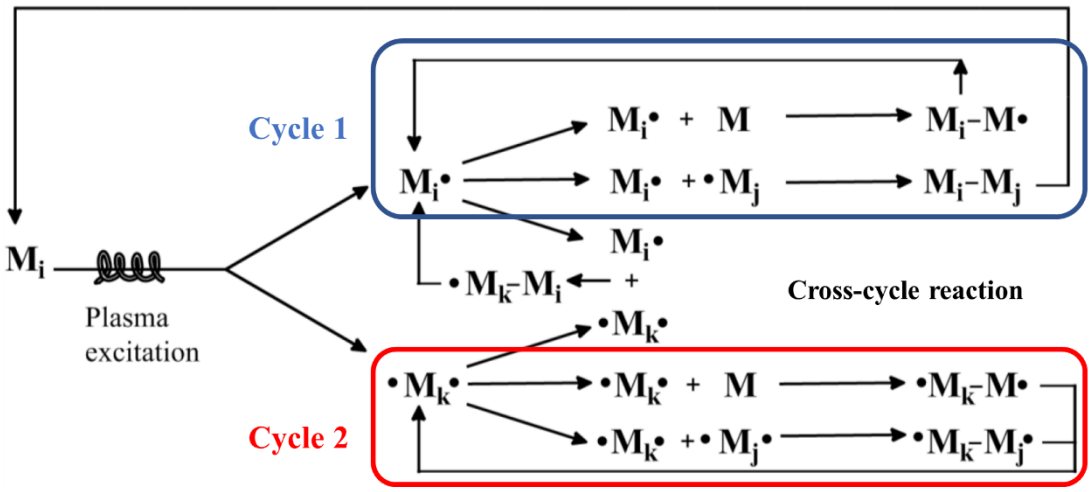

Figure 5. The rapid step-growth polymerization mechanism by Yasuda. Adapted from [31]

To complete the description of plasma polymerization processes, it is necessary to mention the importance of the electron and ion bombardment of the surface. As discussed in Section 1.2, energetic particles from plasma may interact with the surface in various ways. Similarly, D'Agostino suggested [32] that the energetic particles' bombardment is responsible for precursor desorption from the substrate, sputtering (erosion), and polymer cross-linking. Controlling particles' energy, for instance, by means of pressure in the experimental chamber or by discharge power, allows us, to some degree, to control a plasma polymer film growth. Moreover, when the pressure within the reactor rises, it triggers the generation of micro- and nanoscale particles in the plasma region. This occurrence later became widely recognized as dusty plasma or complex plasma.

The technical realisation for plasma polymer reactors could be done in many arrangements. Widely used reactors were summarised by Kylian et al. in [33] (see Figure 6). The one used in this work (therefore, will be described in detail below) is an asymmetric parallel-plate electrode reactor, also known as a magnetron sputtering reactor, as shown in Figure 6b.

Magnetron sputtering

As was described in Section 1.2., if energetic electrons and ions with sufficient energy impinge the target surface, it may lead to the extraction of a small fragment of this target. These fragments are then transported by working gas flow to the substrate (or sample), creating a thin layer by deposition. The source of the plasma is an RF-powered planar magnetron – an electrode with a crossed-perpendicular homogeneous electric and non-homogenous magnetic field of a closed path (see Figure 7), which creates a trap for electrons due to the effect of an ExB drift (described in [1]). These trapped electrons can then collide with gas atoms or molecules, ionizing them and creating a plasma. The ions generated in this process can be trapped in the ExB trap as well. The number of ions trapped depends on several factors, including the strength of the magnetic field, the gas pressure, and the geometry of the trap.

For ions to bombard the target with sufficient energy to initiate sputtering, the magnetron must be cathode against the plasma. Fortunately, if a magnetron (electrode) is capacitively coupled with an alternating current power supply with a frequency of more than 1 MHz (when ions become almost immobile due to high

inertia, and electrons oscillate with relatively small distances) a pulsating negative potential will develop on the electrode [34]. A self-biased negative potential appears due to electrons' high mobility. During the first half-cycle of the radio frequency (RF) voltage, an enormous amount of electrons flow to the electrode. Only after a delay, during the second half-cycle, a relatively low number of ions reach the electrode (due low mobility of heavier particles). The total electron and positive ion charges flow towards the electrode over each cycle must balance to zero, and the electrode surface becomes negatively self-biased against plasma. Usually, values for a self-biased negative potential range between 100-1000 V [5], [9].

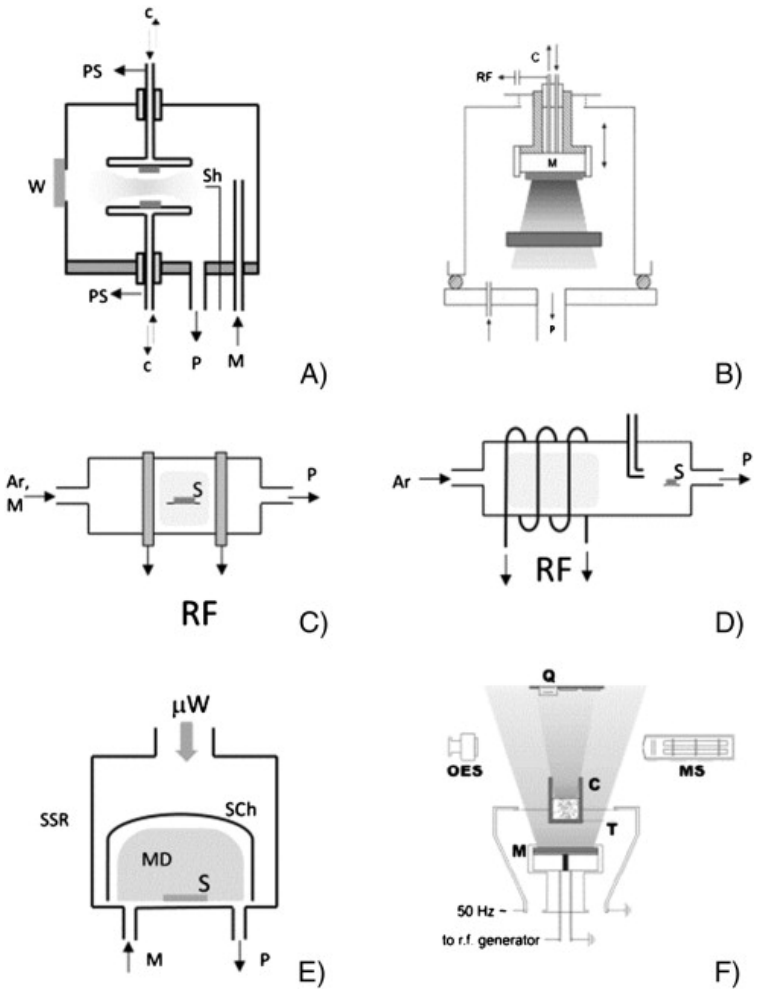

Figure 6. Deposition systems: A) symmetric parallel-plate electrode reactor (PS = to power supply, C = cooling, W = window, P = to pumps, M = monomer, Sh = shutter, S = substrate); B) asymmetric parallel-plate electrode reactor (M = planar magnetron as the excitation electrode); C) tubular glass or silica deposition system with external ring electrodes (M = monomer, S = substrates, P = pumps); D) tubular glass or silica deposition system with external excitation coil (monomer inlet and substrate S are downstream); E) simple microwave reactor (μW = microwave energy, MD = microwave discharge, SSR = stainless-steel resonator, SCh = silica chamber, S = substrate, M = monomer, P = to pumps); and F) polymer thermal decomposition system with auxiliary discharge (Q = quartz crystal microbalance, OES and MS = optical emission and mass spectrometers, respectively, M = magnetron with graphite target, T = thermocouple, C = evaporator). After ref. [33]

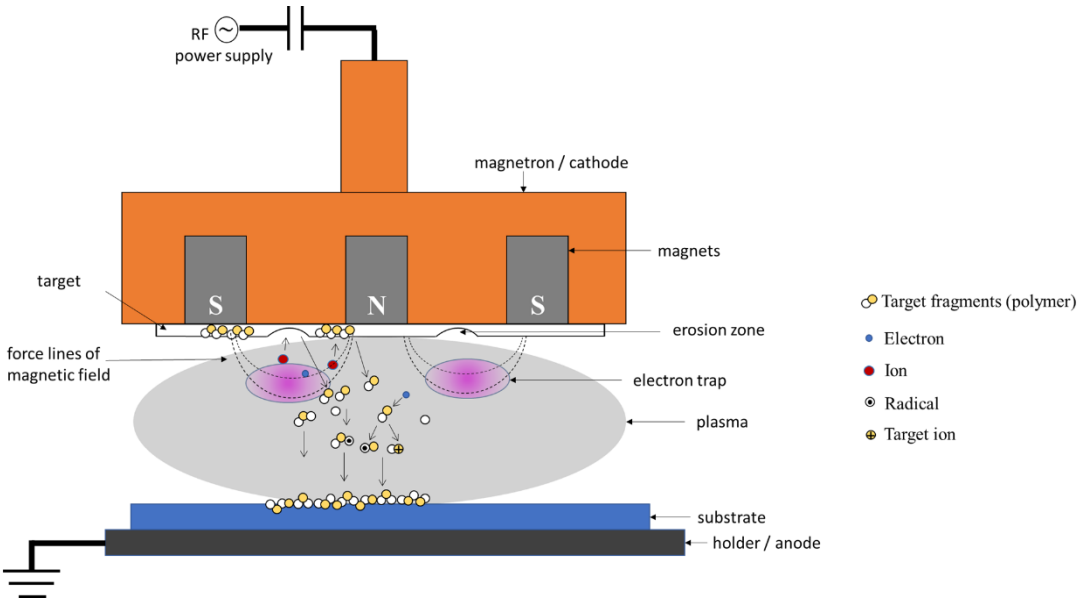

Figure 7. Simplified illustration of a magnetron sputtering technique. A polymer target is used as an example.

Magnetron sputtering technique found its implementation in the sputtering of polymer materials creating a unique type of plasma polymer. For cases with polymer targets, the ion from plasma dissociates a small polymer fragment from the target after bombardment, and those fragments (mostly neutral) in the plasma region may become ionized, dissociate and convert to radicals or ions. Fragments, later on, polymerise on the substrate creating a thin layer that is highly cross-linked. Method of magnetron sputtering was successfully applied for sputtering of polytetrafluoroethylene (PTFE) [35]–[43], polypropylene [41], [44]–[47], polyethylene [42], [45], [48], polyamide [49]–[55], nylon [56], polyaniline [57], amorphous hydrocarbon [58]. This work will also present results from the magnetron sputtering of polylactic acid (PLA) polymer. Magnetron sputtering technique may as well be utilised for the nanostructuring of the plasma polymers by creating nanoparticles (NPs) using a so-call gas aggregation cluster source, which will be described below.

Gas aggregation cluster source

In Figure 6, many plasma polymerisation deposition technics are shown where the substrate is placed in the same chamber where the polymerisation occurs. There, the growth of the film on the substrate depends on the supply of radicals and monomer from the gas phase or the diffusion over the solid/vacuum interface. If the nanostructured surface is desired, then these methods have a rather complected controlling mechanism over the process of creation of nanostructured plasma

polymers. The interest in nanostructured plasma polymers was and still is vast because of the promising advantages that they bring. For instance, the deposition of two different polymers with different properties, like hydrophilic and hydrophobic polymers, allows forming of coatings with tuneable wettability [42]. Other applications of nanostructured plasma polymers (in combination with copper and silver NPs) that could benefit industries such as electrotechnical, biomedical, optical, etc., were discussed in [59]–[67]. The search for more ecological and more efficient methods of NPs synthesis continues nowadays. However, the aggregation of NPs in cold buffer gas showed its potential and is considered one of the most promising methods of NPs generation.

A gas aggregation cluster source (GAS) is a broad technic pioneered in the first half of the 20th century [68]. This and later research were based on the principle of material evaporation with direct precursor heating [69]–[71]. Introducing the magnetron into the GAS chamber, which was done by Haberland and his colleagues [72], brought significant advantages over the evaporation cell GAS techniques, such as more stable deposition rates and relatively more straightforward process control and longer operation time. Mechanism description of the NPs formation in the magnetron-based GAS can be found in [72]–[74]. In Haberland's GAS, a dc planar magnetron (or two opposing planar magnetrons) was applied to sputter a metal target to an inert gas flow of low temperature (see Figure 8). Under specific super-saturation conditions, atomic metal vapours condense with the formation of clusters or NPs, which can be further transferred by the carrier gas flow and deposited on substrates.

Furthermore, NPs acquire electrical charge in the low-temperature plasma generated by the magnetron. Therefore mass-to-charge separation, trajectory deflection, and acceleration/deceleration can be employed to control the NP transport and landing on substrates. Consequently, sputter-based GAS has become very popular [75]–[84]. However, despite the popularity of GAS in the scientific community, there are still uncertainties and a lack of understanding of the physical processes that take place in GAS.

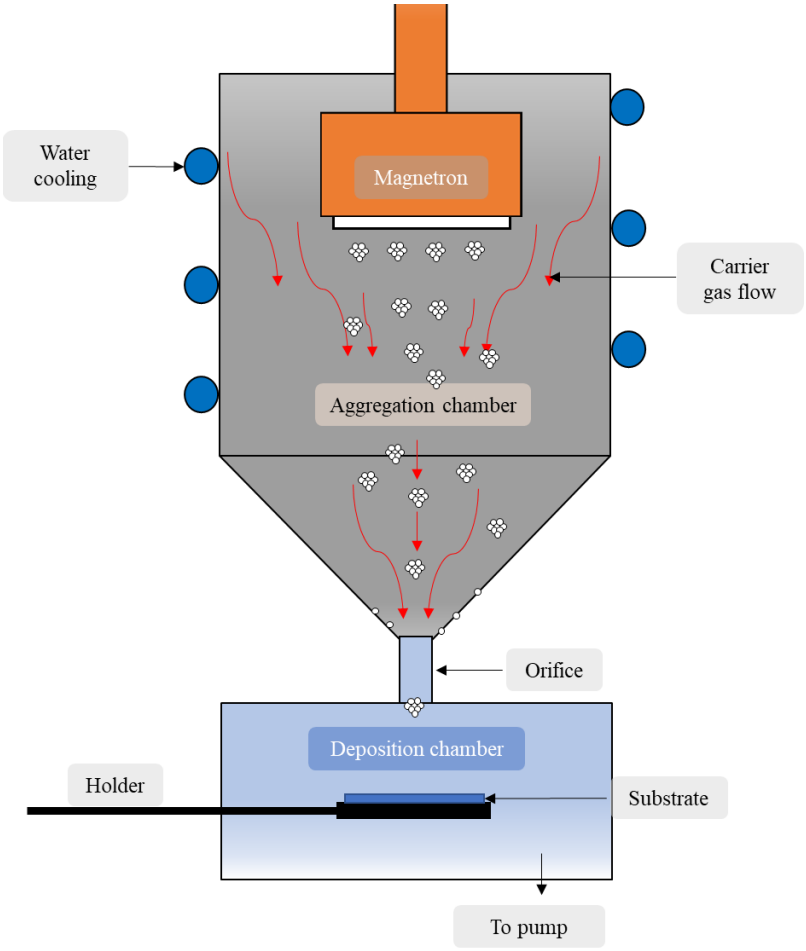

Figure 8. Schematic drawing of the magnetron-based gas aggregation cluster source

In the research that our group conducted in DESY synchrotron, Hamburg, Germany (in cooperation with the Chair for Multicomponent Materials Faculty of Engineering, Kiel University, Germany) [74], it was revealed by in situ small angle X-ray scattering (SAXS) analysis, that there exists a capture zone, or also known as an NPs trap, in the proximity of the magnetron and target. In order to understand the cause of the NPs capture, it was necessary to eliminate electromagnetic forces from the carrier gas drag force. The author of this work had the capability to provide research on the influence of the carrier gas flow on NPs' behaviour. This topic proved to draw interest from various research groups and industries. Therefore, the author's attention was shifted towards understanding the influence of the carrier gas flow on NPs formation, motion and losses in magnetron-based GAS systems. It is also important to note that the NPs trapping is specifical for magneton-based GAS systems. However, the NPs' transportation by means of carrier gas flow drag is crucial for many other aggregation

cluster sources. Therefore, understanding and control over the gas flow may significantly contribute to cluster sources being widely implemented in industry.

One of the methods to understand the carrier gas flow inside the GAS is to conduct a numerical simulation of the fluid dynamics. The scientific field that is dedicated to questions of numerical simulation of fluid's behaviour in closed and opened domains (including thermodynamics) is called Computational Fluid Dynamics (CFD). The brief description and theory behind CFD are described in Section 2..

2. Computational Fluid Dynamics for GAS

CFD is a numerical method that computes fundamental governing equations of fluid dynamics, usually in the form of integral or partial derivation equations. CFD is the set of codes that discretise algebraic forms, which are then solved to obtain flow field values at discrete points in space and time.

Three fundamental laws upon which all fluid dynamics are based are: mass and energy are conserved, and Newton's second law. From these three fundamental laws, we may derive governing equations of fluid flow[85]:

- Continuity equation, which is derived from the law that mass is conserved.
- The momentum equation, derived from Newton's second law, incorporates among body forces also, pressure forces (from surroundings) and normal and shear stress forces caused by friction (effect of viscosity).
- Energy equation, which is derived from the law that energy is conserved. The physical principle of energy conservation is essentially the first law of thermodynamics. The rate of energy change inside the fluid domain is equal to the net heat flux into the fluid domain plus the rate of work done on fluid due to body and body surface forces.

The entire system of flow equations for the solution of viscous flow in fluid dynamic terminology is called Navier-Stokes (N-S) equations. Although historically accurate N-S equations were referred to exclusively for momentum equations [85]. But we will stick with the adopted approach and refer to N-S equations as a complete system of equations derived from the flow governing equations. The derivation process of N-S equations is well known and may be found in many fluid dynamics or CFD-dedicated study literature, for example, in John D. Anderson's book [85]. However, for reference, in

, one may find the final forms of the governing equations for the unsteady, three-dimensional, compressible viscous flow. These equations are coupled non-linear partial differential equations, where for instance, the friction and velocity are interdependent. Till today there is no general closed-form analytical solution exists. Therefore, a numerical approach must be made to solve them, which brings us to CFD.

In this section, we will mostly focus on the CFD relevance (Section 2.1.) and usage for GAS since conditions, hence, challenges that we meet in the GAS from a fluid dynamic perspective, are specific and unique. What applies to the aerospace or automotive fields is not relevant low-pressure flows that we have.

Fundamental governing equations of the flow are true for any kind of flow. So, what is the difference between the flow over the transport aircraft in the wind tunnel, the same aircraft in the free flight and the flow of Argon in the gas aggregation cluster source? Obviously, despite the fact that the same set of N-S equations is used, there is a huge number of differences. However, these differences could be categorized into two major categories. First be *Boundary Conditions*, which describe the geometry of the object over which the fluid flows, the geometry of the fluid domain bounded by the *walls*, do these walls heat up or cool down the fluid, from where the fluid flow enters (*inlet*) at what speed and where the fluid goes afterwards (*outlet*), and so on. All this is defined by the boundary conditions (BC), which is described for use in the GAS and similar systems in Section 2.2.. The second group of differences is the so-called Fluid Model, which represents the fluid and flow parameters. For instance, is our fluid the gas of Argon or Oxygen, what is the regime of the flow, etc.? The fluid model for the GAS and similar systems is described in Section 2.3..

2.1. Knudsen Number

The mathematical description of fluid dynamics relies on the assumption that the flow in the fluid domain is continuous. The length and time scales are much larger in the continuous flow regime than in the atomic/molecular scale. In rarefied gases, the mean free path (eq. (10)) may become large so that it is comparable to the macroscopic (continuous flow) length scale.

$$\lambda = \frac{k_B \cdot T_f}{\sqrt{2} \cdot \pi \cdot d_{fm}^2 \cdot p_f} \quad (10)$$

Here, λ is a mean free path, k_B is the Boltzmann constant, T_f is s fluid (gas) temperature, d_{fm} is a fluid molecule or atom diameter (van der Waals diameter is assumed), and p_f is the pressure of the fluid domain.

When the system size is so small that it is comparable to the mean free path, one may falsely denote this as a microscopic (molecular flow) length scale. Therefore, a particularly useful parameter is the Knudsen number (eq. (11)).

$$Kn = \frac{\lambda}{L} \quad (11)$$

Here, L is the characteristic length of the fluid domain. The Knudsen number defines the ratio between the mean free path and the representative system size. For Kn $\ll$ 1, the continuity N–S and CFD are valid. For Kn $\geq$ 10, molecular flow applies (kinetic theory). The region 0.01 < Kn < 1 corresponds to a slip flow. For 1 < Kn < 10, transitional flow applies, and Monte-Carlo simulation is required, specifically in near-wall regions.

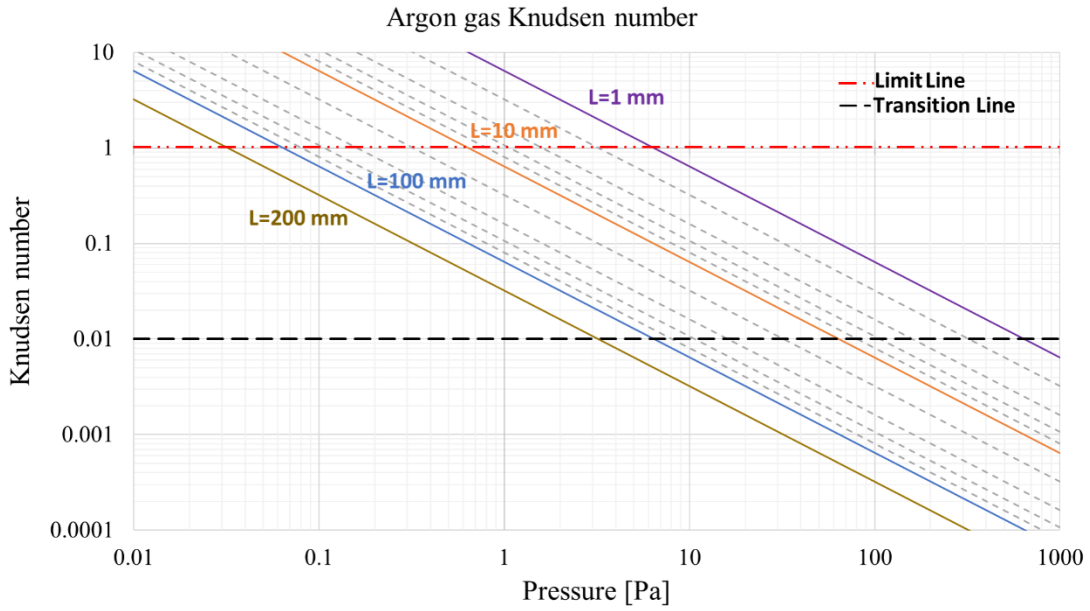

Figure 9. Knudsen number of Argon gas. Dependence on pressure and system size at 293 K.

Figure 9 shows the calculation of the Argon Knudsen number for pressures between 0.001 and 1000 Pa and various characteristic lengths. For instance, the typical use of the GAS presumes differential pressure between the aggregation chamber (tens to hundreds of Pa) and the deposition chamber (below 1Pa). For a typical GAS of 100 mm in diameter, the working conditions meet the requirements of a continuous flow;

therefore, the CFD usage is valid. A few exceptions exist in the GAS where the gas may flow in the transition regime. For example, the flow in the small exit orifice may be characterised by larger Kn; in this case, so-called “slip correction” is necessary. The concept of slip correction is shown in Section 2.2.4..

2.2. Boundary Conditions

Boundary conditions, along with the fluid model, dictate the particular solution to be obtained from the governing equations. From a mathematical perspective, BC is the real driver for the solution of the governing equations. Therefore, the correct definition of BC from a physical perspective and the perspective of numerical implementation of these physical conditions are of the uttermost importance. Of course, we will not discuss in detail the numerical part of the problem here since it is a substantial scientific field by itself. Still, if one is interested, the following literature is good for familiarising the problem [85]–[87]. Instead, we will focus on the physical meaning of BC that is specifically suited for the application of CFD in the GAS and similar systems.

2.2.1. Inlet Boundary Conditions

CFD software allows us to define a few types of boundary conditions. For the inlet, the most frequently used Dirichlet boundary conditions (only normal component is a non-zero value) for flow simulations in the GAS are mass flow inlet and velocity inlet.

In experiments, one usually controls the inlet mass flow in cm^3_{STP}/min (cubic cm per minute at standard atmospheric pressure, “sccm”) units. The standard atmospheric pressure is 1 bar = 10^5 Pa and the temperature of 0 °C or 273.15 K. In that case, the mass flow inlet BC is more suitable. However, it is essential to note that the mass flow inlet BC is typically defined as a kilogram per second (kg/s). Therefore, it is necessary to convert sccm to kg/s. To do this, we may use the following steps starting from the equation of state:

$$pV = nRT \rightarrow p \cdot \frac{V}{n} = RT \rightarrow p \cdot \frac{M}{Z\rho} = RT \tag{12}$$

If we assume fluid compressibility to be $Z = 1$, then density is:

$$\rho = \frac{pM}{RT} \tag{13}$$

Mass flow rate

$$\dot{m} = \rho \cdot \dot{q} \tag{14}$$

Substituting equation (13) into equation (14), we get the relation between mass flow rate and volumetric flow rate:

$$\dot{m} = \frac{pM}{RT} \cdot \dot{q} \tag{15}$$

Correcting for units gives us then sccm to kg/s conversion formula for standard environment conditions (atmospheric presser at 0 °C):

$$\dot{m}\left[\frac{kg}{s}\right] = \left(6 \cdot 10^{7}\right) \cdot \frac{p_0[Pa] \cdot M\left[\frac{kg}{kmol}\right]}{R\left[\frac{J}{K \cdot kmol}\right] \cdot T_0[K]} \cdot \dot{q}[sccm] \tag{16}$$

Where p is a pressure of a system ($p_0 = 101325\,Pa$, standard atmosphere pressure), V is a volume, n is the number of moles of a substance, R is the universal gas constant, T is a temperature of a system ($T_0 = 273.15\,K$, standard atmosphere temperature), M is the molar mass of a gas, $\dot{m}$ is a mass flow rate, $\dot{q}$ is a volumetric flow rate.

In the case of the velocity inlet boundary condition, for instance, used by Rudd et al. [88], an extra step is needed to convert the gas mass flow rate into the gas velocity by dividing the mass flow rate value by gas density and inlet cross-sectional area. In an ideal simulation model, there should be no difference between the mass flow rate BC and velocity BC. However, it was noticed for unoptimized simulation models that in the case of velocity BC the mass flow rate at the outlet does not correspond to the inlet mass flow rate (converted from sccm), which is against mass conservation law. If the gas inlet's velocity BC is considered, extra care should be taken while building the simulation model (material data, initial conditions, simulation relaxation factors, mesh quality, etc.).

2.2.2. Outlet Boundary Conditions

The pressure outlet boundary condition is the best fit for the CFD simulations of the GAS. This boundary pressure can be considered as the static pressure of the

environment into which the fluid exits. Specifically, in the case of the GAS simulations, it can be regarded as the pressure in the deposition chamber, which is usually less than 1 Pa. Similar to inlet boundary conditions, the pressure outlet boundary condition is of the Dirichlet type, i.e. it takes into account only the normal component of the flow. It is important to note that the outlet surface should be placed a few centimetres away from the orifice end.

Despite a low pressure and relatively high Knudsen number in the deposition chamber, it is still recommended to leave some space in the simulation model after the orifice. It helps the pressure gradient fully develop and facilitates capturing backflow or vortices around the orifice. Most importantly, it helps the simulation to be more stable and converges faster.

2.2.3. Wall Boundary Conditions

A 'wall' in the CFD terminology is not only a chamber wall but, generally, anything that is not an inlet or outlet. Under normal conditions, proper physical BC for a viscous flow on the walls assumes zero relative velocity between the wall (solid's surface) and the fluid interfaced with that wall. This is a so-called *no-slip* condition, i.e. if walls are stationary with the fluid moving past them, then all the fluid velocity components are zero (at the surface) [85]. Slip – is the phenomenon in the fluid dynamics that appears in the near-wall regions, where the fluid slides along the wall without any shear forces. In the case of continuous flow, where the Knudsen number is well below Kn << 0.01, the usually no-slip boundary condition is applied. No-slip boundary condition means that fluid sticks to the wall and moves with the same velocity as the wall. Thus, for a stationary wall, the fluid has zero velocity at the wall. In situations where the Knudsen number is $0.01 < Kn < 1$, e.g., rarefied gas flows, partial slip correction is required. Slip correction is described in Section 2.2.4..

Analogically applies to the thermal condition. If we have a wall temperature T_w, then the temperature of the fluid layer in contact with the wall is also T_w. However, if the temperature of the wall is unknown and the heat is transferred from the fluid to the wall or vice-versa, then the Fourier law of heat conduction is applied as BC on the wall.

$$\dot{q}_w = -\left(k\frac{\partial T}{\partial n}\right)_w \quad (17)$$

Where $\dot{q}_w$ is the heat flux to the wall or from the wall, and n denotes the direction normal to the wall. This type of BC, if the flow is concerned, is a boundary condition on the temperature gradient at the wall. Finally, if there is no heat transfer from the wall to the fluid or vice-versa, then we apply adiabatic BC.

For instance, in the simulations we did for the GAS, we used room temperature (20 °C) for the chamber walls and 40 °C for the magnetron target surface, as measured by a thermal camera.

2.2.4. Slip Correction

Full-slip (or just slip) BC mostly applies to non-Newtonian fluids using the Viscous Flow model. In practice, it means that the flow speed on the wall is the same as the bulk flow speed distanced from the wall. The full-slip BC is not applicable in our case [89]. As mentioned in the previous section, partial slip correction is required when the Knudsen number is $0.01 < Kn < 1$, e.g., rarefied gas flows.

As shown in Figure 9, in the typical GAS that operates, for example, under 100 Pa, the slip correction should be applied in regions smaller than 10 mm. It could be an orifice, inlet channels or the gap between the magnetron and the chamber. In our work, the Maxwell slip correction for laminar flow was used (eq. (18)). For the more prominent length scale, default settings (no-slip condition) for the wall slip can be safely applied. The velocity correction then takes the following form [89], [90]:

$$\vec{v}_{tangent} = \frac{2-\sigma_{v,spec}}{\sigma_{v,spec}} \cdot \lambda \cdot \left.\frac{\partial \vec{v}}{\partial n}\right|_{wall} \quad (18)$$

Here, $\sigma_{v,spec}$ is the specified tangential momentum accommodation factor, from 0 to 1, an empirical parameter denoting the gas-surface momentum exchange; n is the normal distance from the wall, and $\vec{v}$ is the velocity vector.

Rudd et al. [88] discussed the influence of slip on the NP agglomeration on walls and on the flow. A partial slip was found to increase the wall interaction surface area twice compared to the full-slip condition.

2.3. Fluid Model

Generally, CFD offers a large number of tools that help solve a significant number of problems. The CFD software utilised is not of great importance since the basis of all CFD codes is the same. However, some software better handle instabilities, converges in fewer iterations due to modified algorithms, has a friendly graphical interface, a wider choice of computational modules, better meshing algorithms, etc. It usually depends on one's experience with particular software and how precisely the simulation should be performed. Four software packages were primarily used to simulate gas flow and particle motions in the GAS and similar systems.

- OpenFoam – open-source software. Ref. [88], [91]–[93]
- Ansys Fluent – commercial software by Ansys Inc. [94], [95]
- STAR CCM+ – commercial software by Siemens. Ref. [74], [96]–[99]
- COMSOL Multiphysics – commercial software by COMSOL Group. Ref. [100], [101]

It is also vital to notice that if the software offers to choose between single-precision (32-bit floating-point numbers) and double-precision (64-bit floating-point numbers) versions, double-precision should be selected. Although the double-precision version of the simulation generally requires 15-20% more CPU time and 20% more memory requirements [89], the precision and stability of the simulation are substantially better than the single-precision version. In our case, the double-precision version is used.

At the beginning of Section 2., we described the governing equations for the fluid flow, which are true for all fluids. However, some technicalities that are essential for flow simulations under conditions similar to the GAS are still left to describe.

2.3.1. Flow regime

Before one begins with the simulation, choosing the appropriate physical model for the simulation is crucial. Otherwise, the software, in a good scenario, will crash, and in a worse case, the code will compute some results, and an inexperienced user may falsely interpret results, leading to false conclusions. Simply saying, if there is a mistake in the simulation model, especially if the flow regime was chosen inappropriately, then the results will definitely be a mistake.

The dimensionless Reynolds number (Re) (eq. (19)) defines whether the flow is laminar or turbulent.

$$\Re = \frac{\rho_f \cdot v \cdot L}{\mu} \tag{19}$$

Here, ρ_f is the density of the fluid, v is the fluid velocity, L is the characteristic system dimension, and μ is the dynamic viscosity of the fluid. The geometry of GAS resembles the 'pipe' geometry with relatively smooth walls; therefore, a standard pipe's critical Reynolds number of $Re_{crit} \approx 2000$ can be assumed [102]. It is generally known that the linear flow speed does not exceed a few $m\,s^{-1}$ in the GAS [74], [88], [91]–[98]. A conservative estimate with the system diameter of 200 mm, the fluid velocity of 10 $m\,s^{-1}$, and Ar pressure of 150 Pa gives Re ≈ 221, which is well below the $Re_{crit.}$ Therefore, it is safe to assume that the flow in the aggregation region is laminar. In the orifice region, the flow velocity may increase to hundreds of m/s as a result of the expansion. However, the orifice diameter usually does not exceed 5 mm, compensating for the velocity increase and satisfying the condition $Re < Re_{crit}$. However, in this case, slip correction may be necessary.

In addition to weather the flow is laminar or turbulent, it is also essential to determine whether the flow is compressible. In reality, any fluid is compressible (fluid density is non-constant). But under certain conditions, such as low speed (lower than the speed of sound) air flow over the wing, it is reasonable to assume that the density of the air is constant. Which significantly simplifies aerodynamic calculations and subsequently saves the time and cost of the development processes. Contrarily, under given conditions that GAS operates (hundreds of pascals pressure, room temperature, inlet mass flow rate, etc.), it is safe to state that the gas in the cluster source obeys the ideal gas law. Therefore, the flow in the simulation is set to be *compressible flow*, which is solved assuming the ideal gas law.

2.3.2. Initial condition

The working gas pressure in the GAS is set as the initial *pressure* condition in the simulation model. However, we should also account for the additional value of the dynamic pressure from the inlet and pressure losses (pressure drop) from the orifice. Therefore, if we have high inlet flow and a long narrow orifice, the simulation code

may end up, for non-optimised simulation models, getting absolute total pressure of approximately 300 Pa if we set the initial pressure as 50 Pa. It is important to optimise the model prior to extracting results by increasing the quality of the discretisation mesh, boundary layer prismatic mesh, simplifying geometry, optimising default model constants, etc.

The initial *temperature* condition sets the global environment temperature in the simulation model. The initial *velocity* condition sets the gas flow velocity, if needed, despite the impact of the inlet flow.

Setting initial *turbulence* conditions, if the turbulence model is used, is a complex task, and not always default values are of good use. Fortunately, as was explained above, a laminar flow regime in most cases is required, and turning on the turbulence model will only increase the computational cost of the simulation without any additional value.

2.4. Other technical considerations for CFD

Coupling algorithm

In the simulations that are presented in this work, the *Segregated Flow solver* was used. Segregated flow solver solves each of the momentum equations in turn, one for each dimension. The linkage between the momentum and continuity equations is achieved with a predictor-corrector approach. The complete formulation can be described using a collocated variable arrangement and a Rhie-and-Chow-type pressure-velocity coupling combined with a Semi-Implicit Method for Pressure Linked Equations (SIMPLE) algorithm [89], [85]–[87].

Mesh

The type of discretisation mesh (e.g., tetrahedral, polyhedral, trimmed hexagonal, etc.) does influence the simulation results; however, it is more important to meet the quality requirement of mesh cells itself as well as follow certain simulation building guidelines. Mesh quality criteria for various situations can be found in the user guides of the software of interest [89], [103]. Some ‘rule of thumb’ model building guidelines that are useful for the model build-up for the GAS and similar systems are described below.

- For laminar flows, it is recommended to have a number of cells in boundary layers of five for adequate velocity changes near the wall for better slip calculations.
- Refine the mesh in regions of interest and where there is a steeper change of values (high gradient). For example, around the inlet regions, closer to the orifice, near the magnetron, etc. On the other hand, it is recommended to re-coarse the mesh in the areas where no abrupt changes (excessive gradient) of calculated values are expected.
- If the distance between two walls is narrow (for example, orifice), despite the number of boundary layer cells, there should be at least three (five is better) cells in between to register the fluid velocity changes in narrow regions adequately.

2.5. Solid Particle Model

Even though solid particles are not part of the fluid dynamic theory, the CFD is a computational code which allows being modified by extension with other physical codes. Therefore, CFD can be used not only for fluid flow simulations but also for thermal simulations, fluid-solid interactions, and many more. For us, the particular interest is the fluid-solid particle interactions.

The simulation type with more than one simulation phase present (fluid – gas & solid – NP) is called a 'multi-phase' simulation. There are two major approaches for multi-phase simulations: the Eulerian-Lagrangian (for simplicity, called just Lagrangian) and the Eulerian-Eulerian (for simplicity, just Eulerian). The Lagrangian approach solves idealised isolated particles that are transported with the flow and may account for turbulence, momentum transfer, heat transfer, and mass transfer. The Eulerian approach solves two or more coexisting fluids: one phase is present in another phase at a relatively high ratio (e.g. bubbles in water) or two completely separated phases where each phase is contiguous through the domain, and there is a well-defined boundary between the phases (for example, a half-filled bottle of water).

In the GAS, the number of NPs is usually much less than the number of carrier gas atoms. Therefore, each NP may be treated as a discrete solid unit that moves in the

GAS under various forces. Hence, the Lagrangian approach is used to describe the evolution of individual particles as they traverse the domain.

The particle equation of motion (eq. (20) is based on the conservation equation of momentum written in the Lagrangian framework. The change in momentum is balanced by the surface and body forces that act on the particle.

$$m_p \cdot \frac{d\vec{v}_p}{dt} = \vec{F}_S + \vec{F}_B \tag{20}$$

Here, m_p is the particle mass, $\vec{v}_p$ is the instantaneous particles velocity, $\vec{F}_S$ is the resultant of the forces that act on the surface of the particles, and $\vec{F}_B$ is the resultant of the body forces.

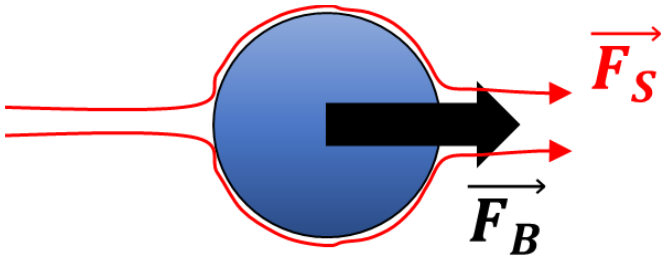

Figure 10. Forces on the solid spherical particle

These forces may be decomposed into:

$$\vec{F}_S = \vec{F}_D + \vec{F}_p \tag{21}$$

and

$$\vec{F}_B = \vec{F}_g + \vec{F}_C + \vec{F}_{Br} \tag{22}$$

Here, $\vec{F}_D$ is the drag force, $\vec{F}_p$ is the pressure gradient force, $\vec{F}_g$ is the gravity force, $\vec{F}_C$ is the Coulomb force, $\vec{F}_{Br}$ is the Brownian force.

Drag Force

For submicrometric spherical particles moving through the fluid, Stoke's drag must be corrected by a Cunningham factor for higher Knudsen numbers [104], [105]. In that case, the drag is [106]:

$$\vec{D} = \frac{18 \cdot \mu}{d_p^2 \cdot \rho_p \cdot C_C} \cdot \vec{v}_{ps} \left[\frac{m}{s^2}\right] \tag{23}$$

Here, μ is the dynamic viscosity of the fluid, d_p is the particle diameter, ρ_p is the particle mass density, $\vec{v_{ps}}=(\vec{v_f}-\vec{v_p})$ is the particle slip velocity (relative fluid velocity over the particle surface), and C_C is the Cunningham correction factor for Stoke's drag [107]:

$$C_C=1+\frac{2\lambda}{d_p}\cdot\left(1.257+0.4\,e^{-\left(\frac{1.1\,d_p}{2\lambda}\right)}\right) \quad \textbf{(24)}$$

Here, λ is the molecular mean free path from eq. (10).

It is important to note that the drag calculated in eq. (23) is the acceleration. To obtain the force, it needs to be multiplied by a particle mass, $\vec{F_D}=\vec{D}\cdot m_p$.

Pressure Gradient Force

The pressure gradient is defined as [89]:

$$\vec{F_p}=-V_p\cdot\nabla\ p_{f_{Static}} \quad \textbf{(25)}$$

Here, $\nabla\ p_{f_{Static}}$ is the gradient of the static pressure of the fluid domain, and V_p is the volume of the particle.

The pressure gradient force is insignificant in the main portion of the aggregation chamber since the pressure does not vary there. However, the pressure gradient may affect particle motion in narrow regions, e.g., orifice, the distance between the magnetron and chamber walls, etc. Regardless, the pressure gradient force component remains insignificant compared to the drag force or Brownian force.

Gravity Force

The gravity force may be neglected because it is substantially smaller than other forces since NPs are of very low weight. However, for reference, see eq. (26).

$$\vec{F_g}=m_p\cdot\vec{g} \quad \textbf{(26)}$$

Here, $\vec{g}$ is a gravitational acceleration vector.

Coulomb Forces

Particles can enter the domain bearing electrical charges or, under some circumstances, acquire electric charges after entering, resulting in an additional force acting on the particles.

$$\overrightarrow{F_C} = q \cdot \vec{E} \tag{27}$$

Here, q is a particle charge and $\vec{E}$ is an electric field.

Brownian Force

Brownian motion is the random motion of particles suspended in a fluid resulting from collisions with quick molecules/atoms of the fluid. The random factor is represented in this force by a zero-mean unit-variance-independent Gaussian random number ς_i, which generates a sequence of normal random variables which are uniform over the range between 0 and 1. The method of producing these random numbers was described by Marsaglia and Bray [108]. The Brownian force itself is given by [105]:

$$\overrightarrow{Br} = \varsigma_i \cdot \sqrt{\frac{\pi \cdot S_0}{\Delta t}} \left[\frac{m}{s^2} \right] \tag{28}$$

Here, Δt is a particle time step and S_0 is a spectral intensity coefficient [105]:

$$S_0 = \frac{216 \cdot \upsilon \cdot k_B \cdot T_f}{\pi^2 \cdot \rho_f \cdot d_p^5 \left(\frac{\rho_p}{\rho_f} \right)^2 \cdot C_C} \tag{29}$$

Here, υ is the kinematic viscosity, ρ_p is the particle mass density, ρ_f is the fluid mass density, k_B is the Boltzmann constant, T_f is the fluid temperature, and C_C is the Cunningham correction factor shown in eq. (24). The force calculated in eq. (29) is a specific force per unit mass, $\overrightarrow{F_{Br}} = \overrightarrow{Br} \cdot m_p$.

Near Orifice Region

In the near orifice region, where a pressure drop of several orders of magnitude occurs over the length of several millimetres accompanied by a strong acceleration of the carrier gas flow due to expansion, the Stokes drag approach with the Cunningham correction factor is no longer valid. Since the mass versus cross-section ratio of the nanoparticle increases with its diameter and the carrier gas density decreases during expansion, the heavier particles do not undergo enough collisions with light gas atoms to equalize their velocity and direction with the gas [109]. This may cause differences in the motion trajectory between lighter and heavier NPs. This effect is called

aerodynamic lensing or aerodynamic focusing [110]–[112]. Although sometimes the effect on the flight trajectory of particles of various sizes is negligible, their velocity differences remain. Particle acceleration in the near orifice region should be then corrected for that phenomenon.

The acceleration of a spherical particle in the gas flow, derived by Smirnov et al. in [110], is described by the equation:

$$\frac{\vec{v_p}}{dt}=\vec{a_p}=f\cdot\vec{v_{ps}} \tag{30}$$

Where $\vec{v_p}$ is a solid particle velocity, $\vec{v_{ps}}$ is a particle slip velocity, and f is a proportional collisional frequency coefficient shown in the eq. (31).

$$f=\frac{m_{fa}}{m_p}\cdot N\cdot \upsilon_{therm}\cdot\sigma \tag{31}$$

Here m_{fa} is the mass of the carrier gas atom or molecule, m_p is a solid particle mass, N is a numeric density of the gas, $\upsilon_{therm}=\sqrt{\frac{k_B T}{m}}$ is an average thermal velocity of the carrier gas, and σ is a particle cross-section.

Equation (30) does not account for the dependence of the collision frequency of the particle with the gas on the solid particle acceleration and hence, on its drift velocity. To solve this issue, Kousal et al. derived in [109] the thermal velocity correction factor ξ, by adding the velocity vector of the gas molecule to the vector of difference between drift velocities of gas and the particle.

$$\xi=1+\frac{1}{\pi}\cdot\left(1.6\cdot\omega-\omega^2+0.285\cdot\omega^3\right) \tag{32}$$

Where ω is the ratio between particle slip velocity to average thermal velocity:

$$\omega=\frac{\left|\vec{v_{ps}}\right|}{v_{therm}} \tag{33}$$

This correction assumes fully elastic collisions between light gas molecules and heavy spherical solid particles. The collision leads, on average, to a momentum transfer of 4/3 of the momentum of the gas molecule to the particle. The acceleration of the particle then:

$$\vec{a_p} = \frac{4}{3} \cdot \xi \cdot f \cdot \vec{v_{ps}} \quad (34)$$

To obtain the force acting on the particle, we should multiply acceleration with the particle mass: $\vec{F_p} = m_p \cdot \vec{a_p}$.

Neglecting correction factors for the collision frequency and the momentum transfer results in the NPs' final velocity being about 25% lower [109].

2.5.1. Multi-Phase Model Implementation

Steady State

There are several ways in which one can perform a simulation of both the fluid domain and solid particles' motion. For example, Zhang et al. [91] conducted a completely steady-state simulation, where fluid flow equations were solved simultaneously with the motion of the particles. So-called 'two-way coupling' simulations were performed, where fluid flow (Eulerian field) and particle motion (Lagrangian fields) are interdependent. Therefore, the influence of NP transport on fluid flow was taken into consideration. It was achieved in the steady-state regime by alternating continuous and discrete phase equations until a converged coupled solution was reached.

Semi-transient

The number of NPs is evidently smaller than the number of gas atoms, as well as the size of NPs is small enough to consider that the fluid flow is unaffected by the presence of the NPs. Therefore, only fluid flow affects the motion of NPs but not vice versa. This approach is called 'one-way coupling' [89], [103]. In this case, the fluid flow is first solved in a steady-state regime until the convergence. Afterwards, the flow is 'frozen', as is, it stores the fluid field data and does not solve the N-S equations even if the solver continues to run. NPs are then added to the system and solved transiently (unsteady), taking the necessary fluid flow information from the previous steady-state simulation. In that case, NPs do not affect fluid flow in any way.

Transient

Fully transient two-way coupled simulation (it can also be one-way coupled) solves governing fluid dynamic equations and particle motion equations with a time-dependent approach. In this case, we may see 'real-time' changes in the position of

the particles as well as changes in the fluid flow if this occurs. However, it is important to state that these kinds of simulations are demanding in terms of CPU cost, time (hence, electricity consumption), and disk storage.

If a global and quick solution is desired, then it is recommended to use the steady-state approach. For a more detailed understanding of the particle motion and relative efficiency of the GAS in terms of gas flow in the chamber, it is recommended to use semi-transient simulation, as it is a moderate approach. The fully transient simulation is recommended for detailed simulation of the particle motion, where the local observation is essential or some fine-tuning of the GAS is required. If the fully transient simulation is wanted, testing out the model by at least steady-state simulation is strongly recommended to debug the model and if no fundamental errors are presented.

3. Experimental and Simulation set-up

3.1. Magnetron sputtering

The experimental set-up used to sputter PLA fragments was based on the bell-jar vacuum reactor, pumped by the diffusion pump backed by the oil rotary pump. There was used 3-inch cylindrical, planar magnetron with a water cooling system. PLA bulk target was fastened to the cathode (magnetron electrode). In this experiment, commercial PLA from NatureWorks® was used, with the designation "2500HP". Technical datasheet and safety datasheet information of PLA 2500HP can be found on the manufacturer's website (www.natureworksllc.com). The thickness of the target was 2±0.07 mm.

Substrates were placed approximately 30 mm below the magnetron, and argon was used as a carrier gas (2 sccm, which made ≈ 6 Pa system pressure). A schematic diagram of the set-up is shown in Figure 11. RF (13.56 MHz) discharge power applied was in the range of 20-130W.

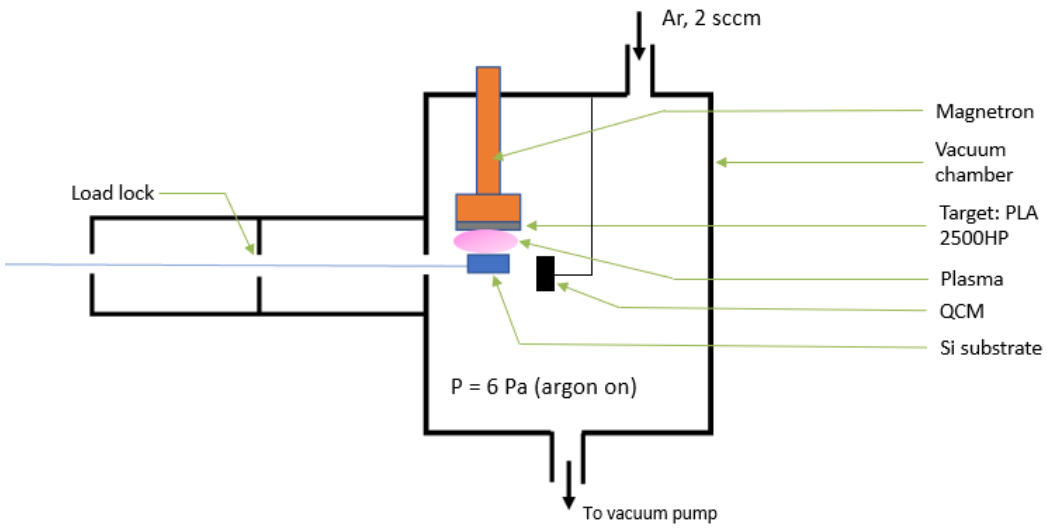

Figure 11. Schematic diagram of the bell-jar vacuum reactor (Magnetron sputtering system) used in the experiment

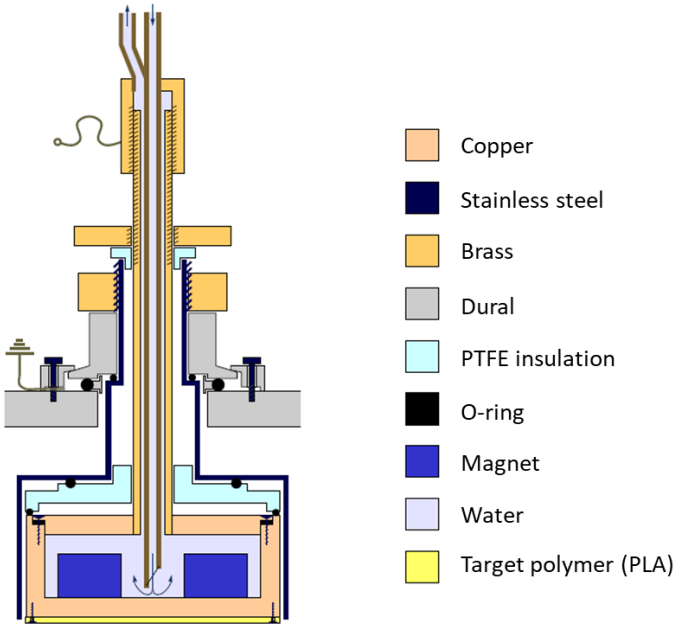

Figure 12. Magnetron structure. Adapted from [113].

3.2.Magnetron-Based Gas Aggregation Cluster Source

There were several magnetron-based GAS systems used in this study that share similar principles but under different conditions with different characterisation methods involved. To keep a reasonable size of the work, only selected experimental techniques will be described in detail, and if discrepancies appear, they will be mentioned in the related sections.

3.2.1. Planar magnetron GAS

The experiments were performed in an ultra-high vacuum system pumped by scroll and turbomolecular pumps to the base pressure of 4×10^{-5} Pa. The main deposition chamber was equipped with a magnetron-based GAS mounted in the vertical configuration (Figure 13). The GAS consisted of a water-cooled aggregation chamber 100 mm in diameter and 220 mm long with two quartz windows, a glass window for the discharge observation and a port for the sample holder. Sputtering of a 3 mm thick Ag target (99.99% purity) was realized by a movable 3-inch magnetron. The magnetron was powered by a direct current generator MDX-500 (Advanced Energy, Fort Collins, CO). The discharge current of 500 mA was kept constant during all experiments. The aggregation chamber was ended by a conical lid with an orifice of 2mm diameter. The aggregation length (the distance between the magnetron target and the orifice) could be varied by the movement of the magnetron. Quartz crystal microbalance (QCM, Inficon, Bad Ragaz, Switzerland) was used to control the

deposition rate in the main chamber. Figure 13 also schematically shows the UV–Vis light passage for the in situ spectroscopy characterization of Ag NPs in the aggregation zone. Details of the UV-Vis technique are described in Section 3.4.3..

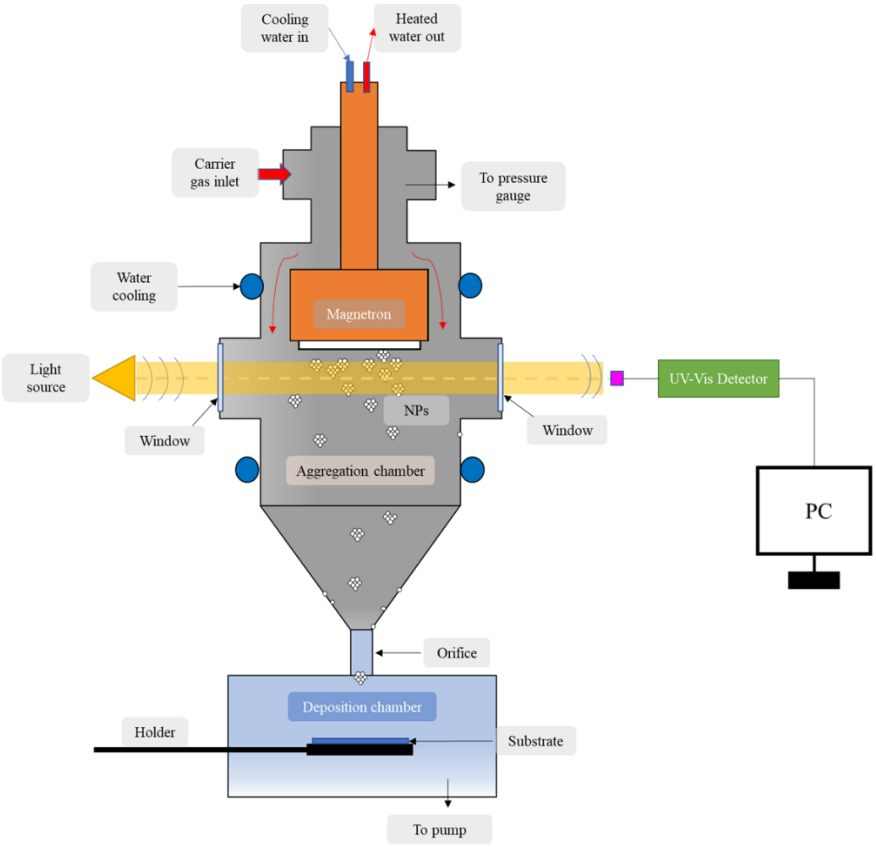

Figure 13. Planar magnetron GAS scheme with equipped UV-Vis

3.2.2. GAS with an auxiliary chamber for in-flight coating of NPs

NPs produced in GAS can be additionally modified by installing an auxiliary chamber between the GAS and the deposition chamber, as it was implemented, for example, in [114]. In this case, the auxiliary chamber is equipped with two parallel-plate planar magnetrons for the in-flight coating of primary NPs with a secondary material, as shown in Figure 14. The main difficulty of such an experimental decision lies in the necessity to properly choose the dimensions of the orifices that separate the GAS, the auxiliary chamber, and the deposition chamber because the pressures in the three chambers are not independent. To date, research has mostly been limited to test-and-trial experiments to find the proper combinations of orifices that would maintain sufficiently high pressure for the NP production in the GAS and the optimal pressure

in the auxiliary zone to cover the NPs with the secondary material. In this work, the author decided to use CFD to characterise the carrier gas flow performance for such a geometry, providing guidelines for the orifice choice for future experimentalists.

In experiments (from which input data were taken for subsequent CFD analysis): The system was pumped by scroll and turbomolecular pump to the base pressure of 10^{-4} Pa. The support pumping essentially is connected to the deposition chamber, therefore, it is pumped be the same system as has just been described. The gas flow was controlled by a flow controller (MKS MFC). A capacitive gauge (MKS baratron) determined the pressure inside the aggregation chamber. The magnetron was powered by a direct current (DC) power supply (Advanced Energy Pinnacle 3000) operated in a constant current mode.

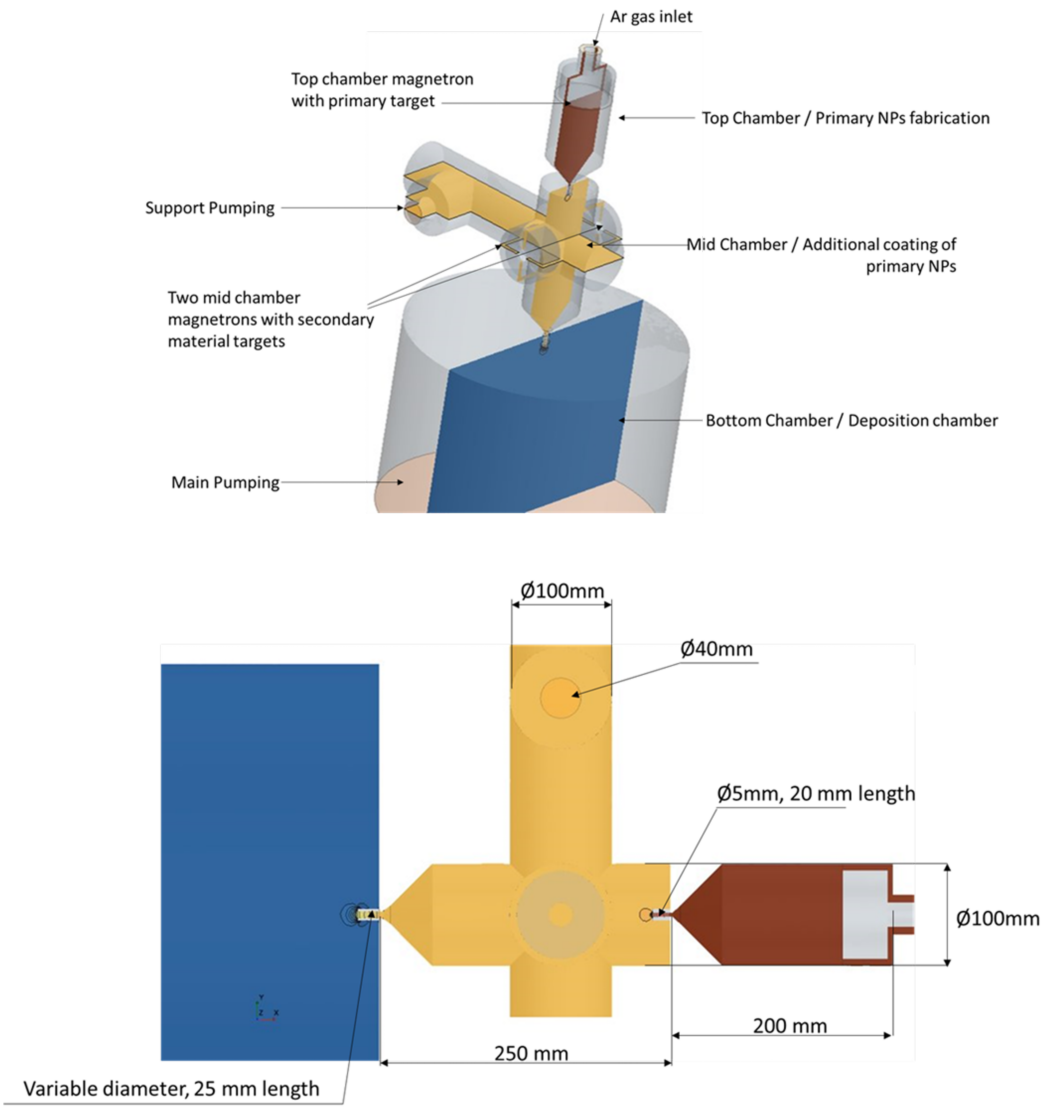

Figure 14. Gas system for composite NPs fabrication.

3.2.3. Post-cylindrical magnetron GAS

A cylindrical post magnetron of a custom design 50 mm in external diameter and 180 mm long was suspended top-down in a vacuum chamber 150 mm in inner diameter (Figure 15). The cylindrical body was made of Cu with a wall thickness of 5 mm. A single magnetic circuit was placed inside the magnetron and attached to a spindle that enabled their rotation driven by an external motor. The circuit was made rectangular with a longer side of 110 mm and a shorter side of 30 mm, generating two elliptical magnetic tunnels shifted by 180°. The magnetron interior was cooled by circulating water. Ar was used as a working gas. The gas inlet was from the back of the magnetron at the top of the aggregation chamber. The bottom of the chamber was equipped with a circular orifice of exchangeable diameter. The assembly of the cylindrical magnetron and the aggregation chamber was installed on another vacuum chamber where NP deposition on substrates was performed. The system was pumped by scroll and turbomolecular pump to the 10^{-4} Pa base pressure. The gas flow was controlled by a flow controller (MKS MFC). The pressure inside the aggregation chamber was determined by a capacitive gauge (MKS baratron). The magnetron was powered by a direct current (DC) power supply (Advanced Energy Pinnacle 3000) operated in a constant current mode.

The NP throughput was monitored in situ by quartz crystal microbalance (QCM) placed in the deposition chamber at the axis of the GAS 10 cm below the orifice. The NPs were investigated by scanning electron microscopy (SEM; JEOL JSM-7200F). The NPs size was evaluated using the software Solarius Particles (~300 NPs were taken into account).

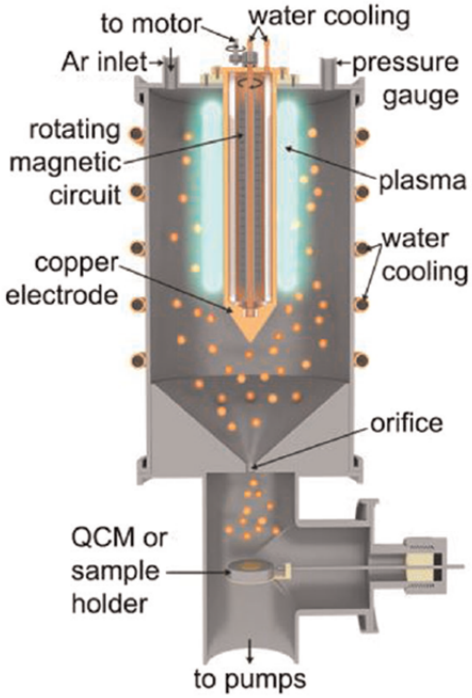

Figure 15. Post-Cylindrical magnetron GAS scheme. From [96].

3.3. Simulations set-up

This section describes the simulation models' setup parameters and properties, which results are presented in the Results and Discussion section. All simulations were done in the software Siemens STAR CCM+. Reported models are already optimised (for mesh quality, computational time & cost, and mesh sensitivity) and provided converged results. Convergence was checked by residual values and critical simulation parameters.

Residuals are a measure of the accuracy of the numerical solution. They represent the difference between the computed values of the flow variables (e.g., velocity, pressure, temperature, etc.) at each iteration and the corresponding values from the previous iteration. The lower the residual, the more converged the solution. All residuals were ensured to fall below 10^{-6} for all residual values.

A critical parameter is a parameter of interest that we acquire from the CFD simulation or can prove that simulation results are adequate. Such parameters are pressure in the aggregation chamber, surface average velocity (from section cut), outlet mass flow, average temperature, etc. The critical parameter is considered converged if the value does not change or if the change is neglectable with each

simulation iteration. It should be valid for both steady-state and transient simulations. In the case of transient simulation, there were at least 10 iteration steps between each time step.

3.3.1. Planar magnetron GAS with rear inlet

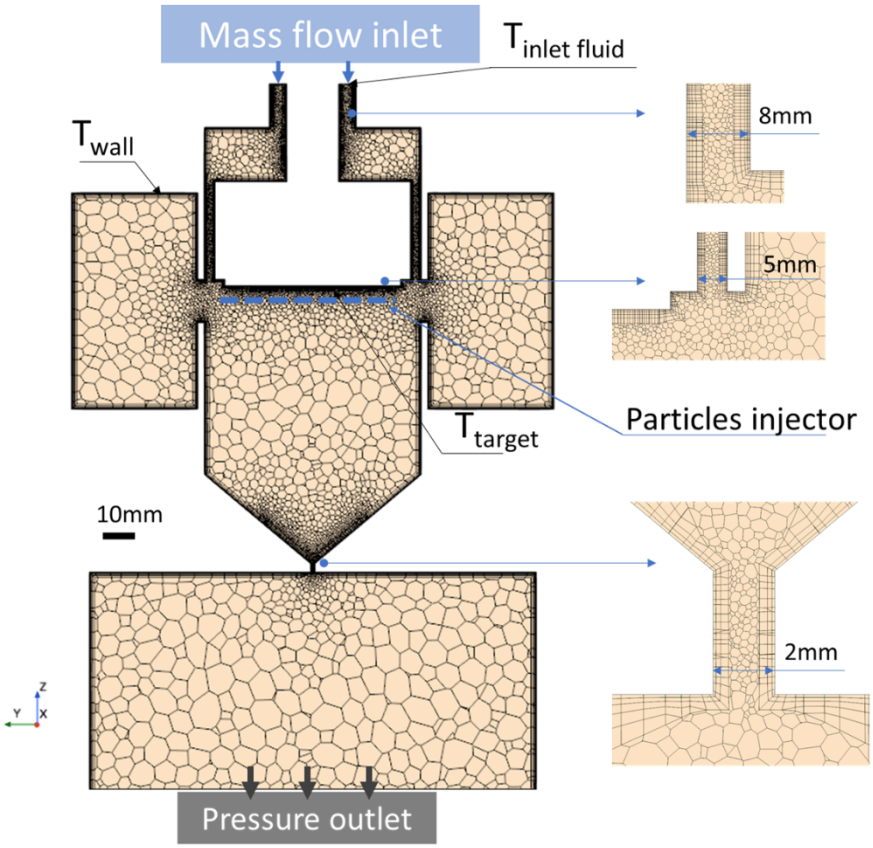

Figure 16. Mesh for the planar magnetron GAS with rear inlet configuration, section cut.

Figure 16 shows the simulated fluid domain for the GAS with a planar magnetron. This system is configured to have a carrier gas inlet located behind the magnetron, the so-called “rear inlet” configuration, which is discussed in Section 4.2.5..

Table 1 shows model configuration data. It includes mesh data, a physics model for fluid and solid particles, initial conditions and inputs required for the proper simulation.

Solid particles were injected into the fluid domain approximately in the trapping region, i.e. 5 mm far from the target. It is also assumed that particles do not grow after they enter the domain. To estimate the impact of the carrier gas flow on NPs’ motion, all forces, except the drag, Brownian, and pressure gradient forces, were neglected.

Table 1. Simulation model configuration for the planar magnetron GAS with rear inlet configuration.

Mesh Data	
Domain	3D
Base mesh type	Polyhedral
Boundary layer mesh	Prismatic
Base mesh size	5 mm
Minimum mesh size	0.1 mm
# of boundary layers	5
# of cells	1 795 834
Flow simulation model	
Turbulence model	Laminar
Simulation type	Steady state
Solver	Segregated
Thermal	Activated
Algorithm	SIMPLE
Under-relaxation factors	Velocity: 0.7 Pressure: 0.3 Energy: 0.9

Inputs & Initial conditions	
Fluid material	Ar
Initial total pressure	133 Pa
Initial temperature	293 K
Outlet pressure (total)	0.1 Pa
Inlet mass flow*	$5.347 \cdot 10^{-7}$ kg/s (18 sccm)
Inlet fluid temperature	293 K
Wall temperatures	293 K
Target temperature	305 K
Solid particle simulation model	
Modelling approach	Semi-Transient (implicit)
Fluid flow	From steady-state flow simulation
Particle model	Lagrange
Particle material	Ag (Silver) Density = 10490 kg/m^3
Forces	Drag Pressure gradient Brownian **

* Inlet mass flow rate was also: 24 sccm. Details mentioned in the results and discussion section
** For comparison, a simulation without Brownian motion was done too

3.3.2. Planar magnetron GAS with magnetron inlet

Figure 17 shows the simulated fluid domain for the GAS with a planar magnetron. This system is configured to have a carrier gas inlet inside the magnetron, the so-called “magnetron inlet” configuration, which is discussed in Section 4.2.5..

Table 2 shows model configuration data. It includes mesh data, a physics model for fluid, initial conditions and inputs. There was a total of 12 simulations done for 3 different geometries (varying aggregation length) and 4 different inlet flow rates.

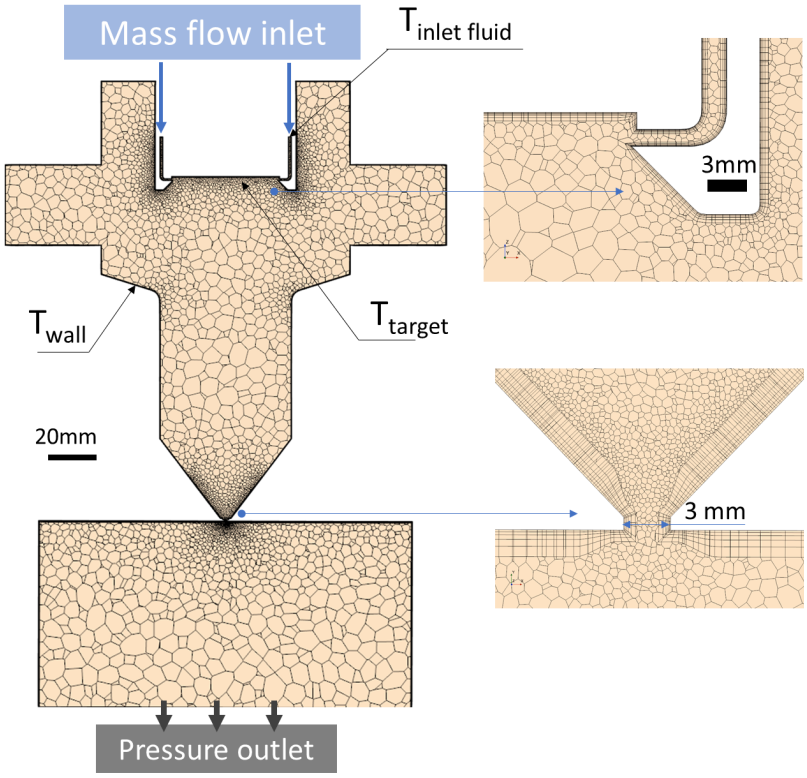

Figure 17. Mesh for the planar magnetron GAS with magnetron inlet configuration, section cut

Table 2. Simulation model configuration for the planar magnetron GAS with magnetron inlet configuration.

Mesh Data	
Domain	3D
Base mesh type	Polyhedral
Boundary layer mesh	Prismatic
Base mesh size	5 mm
Minimum mesh size	0.2 mm
# of boundary layers	5
# of cells for a model with aggregation length = 155 mm = 165 mm = 185 mm	 1 723 357 1 750 435 1 785 236
Flow simulation model	
Turbulence model	Laminar
Simulation type	Steady state
Solver	Segregated
Thermal	Activated
Algorithm	SIMPLE
Under-relaxation factors	Velocity: 0.7 Pressure: 0.3 Energy: 0.9

Inputs & Initial conditions				
Fluid material	Ar			
Initial total pressure	49 Pa	113 Pa	177 Pa	220 Pa
Initial temperature	293 K			
Outlet pressure (total)	0.1 Pa			
Inlet mass flow* (kg/s)	$7.13 \cdot 10^{-7}$	$1.78 \cdot 10^{-6}$	$2.85 \cdot 10^{-6}$	$3.56 \cdot 10^{-6}$
Inlet fluid temperature	293 K			
Wall temperatures	293 K			
Target temperature	305 K			

* 24, 60, 96, 120 sccm, respectively.

3.3.3. GAS for in-flight coating of NPs

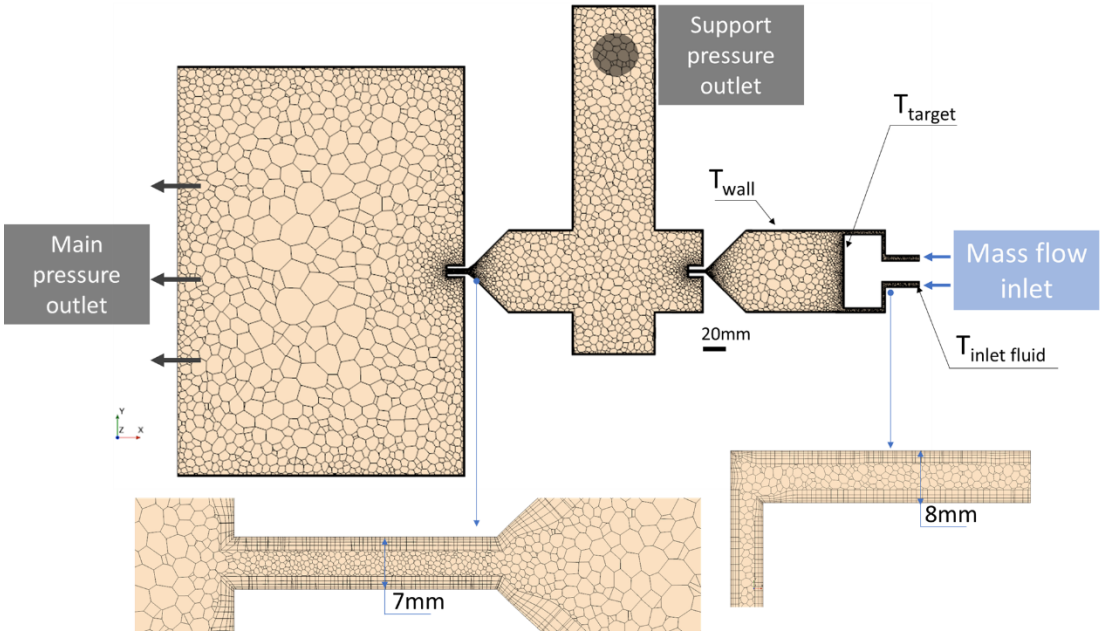

Figure 18. Mesh for the in-flight coating GAS, section cut.

Figure 18 shows the simulated fluid domain for the GAS for in-flight NPs modification. Simulations were done for two configurations. First, where the support pressure outlet is open, and in that case, the boundary BC is set to be a pressure outlet. Second, where the support pump outlet is closed, and in that case, the boundary is assumed to be a wall.

Table 3 shows model configuration data. It includes mesh data, fluid and solid particles physics model, initial conditions and inputs.

Table 3. Simulation model configuration for in-flight coating GAS.

Mesh Data	
Domain	3D
Base mesh type	Polyhedral
Boundary layer mesh	Prismatic
Base mesh size	5 mm
Minimum mesh size	0.2 mm
# of boundary layers	5
# of cells for a model with a mid-chamber orifice Ø7 mm Ø11 mm Ø15 mm	 862 314 823 761 825 024
Flow simulation model	
Turbulence model	Laminar
Simulation type	Steady state
Solver	Segregated
Thermal	Activated
Algorithm	SIMPLE
Under-relaxation factors	Velocity: 0.7 Pressure: 0.3 Energy: 0.9

Inputs & Initial conditions	
Fluid material	Ar
Initial total pressure	40 Pa
Initial temperature	293 K
Outlet pressure - Main (total)	0.16 Pa
Outlet pressure – Support (total)*	3.5 Pa 0.0 Pa
Inlet mass flow	$2.08 \cdot 10^{-7}$ kg/s (7 sccm)
Inlet fluid temperature	293 K
Wall temperatures	293 K
Target temperature	305 K
Solid particle simulation model	
Modelling approach	Semi-Transient (implicit)
Fluid flow	From steady-state flow simulation
Particle model	Lagrange
Particle material	ZrN Density = 7090 kg/m^3
Forces	Aerodynamic lensing drag Pressure gradient Gravity Brownian**

* Simulation was done for a model with and without support pumping
** Brownian was included only for Ø10 nm particles.

3.3.4. Post-cylindrical magnetron GAS

Figure 19 shows the simulated fluid domain for the post-cylindrical GAS at its baseline configuration. Using CFD, optimisation cycles were performed to determine the proper inlet configuration to achieve an adequate flow pattern. Mesh setting remained the same for all geometrical variations.

Table 4 shows model configuration data. It includes mesh data, fluid and solid particles physics model, initial conditions and inputs.

Solid particles were injected into the fluid domain radially, approximately 5 mm from the target. It is also assumed that particles do not grow after they enter the domain. To estimate the impact of the carrier gas flow on NPs' motion, all forces, except the drag, Brownian, and pressure gradient forces, were neglected.

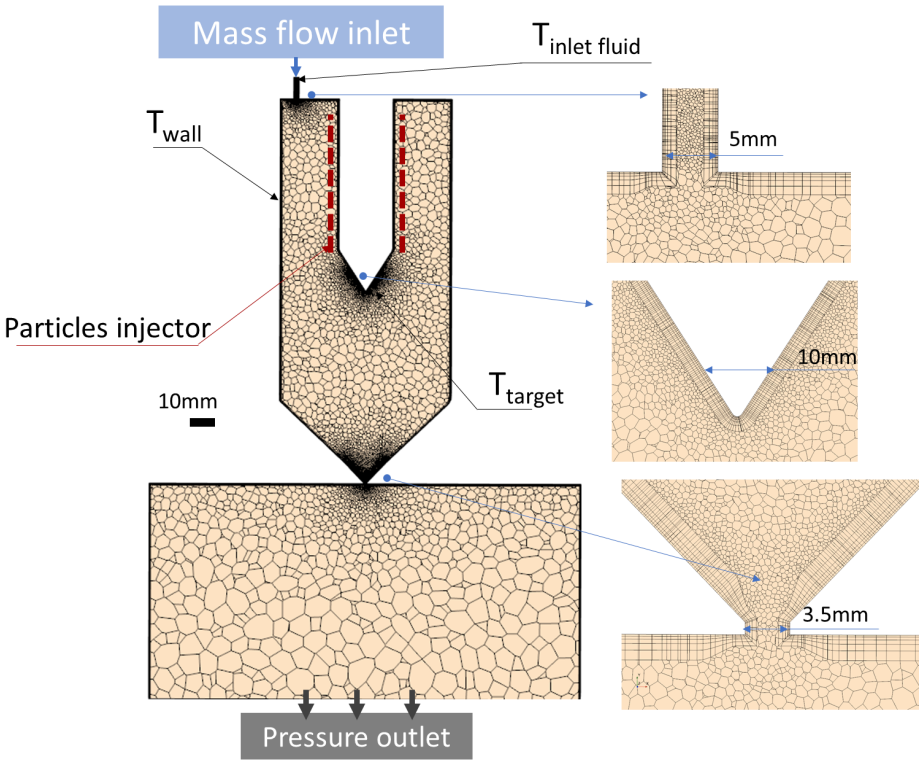

Figure 19. Mesh for the post-cylindrical magnetron GAS, section cut. Single asymmetrical inlet configuration.

Table 4. Simulation model configuration for the post-cylindrical GAS.

Mesh Data	
Domain	3D
Base mesh type	Polyhedral
Boundary layer mesh	Prismatic
Base mesh size	6 mm
Minimum mesh size	0.1 mm
# of boundary layers	5
# of cells	3 000 000*
Flow simulation model	
Turbulence model	Laminar
Simulation type	Steady state
Solver	Segregated
Thermal	Activated
Algorithm	SIMPLE
Under-relaxation factors	Velocity: 0.7 Pressure: 0.3 Energy: 0.9

* Actual number of cells varied as the geometry optimisation via CFD was performed

Inputs & Initial conditions			
Fluid material		Ar	
Initial total pressure	117 Pa	160 Pa	160 Pa
Initial temperature		293 K	
Outlet pressure (total)		0.2 Pa	
Inlet mass flow* (kg/s)	$5.94 \cdot 10^{-7}$	$1.19 \cdot 10^{-6}$	$2.97 \cdot 10^{-6}$
Inlet fluid temperature		293 K	
Wall temperatures		293 K	
Target temperature		305 K	

Solid particle simulation model	
Modelling approach	Semi-Transient (implicit)
Fluid flow	From steady-state flow simulation
Particle model	Lagrange
Particle material	Ag (Silver) Density = 10490 kg/m^3
Forces	Drag Pressure gradient Brownian

3.4. Diagnostic Methods

3.4.1. Quartz Crystal Microbalance

The quartz crystal microbalance (QCM) is an in-situ method used to measure the mass deposited on a quartz crystal surface through the piezoelectric effect. QCM comprises a circular quartz crystal with two metal electrodes linked to a power supply, frequency counter, and computer interface (as depicted in Figure 20).

The connection between the mechanical deformation of the quartz crystal, its thickness, and the applied current is well understood. This enables the control of an acoustic resonance through electrical methods. When an alternating current (AC) voltage is applied to the quartz, acoustic shear waves travel along the crystal at the resonance frequency (f):

$$f = \frac{v_p}{2t} = \frac{N}{t} \tag{35}$$

Where, v_p is a transverse elastic wave velocity, t is a thickness of a crystal, N is the frequency constant of a crystal.

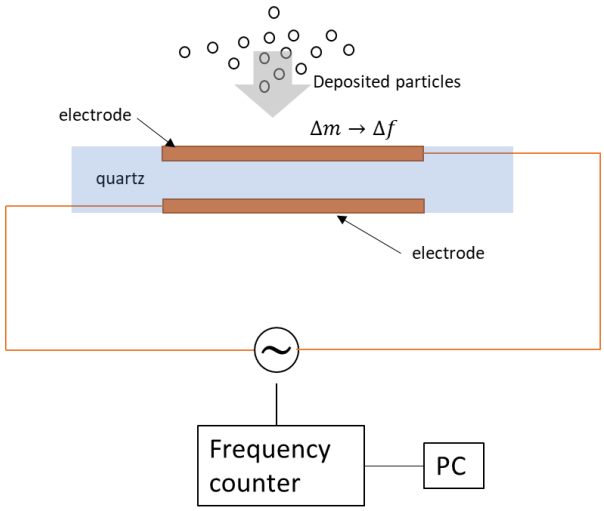

Figure 20. QCM diagram

When the mass is deposited on the crystal, creating a thin layer, the thickness increases, and the resonance frequency decreases. The mass change per unit area is proportional to the frequency change of the quartz resonator ($\Delta m \propto \Delta f$). The Sauerbrey equation establishes the relationship between mass change and frequency change:

$$\Delta f = \frac{-f_0 \cdot \Delta m}{A \cdot \sqrt{\rho_q \mu_q}} \quad (36)$$

Where, f_0 is a resonant frequency, A is a crystal area, ρ_q is a quartz material density, μ_q is a shear modulus of quartz. Additional information on QCM theory can be found in reference [115].

A QCM (Maxtek) featuring a 5 MHz quartz crystal with a diameter of 12.7 mm was employed to monitor the deposition rate.

3.4.2. X-Ray Photoelectron Spectroscopy

X-ray photoelectron spectroscopy (XPS), commonly referred to as Electron Spectroscopy for Chemical Analysis (ESCA), is a spectroscopic method that relies on the photoelectric effect to determine the elemental composition of surface materials. XPS employs monochromatic radiation in the x-ray spectrum to produce photoelectrons, which are subsequently analyzed based on their energy within the analyzer.

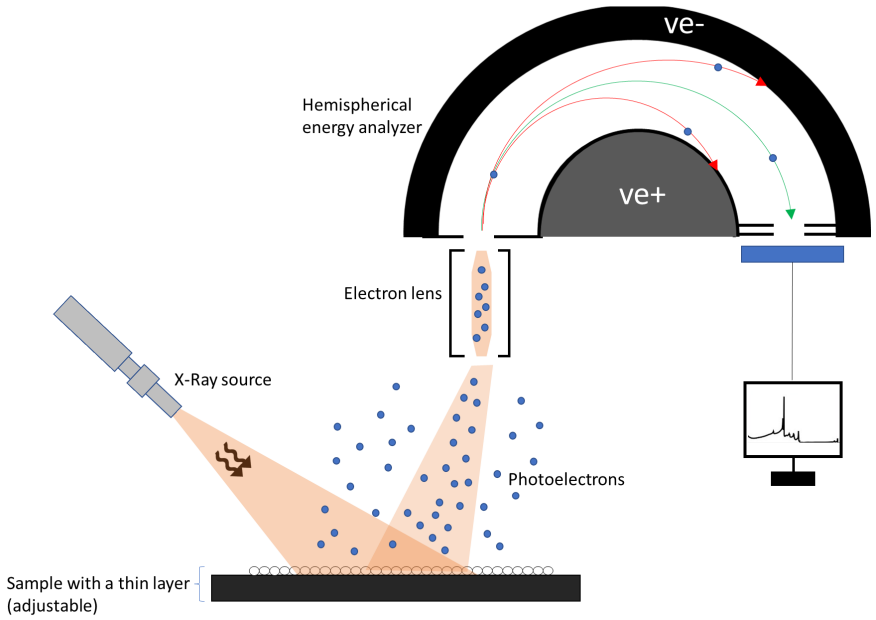

Figure 21. XPS scheme

In a simplified representation (Figure 21), XPS consists of a monochromator (an X-ray source), electron optics, a hemispherical analyser, an electron detector, and a UHV chamber. The sample is irradiated with a monochromatic X-rays beam (typically, $Al\,K_\alpha$: $h\nu = 1486.6\,eV$ or $Mg\,K_\alpha$: $h\nu = 1253.6\,eV$). The interaction of the

photons with the specimen leads to the photoelectric effect, where atoms lose electrons from the core levels. Such photoelectrons are emitted from the sample surface with characteristic kinetic energy (E_K):

$$E_K = h\nu - E_{binding} - \chi - \Delta E \quad (37)$$

Where $h\nu$ is an incident photon energy, $E_{bidning}$ is a binding energy of an electron in the atom, χ is a work function of a spectrometer, and ΔE is an electron energy loss in the path to the surface.

The energy of photoelectrons emitted as a result of X-ray radiation (with a known wavelength) is distinct, enabling qualitative analysis. An electron analyser measures the energy distribution of the electrons. It comprises electron optics that collect the electrons from the sample, retard and focus them onto the entrance of the hemispherical energy analyser. Subsequently, electrons with a specific energy (pass energy) can pass through the hemispherical analyser and reach the detector.

The pass energy for the analyser is a crucial parameter determining the energy resolution and intensity of the obtained spectra. Increasing the energy of electrons impinging on the detector (i.e., higher pass energy) leads to a rise in the signal-to-noise ratio but a reduction in spectral resolution. As a result, high pass energy is employed for acquiring a broad spectrum where high intensity is necessary for easy and rapid peak identification, while low pass energy is used for measuring high-resolution spectra to achieve better spectral resolution.

Quantitative data can be derived by examining the position, width, and specific area of individual peaks in XPS spectra. To determine the atomic percentage of elements present in the analysed material, the signal intensity (peak area) must be normalized by a relative sensitivity factor. This factor accounts for the probability of the photoelectric effect occurring for each chemical element.

The kinetic energy of a photoelectron is influenced by the valence electron density, and consequently, by the type of chemical bond to which the emitting atom is bonded. This results in a signal shift (also referred to as a chemical shift) in the range of 10^{-1} to 10^{0} eV. As a result, each photoelectron band for a specific element comprises multiple components that correspond to various chemical bonds within that element.

Interpreting the measured band is not straightforward, as each component's half-width is proportional to the chemical shift (shift in signal).

In non-conductive (electrically) samples, there is a band shift due to charge accumulation in the sample. This issue is solved by calibrating the energy to a known standard band, usually C1s of 265 eV.

XPS is a surface-sensitive technique, which means photoelectrons, without energy loss, can escape from the top 1-10 nm of the material. The depth of analysis is determined by the inelastic mean free path (λ_i) of the photoelectron in the material. Basically, 63 % of photoelectrons arise from the depth corresponding to 1x λ_i, whereas 95 % of photoelectrons come from the depth corresponding to 3x λ_i.

During the research, an X-ray photoelectron spectrometer equipped with X-ray source XR 50 (Al Kα 1486.6 eV, Specs) and hemispherical electron analyzer Phoibos 100 (Specs) was used. Wide spectra were acquired for binding energies in the 0-1100 eV range with pass energy 40 eV and energy step 0.5 eV. High-resolution spectra were acquired with pass energy 10 eV and energy step 0.1 eV. Charging of acquired spectra was calibrated using C1s peak with the position of 285 eV for C-C bonds. The data were processed using Casa XPS software, which also handles all the shifts.

3.4.3. Ultraviolet-Visible Spectroscopy

Ultraviolet-visible spectrophotometry (UV-Vis) is an absorption-based spectroscopy technique extensively utilized in chemistry, biology, and physics to determine the concentration of absorbing material in a solution. The primary principle involves examining electronic transitions resulting from low-energy radiation interacting with specimens. When exposed to radiation, electrons are excited from their ground state to higher excited states due to the absorption of radiation energy. Light in the ultraviolet and visible regions of the spectrum passes through the sample, and transmittance (T) is measured as the ratio of the intensities of light after (I) and before (I_0) passing through the sample as a function of a wavelength.

UV-Vis spectra could be expressed through the absorbance $A = -\log_{10} T$, a dimensionless quantity that measures the attenuation of light passing through the material. Various physical processes, including absorption, scattering, reflection etc., can cause absorbance. According to the Beer-Lambert Law, the absorbance of the

sample (A) is directly proportional to the concentration of absorber (c). The absorbance is then can be written as:

$$A = \log_{10}\left(\frac{I_0}{I}\right) = \epsilon \cdot l \cdot c \quad \textbf{(38)}$$

Where ϵ is the excitation coefficient of the material, l is the path length through the sample, c is a concentration of absorbing material, I_0 is an intensity of light before transmission through the sample, I is the intensity of light after transmission through the sample, A is the absorbance of the sample material.

***In situ* UV-Vis**

In situ UV-vis spectroscopy enables the examination of metallic NP formation and growth within the GAS. UV-Vis facilitates the identification and tracking of Localized Surface Plasmon Resonance (LSPR) peaks, as well as the changes in number and size of NPs based on the intensity, position, and shape of the peak. However, this method's limitation is that only a restricted range of materials (specifically plasmonic materials) can be effectively detected and analysed. Refer to Figure 13 for a typical GAS system featuring in situ UV-Vis spectroscopy within the aggregation zone. Silver (Ag) is an ideal material for in situ detection, as it displays a distinct and intense LSPR peak with a maximum at approximately 360 nm.

During the experiment, an Ocean Optics STS Microspectrometer with a functional wavelength range of 190-600 nm was employed in conjunction with an Ocean Optics DH2000 BAL light source (Ocean Optics, Inc., Ostfildern, Germany) for the measurements. Fibre optic cables from the light source and spectrometer were attached to quartz windows. A specialized optical system was utilized to generate a parallel light beam with a 1 cm diameter. The background was gathered in the absence of plasma. The UV-Vis spectra were captured with an integration time of 10 milliseconds.

***Ex situ* UV-Vis**

Ex situ UV-Vis, characterisation of NPs (copper and silver) deposited on the substrates allows the investigation of the LSPR peak of plasmonic NPs deposited onto quartz substrates. The Hitachi U-2900 spectrophotometer was used. The light source was equipped with deuterium and tungsten lamps for ultraviolet and visible spectral

regions. The measurements were performed in the wavelength region of 200 – 1100 nm.

3.4.4. Fourier-Transform Infrared Spectroscopy

Infrared (IR) spectroscopy is a technique based on the vibrations of the atoms of a molecule. An infrared spectrum is obtained by passing infrared radiation through a sample and determining what fraction of the incident radiation is absorbed at a particular energy. The energy at which any peak in an absorption spectrum appears corresponds to the vibration frequency of a part of a sample molecule. The relation between absorption and radiation is given by Lambert-Beer law, eq. (38).

For a molecule to show infrared absorptions (in the range of 4000-200 cm^{-1}), it must possess a specific feature, i.e.an electric dipole moment of the molecule must change during the vibration. This is the selection rule for infrared spectroscopy. The dipole moment of such infrared-active molecules changes as the bond expands and contracts. For infrared-inactive molecules, e.g., homonuclear diatomic molecules, the dipole moment remains zero no matter how long the bond is.

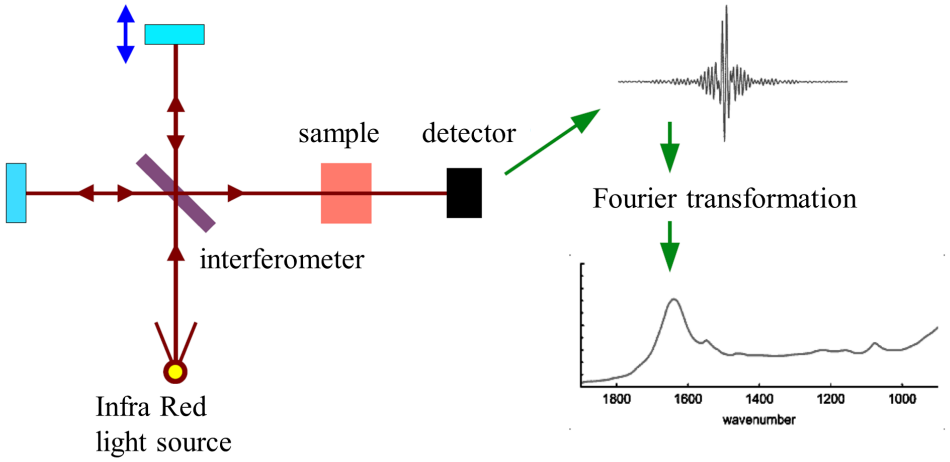

Figure 22. FTIR principles scheme

Fourier-transform infrared (FTIR) spectroscopy utilizes interference of radiation between two beams to yield an interferogram. The interferogram is a signal produced as a function of the change of path length between the two beams. The two domains of distance and frequency are interconvertible by the mathematical method of Fourier transformation. The advantage of FTIR over the conventional IR (with slit) is the

faster measurement time, better signal-noise ratio, and better calibration capabilities for the wavenumber.

Details for the FTIR analysis, theory, applications, interpretations and so on could be found in dedicated literature, for example, in [116].

In our experiments, FTIR measurements were performed using a spectrometer (Bruker Equinox 55) in a reflectance-absorbance mode. The spectra were recorded in the region of 4000 – 400 cm^{-1}. For these measurements, samples were deposited onto silicon substrates coated by a thin gold film. The resolution was set at 2 cm^{-1}. The spectra were processed using the software OPUS (BRUKER Optics).

3.4.5. Ellipsometry

Ellipsometry is an optical measurement technique that characterizes light reflection (or transmission) from samples. The key feature of ellipsometry is that it measures the change in polarized light upon light reflection (or transmission) on a sample. The name 'ellipsometry' comes from the fact that polarized light often becomes 'elliptical' upon light reflection. Ellipsometry measures the two values ψ (the amplitude ratio) and Δ (phase difference) between light waves known as p-polarised and s-polarised light waves. In spectroscopic ellipsometry, spectra *of* ψ and Δ measured by changing the wavelength of light. In general, the spectroscopic ellipsometry measurement is carried out in the ultraviolet/visible spectra region, but measurement in the IR region has also been performed widely.

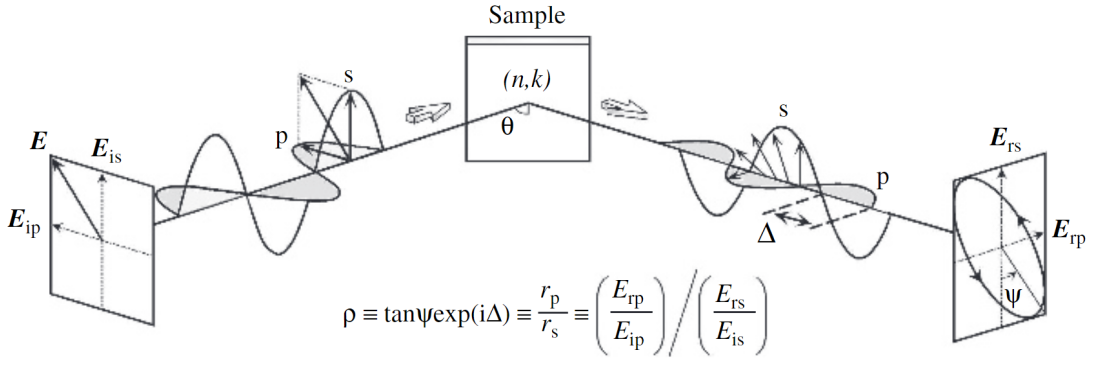

Figure 23. Principles of Ellipsometry. After ref. [117]

Measured ψ and Δ can then be used to determine a wide range of characteristics: film thickness, refractive index, surface roughness, interfacial regions, anisotropy

uniformity, and composition crystallinity. The complexity of the method constitutes in the fact that ellipsometry spectroscopy is a non-direct measurement technique. Desired information (e.g. thickness) must be extracted through a model-based regression analysis using equations to describe the interaction of light and materials. The software adjusts “fit” parameters to find the best match between the model and experiment. Ellipsometry spectroscopy is described in more detail in dedicated literature [117].

In this study, ellipsometry was utilized to assess the thickness of thin polymer films. A Woollam M-2000 DI ellipsometer was used for this purpose. Measurements were conducted at angles ranging from 55° to 75°. The Cauchy model was employed to fit the results and ascertain the coating thickness.

3.4.6. Scanning Electron Microscopy

Scanning Electron Microscopy (SEM) is one of the electron microscopy techniques for surface characterisation. A beam of accelerated electrons is emitted to the surface of the testing sample. The wavelength of electrons is much shorter compared to visible light, resulting in a higher imaging resolution than in a light-based microscope. The output of the SEM is an image of the surface topography, which is obtained by scanning the sample’s surface with the focused beam electrons. The resolution of such images could be as low as 1 nm, and in sophisticated systems, a depth profiling of the surface could be provided [118].

Typically, SEM consists of an electron gun, a set of focusing lenses, deflective coils and a combination of detectors (Figure 24). Electrons from a thermionic, Schottky or field-emission cathode are accelerated through an electrical potential difference between the cathode (which is in the electron source apparatus) and the anode. The voltage difference can be as low as 0.1 keV or as high as 50 keV [118]. Electrons pass through the set of lenses so that the electron probe could be in the range of 1 – 10 nm in diameter (or even 0.4 nm in case of the secondary electrons emission [119]). Scanning of the sample is done by pair of deflectors or, alternatively, scanning coils that allow deflection of the focused beam of electrons. The image formation is done due to the complete electron diffusion caused by the gradual loss of the electron energy and by lateral spreading caused by multiple elastic large-angle scattering [118]. The bombardment of highly energetic electrons on the surface results in the

emission of secondary electrons (SE), backscattered electrons (BSE), Auger electrons (AE), generation of X-ray radiation etc. The image is obtained from the collection of data about the beam position on the sample surface and the intensity of the acquired signal.

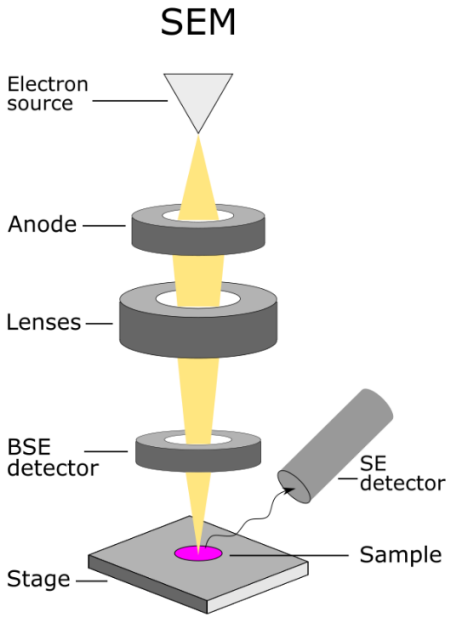

Figure 24. Schematic illustration of the SEM. BSE – Backscattered electron; SE – Secondary electron. (Adopted from https://anapath.ch/electron-microscopy-2/)

The SE mode for image formation is the most important because secondary electrons can be easily collected with a positively charged collector grid. Behind the collector grid, the SE is accelerated onto a scintillator positively biased (around +10 kV), and a photomultiplier records the light quanta generated. The SE yield depends on the tilt angle of a sample surface, the enhanced emission at edges and small particles and the shadow contrast that results from the incomplete collection can all be used to image the surface topography. In addition, the image's brightness depends on the number of SE collected by the detector, where dark spots on the image correspond to a smoother surface, and bright spots correspond to a rougher surface.

BSE move on straight trajectories and is not affected by electrostatic collection fields. The BSE detectors have to be mounted with a large solid angle of collection. BSE have high energy and could emerge from the inner parts of the sample (see Figure 25). The number of BSE depends on the atomic number of the material with which BSE interacts. Hence, the obtained data from the detected BSE can provide information about the distribution of different chemical elements in the sample.

More detailed information about SEM and its deferent variations (e.g., equipped with energy-dispersive X-ray spectroscopy (EDX) and others) can be found in dedicated literature [118]–[120].

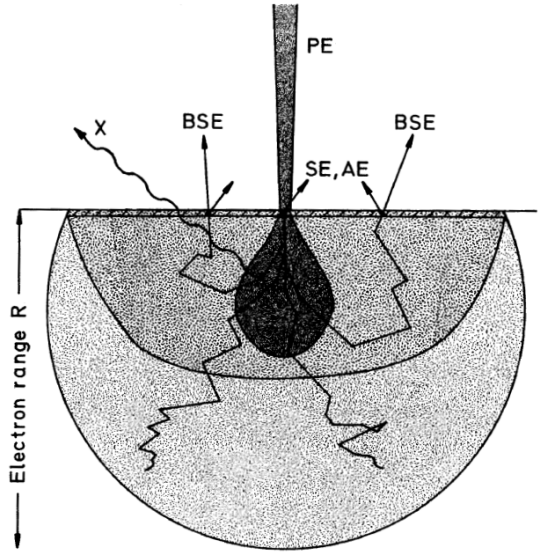

Figure 25. Origin and information depth of secondary electrons (SE), backscattered electrons (BSE), Auger electrons (AE) and x-ray (X) in the diffusion cloud of electron range (R) for normal incidence of the primary electrons (PE). Adapted from [118].

For this work, two SEM systems were used. One in Charles University, Prague, Czech Republic: Tescan Mira III that uses an in-beam secondary electrons detector mounted in the objective lens and Jeol JSM-7200F equipped with a high brightness Schottky field-emission (T-FE) electron gun, an In-Lens SchottkyPlusTM technology-based electron optics and hybrid objective lens. Another in Kiel University, Kiel, Germany: Supra55VP-Carl Zeis with in-lens detectors operated in a secondary electron mode for the topography measurements.

All the measurements were carried out either in the TTL (through-the-lens) or classical SEM mode with the acceleration voltage set to 5 kV. No additional metallization was applied towards the samples.

4. Results and Discussion

4.1. Magnetron Sputtering of PLA

Polylactic acid (PLA) polymer has gained a lot of popularity nowadays due to its advantageous properties such as biodegradability and biocompatibility, low level of toxicity and suitable processing properties; for example, for the fabrication, medical implants, scaffolds, or drug delivery systems, etc. [121]–[123]. Investigation results of the properties of deposited thin film sputtered from PLA target on silicon (Si) substrate are presented in the following section.

Under the experimental conditions reported in Section 3.1., the dependency of the deposition rate on the discharge power was investigated. The deposition rate is almost in linear dependency on the RF discharge power. If the PLA deposition rate is compared with the deposition rate of other polymers (PIB, LDPE, PE, and PP). We observe that in the lower power range (up to 50 W), the deposition rate of the PLA is significantly higher than that of LDPE, PE, and PP during the sputtering process, excluding the thermal co-evaporation part of the dependence, where the lifetime of the target is very limited. At higher power ranges, target evaporation dominates over the sputtering process [48]. The dominance of the evaporation process can be determined by a rapid increase in the deposition rate compared with the RF power increase. During the sputtering deposition process, the target surface is heated by ion bombardment, and the target polymer material's low thermal conductivity strongly reduces the target cooling's efficiency. This results in the target surface melting and evaporation at high discharge powers, which subsequently leads to the target deformation and a fall in the deposition rate (Figure 27).

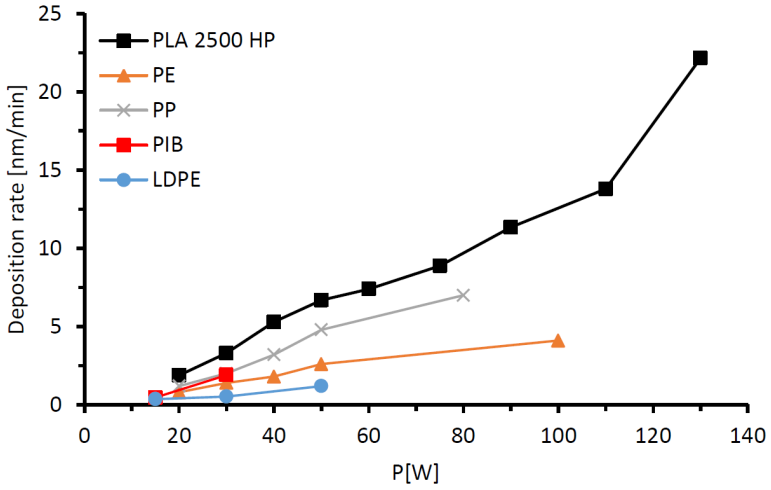

Figure 26. Dependence of deposition rate on RF discharge power for PLA 2500 HP, NatureWorks® (Ar pressure = 6 Pa, target thickness 2mm) — This works. For PIB (Ar pressure 5 Pa, target thickness 2mm), LDPE (Ar pressure 5 Pa, target thickness 3mm), PE (Ar pressure 4 Pa, target thickness 2.5 mm), and PP (Ar pressure 5 Pa, target thickness 1.5 mm) — [48]. Deposition rates are taken only for sputtering, excluding values for evaporation.

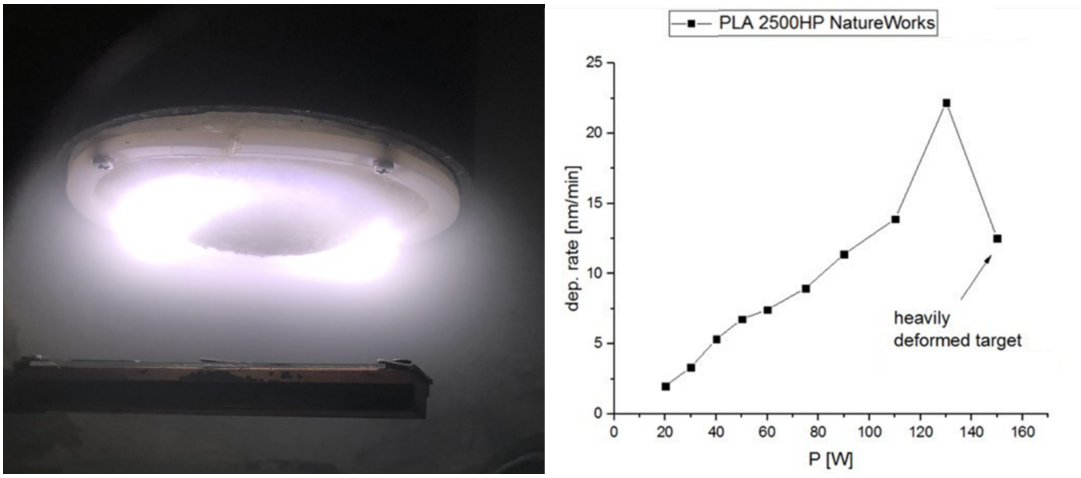

Figure 27. Left: observable PLA target deformation in magnetron sputtering at discharge power 150 W, Ar inlet 2 sccm, chamber pressure 6 Pa. Right: deposition rate of PLA against discharge power.

Chemical composition, specifically C 1s peak, analysed by XPS of the bulk PLA material and deposited thin film is shown in Figure 28. This figure indicates the C–C/C–H bonds (1) concentration increase compared with the original PLA polymer. The concentration of the C–C/C–H bonds has increased from 41.7 % in bulk to 76.5% in the deposited thin film on the expanse of C:O bonds. Double bond C=O (3), whose concentration is 3.4 %, indicates that some of the polymers of the PLA group are left in the deposited film. However, the rest of the bonds (C–O (2), O–C–O (4) in the b) show a typical plasma polymer property, which is a highly crosslinked structure. It is

fair to say that C:O bonds between curves “1” and “3” is hard to assign unambiguously because C:O peaks with various shifts can overlap due to the complex structure of the plasma polymer.

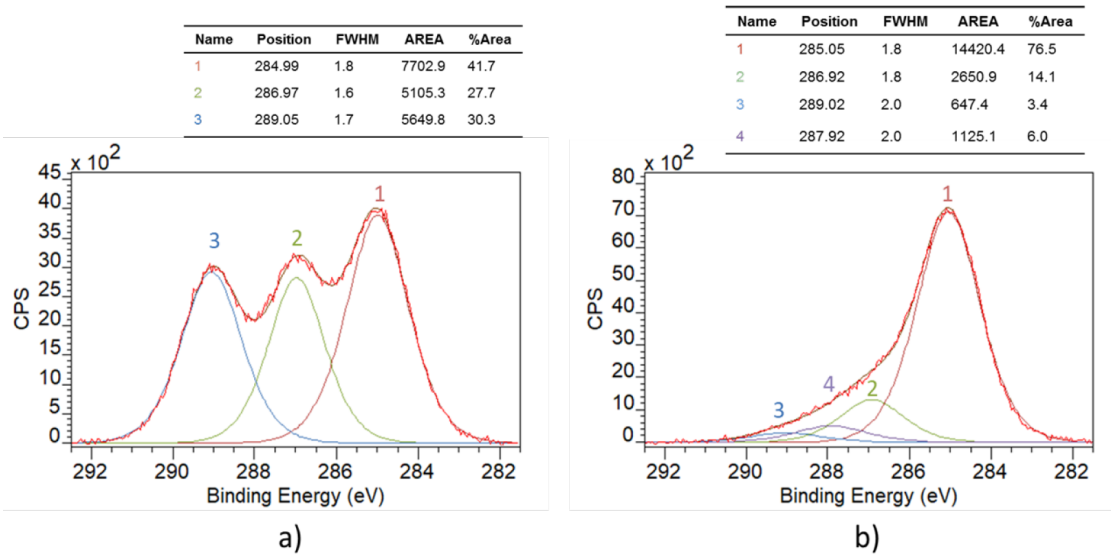

Figure 28. XPS result of the C 1s peak. a) Bulk PLA 2500 HP, NatureWorks® material. b) Deposited thin film by RF discharge magnetron sputtering of PLA 2500 HP, RF power 20W, Ar pressure 6 Pa, target thickness 2mm. Notation in the figure: “1” as C–C/C–H bonds; “2” as C–O bonds; “3” as C=O bonds; “4” as O–C–O bonds. Reference values were taken from [124].

The following is the analysis of the deposited thin film's C1s peak measured by XPS (Figure 28) and FTIR (Figure 30). Increasing RF discharge power of the magnetron sputtering is leading to the rise of C–C/C–H bonds concentration and decrease of C:O bonds concentration in the deposited film. FTIR analysis indicates the presence of cross-linking, and irregular structure can be expected due to C=C stretching vibrations (≈1650 cm^{-1}, overlapped with C=O peak). In addition, the spectra in the range between 2000–1400 cm^{-1} show that with the power increment, more CHx bonds and less C=O bonds are developed in the deposited film. The chemical analysis provided further evidence for a common idea of the enhancement of disorder in plasma polymers and the overall loss of the original polymer's motif at higher discharge power. Plasma-activated PLA sputtered monomers deposit on substrates and participate in recombination reactions, thereby providing cross-links.

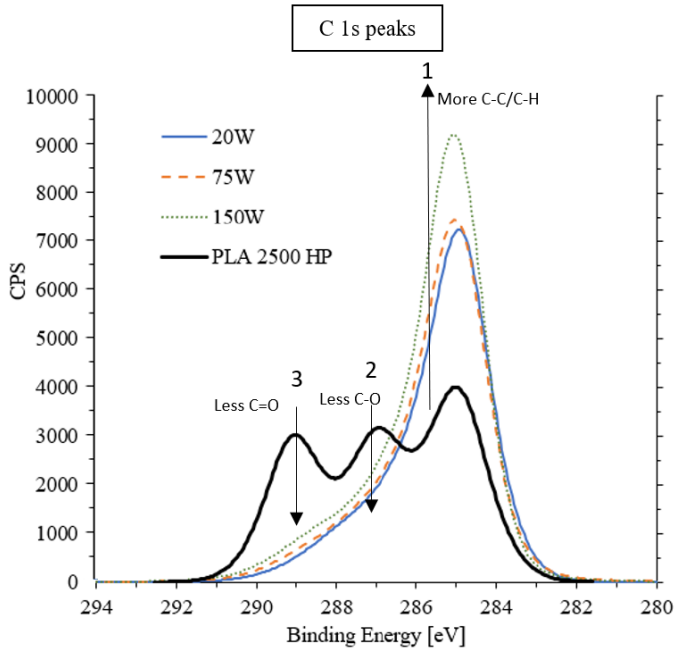

Figure 29. Comparison of the C 1 s of: bulk PLA 2500 HP, NatureWorks®; deposited film at 20 W RF discharge power; deposited film at 75 W RF discharge power; and deposited film at 150 W RF discharge power. Peak designations in the C 1 s diagrams, as "1", "2", and "3" are the same numbers as shown in the chemical structure diagram on the right.

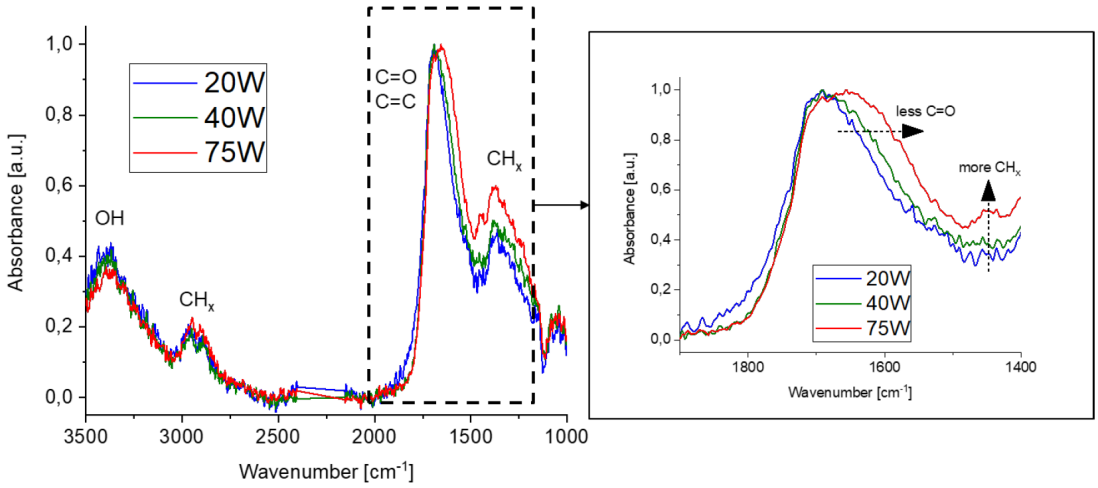

Figure 30. FTIR measurement of the deposited PLA 2500 HP (by NatureWorks®) film for various RF discharged powers.

PLA-based plasma polymer thin films can potentially be used as biocompatible surfaces. Furthermore, their functionality can be extended by loading them with metal NPs. For example, Ag NPs may provide bactericidal properties due to the release of silver ions. In contrast, the kinetics of such a release can be controlled by the cross-link density of embedding PLA plasma polymer. Such nanocomposite coatings can be produced by combining sputtering or PAVTD of PLA with the deposition of Ag NPs

using GAS, as it was implemented by the author in collaboration with another Ph.D. student Zdeněk Krtouš [125]. The experimental scheme of this approach is shown in Figure 31, whereas an example of the Ag/PLA coating can be seen in Figure 32, where the top-view SEM image is displayed.

It was noticed that the efficiency of the NP embedding into the plasma polymer strongly depends on the parameters of the GAS. On the basis of earlier studies [126]–[129], it was hypothesized that the interaction of NPs with the substrate can be governed by their kinetic energy, which should be optimized to avoid the rebounding of the NPs from the substrate. For example, for NPs with a mean diameter between 10 and 100 nm, the rebound may occur at velocities of around several tens of m/s [127]. Given the expertise of the author in CFD modelling, it was decided that the following experiments on Ag/PLA nanocomposites would be carried out by the collaborator within the frames of his Ph.D. work, while the author would focus on the investigation of the NP transport inside and outside the GAS to provide deeper insight to a problem that has not been explored in depth so far.

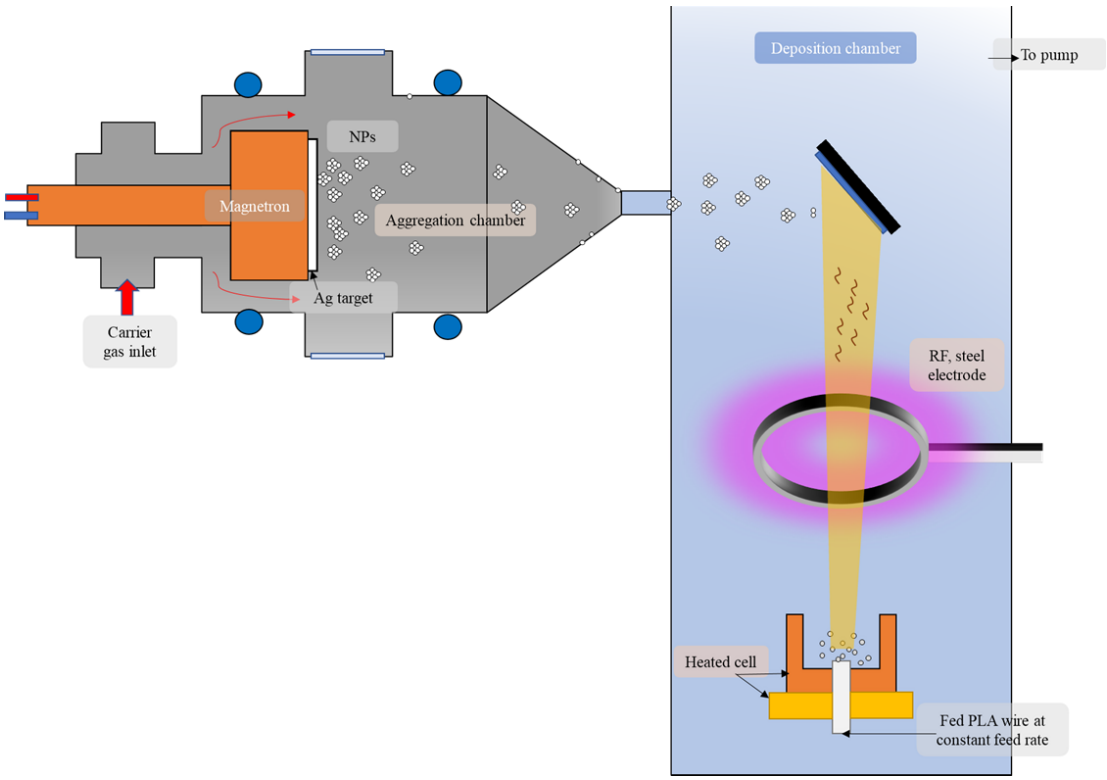

Figure 31. PLA plasma polymer and Ag NPs co-deposition system.

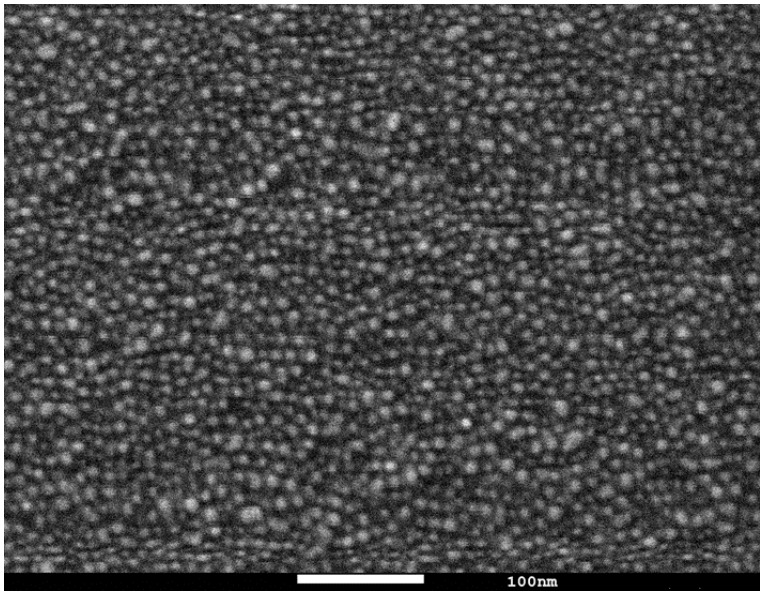

Figure 32. SEM image of the co-deposited Ag with PLA-based plasma polymers on Si substrate. The plasma polymer film was prepared by PAVTD (constant feed rate of PLA wire chamber pressure 2 Pa). NPs were fabricated by planar magnetron-based GAS (discharge current 250 mA, pressure 100 Pa). The holder with the substrate was 45° degrees tilted (plasma polymers and NPs impact the surface with the same angle)

4.2.Planar Magnetron GAS

As mentioned in the introduction section, at the beginning of the author's research work, the group investigated the mechanism responsible for the NPs trapping in magnetron-based GAS [73], [74]. In addition, NPs formation and transport to the substrate is of extreme importance for its deposition capabilities on the substrate, including ones with the plasma polymer films. One of the approaches to control NPs transport would be to investigate the flow of neutral noble gas inside the GAS. Due to the author's personal interest and professional experience in simulations, it was decided to explore deeper, by means of simulations, the processes inside the GAS by the flow of the neutral gas.

4.2.1. In situ UV-Vis measurement

In the experiment outlined in Section 3.2.1. NP detection in the vicinity of the magnetron using UV-Vis was carried out. During this process, the UV-Vis light beam interacts with the cloud of NPs, causing a plasmon resonance signal to emerge on the detector. The plasmon peak's position is influenced by particle size, while the full width at half maximum (FWHM) denotes dispersity, and peak intensity indicates the number density of NPs. Consequently, the in situ UV-Vis spectra obtained in GAS can be employed to study the formation and growth of metal NPs displaying plasmon resonance, such as silver NPs.

Throughout the experiment, UV-Vis spectra were initially recorded with the discharge turned off (background, as shown in Figure 33). Subsequently, the discharge was activated, and UV-Vis spectra were obtained at varying distances from the target connected to the magnetron within the GAS.

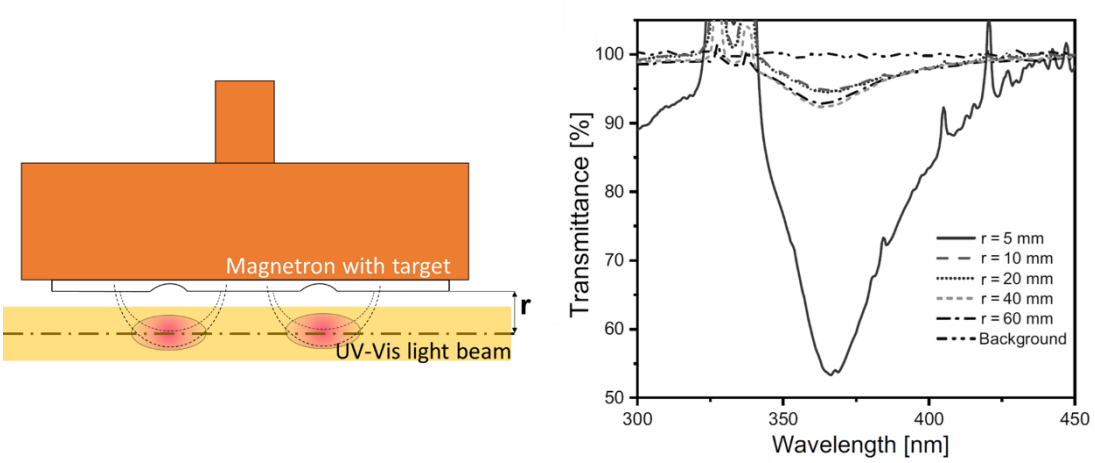

Figure 33 Left: A diagram illustrating the light beam probing the area near the magnetron. Right: UV-Vis spectra acquired at varying distances from the target, with the distance measured from the light beam's axis to the target plane.. Adapted from [98]

We may observe a high LSPR absorption peak in the 5 mm proximity of the target. The distance of 5mm was the minimum possible distance to measure because the light beam radius emitted from the UV-Vis light source was also about 5mm. The peak position at wavelength $\lambda = 365\,nm$ (or close to it), according to ref. [130], corresponds to the LSPR for Ag NPs. Increasing the relative distance between the light beam and the target leads to an abrupt decrease in the absorption intensity. However, it is important to note that the intensity did not fall down to the background level. It is also seen that the absorption intensity measured by UV-Vis remains approximately at the same level for longer relative distances.

The measured results can be interpreted as follows. A high absorption peak at the relative distance of $r = 5$ mm shows that there is an agglomeration or, so to say, a dense cloud of NPs. Whereas at further distances, Ag NPs flow at a relatively constant rate. This goes hand in hand with a measurement done with SAXS in DESY, Hamburg, where under similar experimental conditions and system (but except UV-Vis, SAXS was installed), there was observed NPs agglomeration in proximity to the magnetron, as shown in Figure 34.

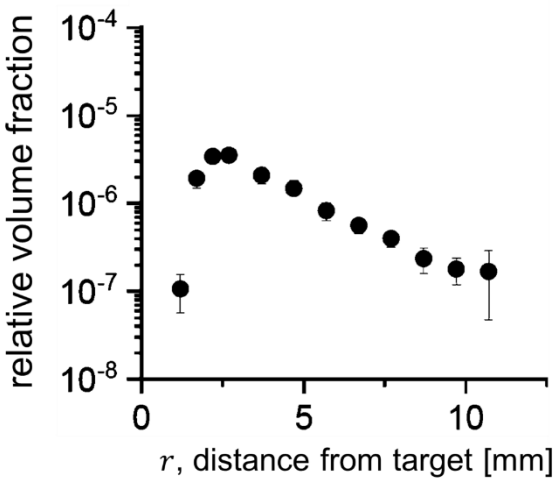

Figure 34. The distribution of relative volume fraction along the GAS longitudinal axis measured by SAXS for Ag NPs. Adapted from [74]

4.2.2. Forces on NPs in planar magnetron GAS

Measurement done with UV-Vis and SAXS indicate that there is a trapping of NPs happening in the proximity to target up to 5 mm. For NPs to be trapped, forces on NPs have to overcome drag force from neutral carrier gas flow and gravitational force. The NPs in a GAS source being submerged in a plasma environment can be charged, therefore, be affected by a complex of electromagnetic forces. Therefore, trapped NPs can be assumed to be in balance of forces such as: drag forces from the carrier gas, electromagnetic force, thermophoretic force (due to possible temperature gradient in the space surrounding the NPs), gravity, and ion drag force (the force induced onto the NP by the momentum transfer from directed fluxes of ions). However, for nanoscale particles, one should not underestimate the impact of the Brownian motion, especially for particles with diameters less than 30 nm. A schematic diagram of assumed forces acting on the NPs cluster is shown in Figure 35. There, gravitational force depends on the experimental setup. In our case, the gravitational force is oriented toward the orifice (outward from the magnetron). Drag force depends on the carrier gas flow direction. Thermophoretic forces tend to move light particles to hot regions and heavy particles to cold regions. Electromagnetic forces can virtually point in any direction depending on the charging of the NP and the plasma environment. Brownian force is a random motion of particles suspended in a fluid resulting from collisions with quick molecules/atoms of the carrier gas.

Therefore, the orientation of the force is random. The impact of the Brownian force is discussed in Section 4.3..

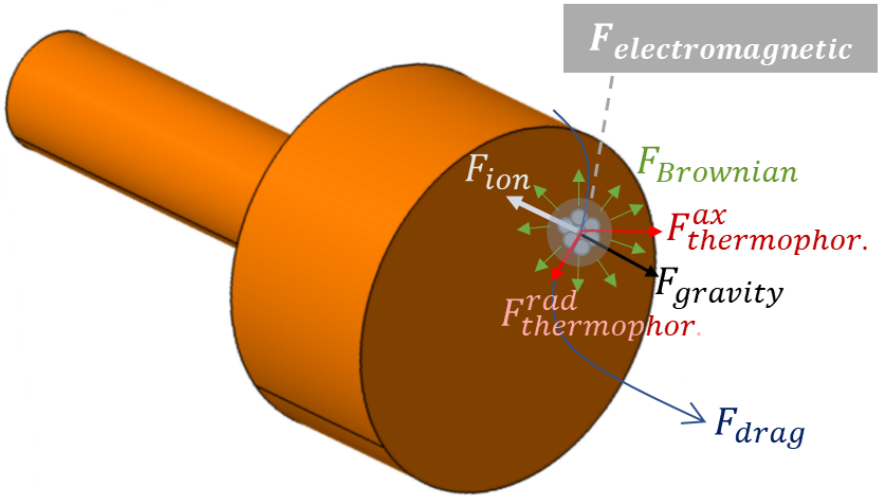

Figure 35. Schematic figure of possible forces acting on NP.

4.2.3. Carrier gas flow simulation in the planar magnetron GAS

So, what does the flow of carrier gas in that region? In order to understand the flow, CFD simulations were performed using commercial CFD software Siemens STAR CCM+. Simulations were performed using the same conditions and geometry as in the experiment. Simulation setups were discussed in Section 3.3.1.. Results for the flow velocity are shown in Figure 36.

At a 5 mm distance from the magnetron, it is seen that the carrier gas velocity is 0.002 m/s at the centre of the target and 0.04 m/s at the beginning of the target. At a 2.5 mm distance, the carrier gas flow velocity fell below 0.0005 m/s in the GAS centre axis region. If NPs are dragged exclusively by the carrier gas flow, i.e., by means of drag force only (only equation (23)), then trajectories for the NPs (Ø10 nm) will be as shown in Figure 37. We can observe that NPs tend to move towards the central axis of the GAS (following the carrier gas motion) and then towards the orifice.

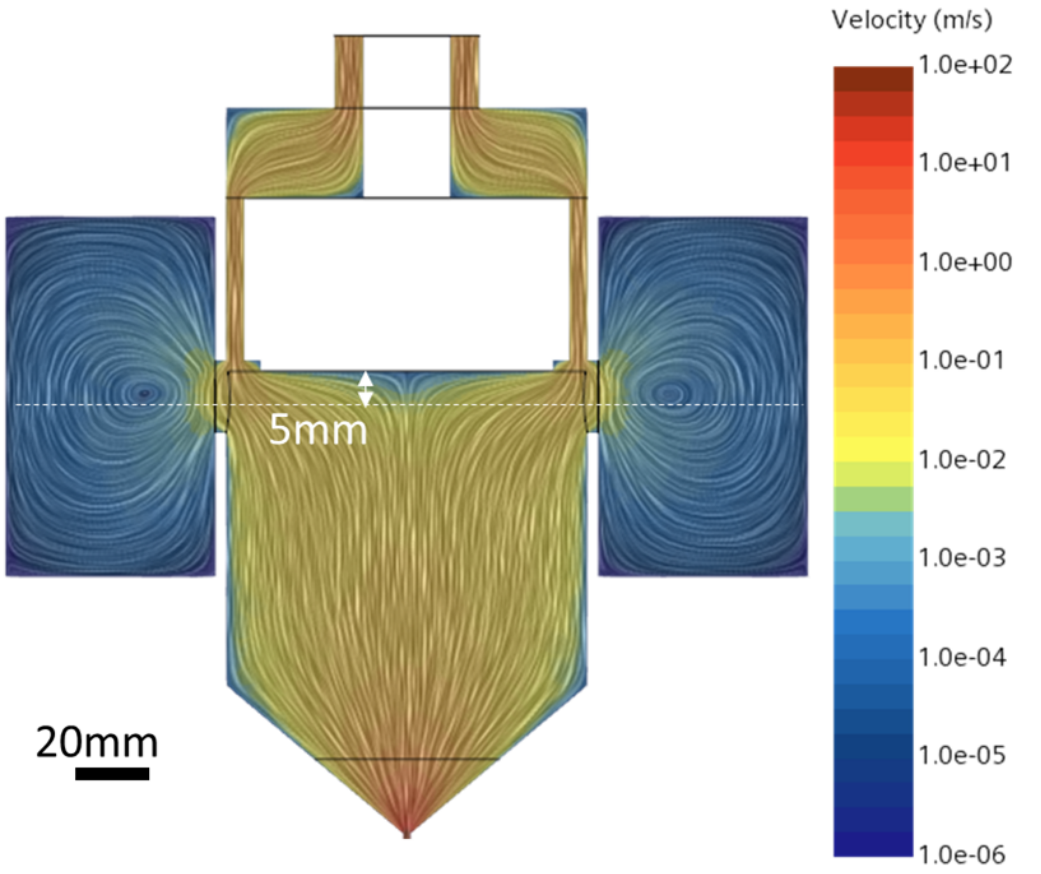

Figure 36. CFD Simulation of the Ar flow in the vicinity of a magnetron. Inlet flow rate 18 sccm, deposition chamber pressure 133 Pa.

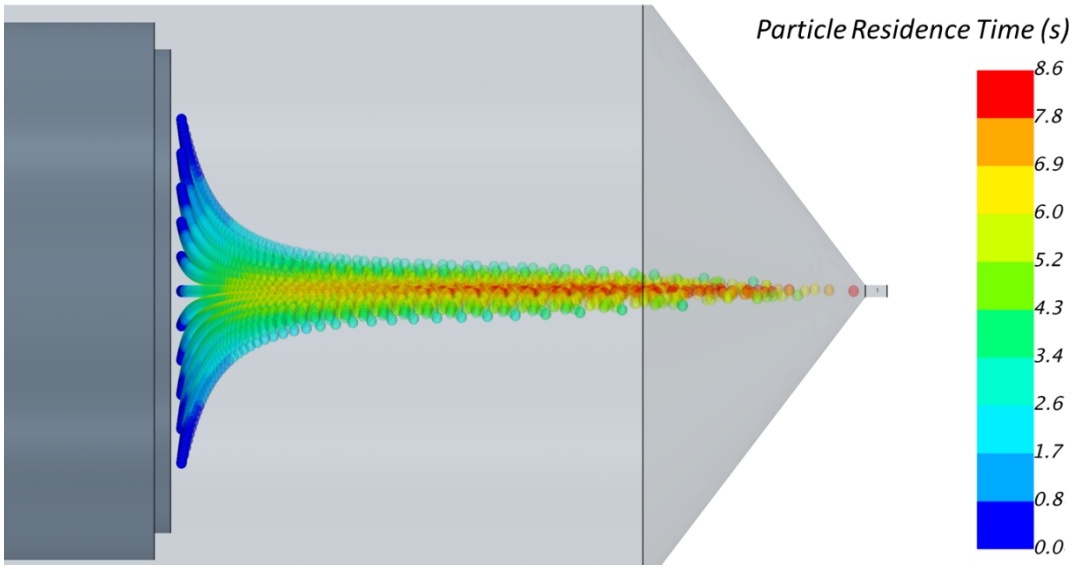

Figure 37. NPs of diameter 10 nm in the GAS. Only drag force accounted for. Colours represent particle residence time

4.2.4. Time-resolved UV-Vis measurement in planar magnetron GAS

From the UV-Vis (Figure 33), SAXS (Figure 34) measurements, and CFD simulation (Figure 36), we can see that the region of NPs trapping corresponds to the region of very low carrier gas velocity profile, as well as the plasma electron trap region. From this, we can suggest that the low velocity creates an insufficient aerodynamic force (drag force) to escape electrostatic forces created by the discharge. Time-resolved UV-Vis measurement can provide evidence for that suggestion.

Under the experimental condition described in Section 3.2.1. (the same as the ones we are discussing now), time-resolved UV-Vis measurements were conducted before and after deactivating the magnetron discharge. In this specific experiment, the relative distance between the target surface and the light beam axis was r=15 mm. While the discharge was active, spectra were collected at 0.1-second intervals with a 100 ms acquisition time. After parameter stabilization, the discharge was turned off, but spectra acquisition continued. The measurements are displayed in Figure 38. The moment when the plasma was still on (and stabilized) but was immediately switched off afterward was considered as the reference time point, 0.0 s. At 0.0 s of relative time, Ag atomic emission lines are visible. When the discharge was deactivated, the emission lines vanished, but the LSPR band persisted. At 0.5 s of relative time, a sharp increase in LSPR intensity is observed. This implies that 0.5 s after the plasma is turned off, the trapped NPs, carried by the gas flow, reach the light beam situated 15 mm away from the target. As the trapped NPs pass through the measurement area, the LSPR band intensity decreases to the background level.

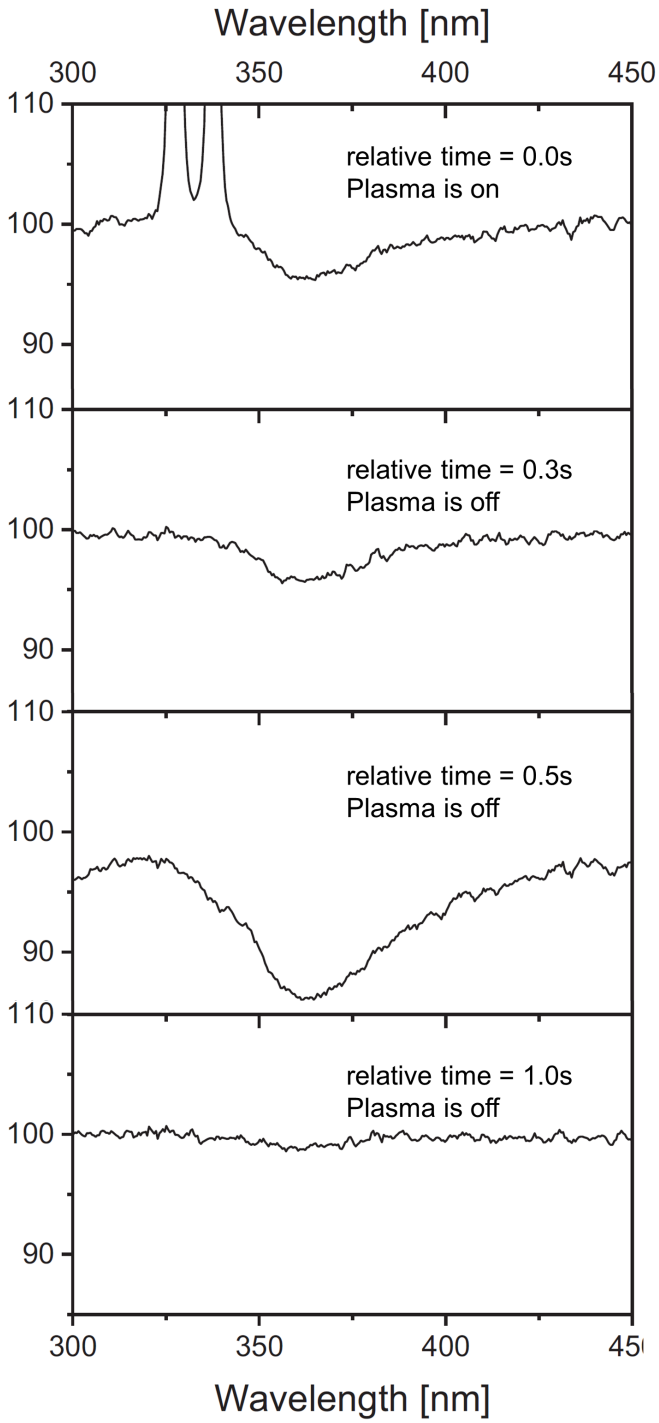

Figure 38. Time-resolved UV-Vis spectra were obtained at r = 15 mm. Reference time when discharge was switched off was taken as 0.0 s, and the relative time to the reference time is shown in the figure. Adapted from [98]

4.2.5. Impact of the inlet configuration on gas flow in the planar magnetron GAS

Naturally, the question may arise, what if we increase the carrier gas velocity? To substantially increase the gas flow velocity in the target region, the gas inlet configuration can be changed. Two typical gas inlet configurations exist on the GAS: rear inlet—from behind the magnetron and magnetron inlet—implemented within the magnetron. Both are schematically shown in Figure 39.

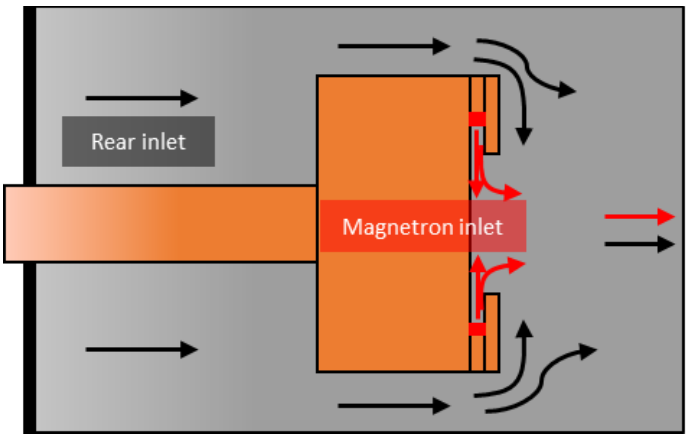

Figure 39. Schematic drawing for the GAS inlet configuration. The rear inlet configuration is shown in black, placed behind the magnetron. The magnetron inlet configuration is shown in red, where the inlet is implemented to enter the magnetron radially. From ref. [99].

For reference, flow simulation was provided for both inlet configurations under similar conditions (24 sccm inlet flow rate, 50 Pa aggregation chamber pressure, 293.15 K fluid temperature). Figure 40 shows that the flow velocity is of one magnitude lower in the near magnetron (or near target) region in the case of the rear inlet configuration. This indicates that the magnetron inlet configuration is essential to GAS performance. Indeed, as it was shown by Sanzone *et al.* [94], the rear inlet configuration led to substantially worse GAS performance (in terms of NP mass flow from the aggregation chamber) than the magnetron inlet configuration. Especially when single atoms were ejected from the target, the drag had no influence on the particle. Hence, the particle was diffused predominantly by the Brownian motion (the influence of the Brownian force on particle motion is yet to be discussed in Section 4.3.). In that case, particles may freely and randomly move in any direction, depositing on the walls and the target or escaping the aggregation chamber, but at a much lower rate. Furthermore, the spatial distribution of single atoms in terms of their

number density was better in the magnetron inlet configuration, providing ~1.3 times higher amount of sputtered atoms available for cluster formation [94].

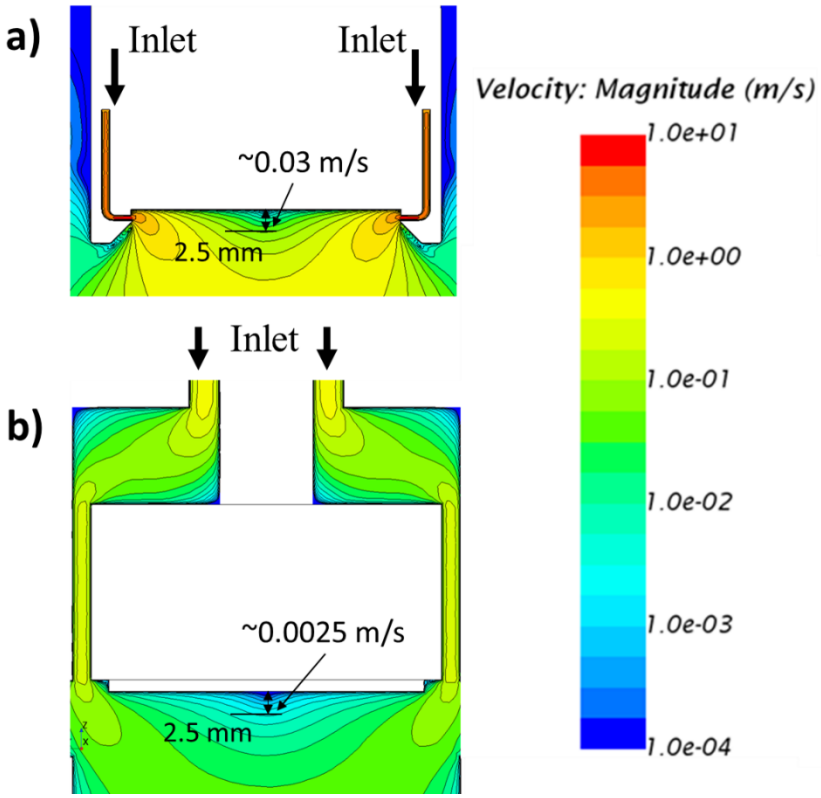

Figure 40. Comparison of the gas flow velocity for different inlet configurations. (Ar flow is 24 sccm, the chamber pressure is 50 Pa, and T_f is 293.15 K): (a) magnetron inlet; (b) rear inlet. From ref. [99]

4.2.6. Planar magnetron GAS with magnetron inlet configuration

Another set of experiments was done under similar conditions as reported in Section 3.2.1., however, with certain differences. There was employed a 2-inch (50 mm) magnetron with the possibility to adjust the aggregation length. The argon gas was injected into the GAS through the magnetron ground shield, allowing for gas delivery directly to the target surface. A conical orifice of 3 mm diameter was used between the aggregation and deposition chamber. For 24 sccm inlet gas flow rate, the pressure inside the chamber was 49 Pa. Magnetron was supplied with 100 W power over all experiments. The GAS was equipped with two quartz windows and a UV–Vis spectroscopy setup (Light source: Deuterium/Halogen lamp DH-2000BAL; Detector: Ocean Optics, HR 4000CG-UV-Nir; Ocean Optics). The light beam diameter of the UV–Vis spectroscope is 14 mm. The simulation setup was described in Section 3.3.2..

The result of the flow simulation for 24 sccm inlet flow rate for an initial aggregation length of 220 mm (corresponding to $r = 7$ mm, a relative distance between the target and light beam axis, as shown in Figure 33) is shown in Figure 41 as a convolute velocity vector field scene.

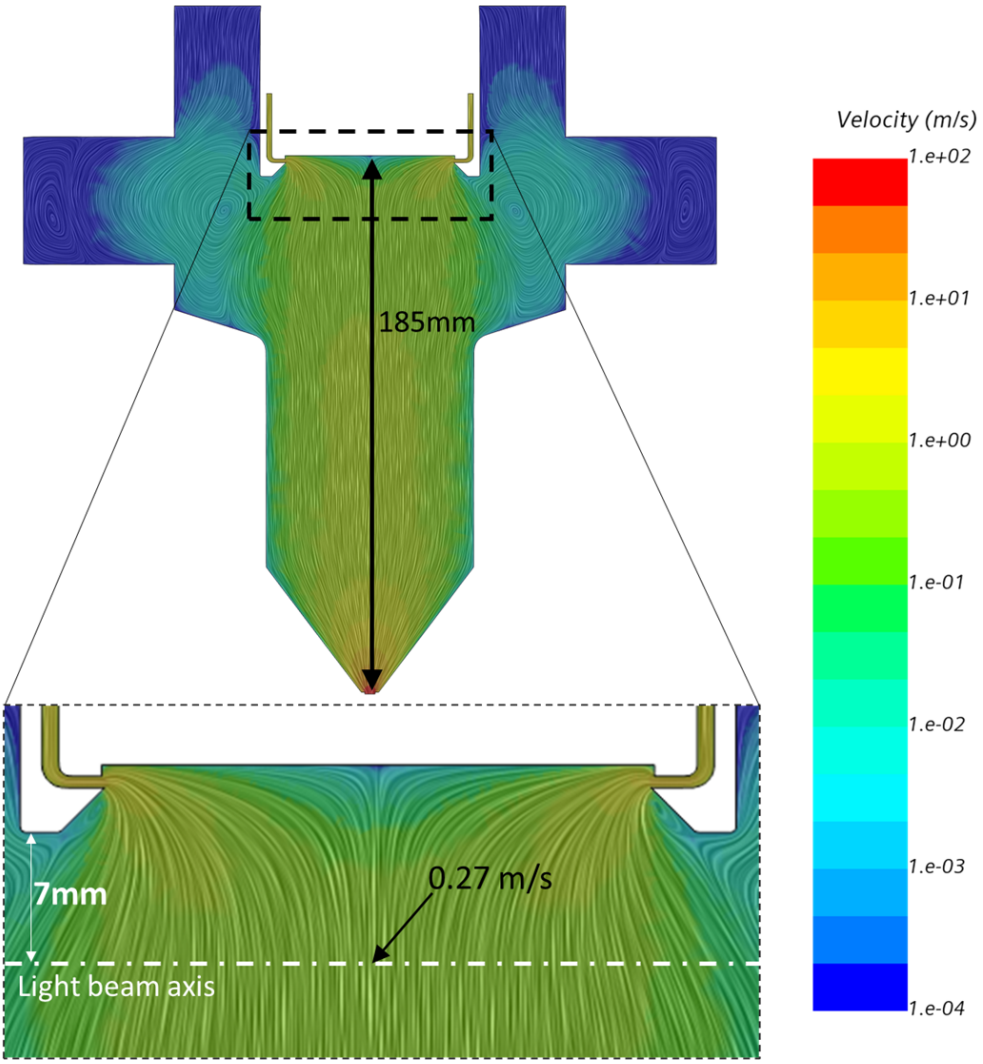

Figure 41. Magnetron inlet GAS configuration. Inlet flow: 24 sccm, aggregation chamber pressure: ~50 Pa, Aggregation length 185 mm.

Flow simulation results for three different aggregation lengths (155 mm, 165 mm, 185 mm) and 24 sccm inlet flow rate (~50 Pa chamber pressure) are shown as a scalar velocity field in Figure 42. UV-Vis was also measured for the given inlet flow rate and varying aggregation length, as shown in Figure 43. From there, we see (comparing against rear inlet configuration GAS, Figure 33) that the strongest LSPR has been shifted to a bigger distance in the case of the higher flow rate. To understand if that shift appeared due to higher carrier gas velocity or due to a changed inlet

configuration, we increased the inlet flow rate from 24 sccm to 60 sccm and repeated the experiment. Results of which are shown in Figure 44 and Figure 45.

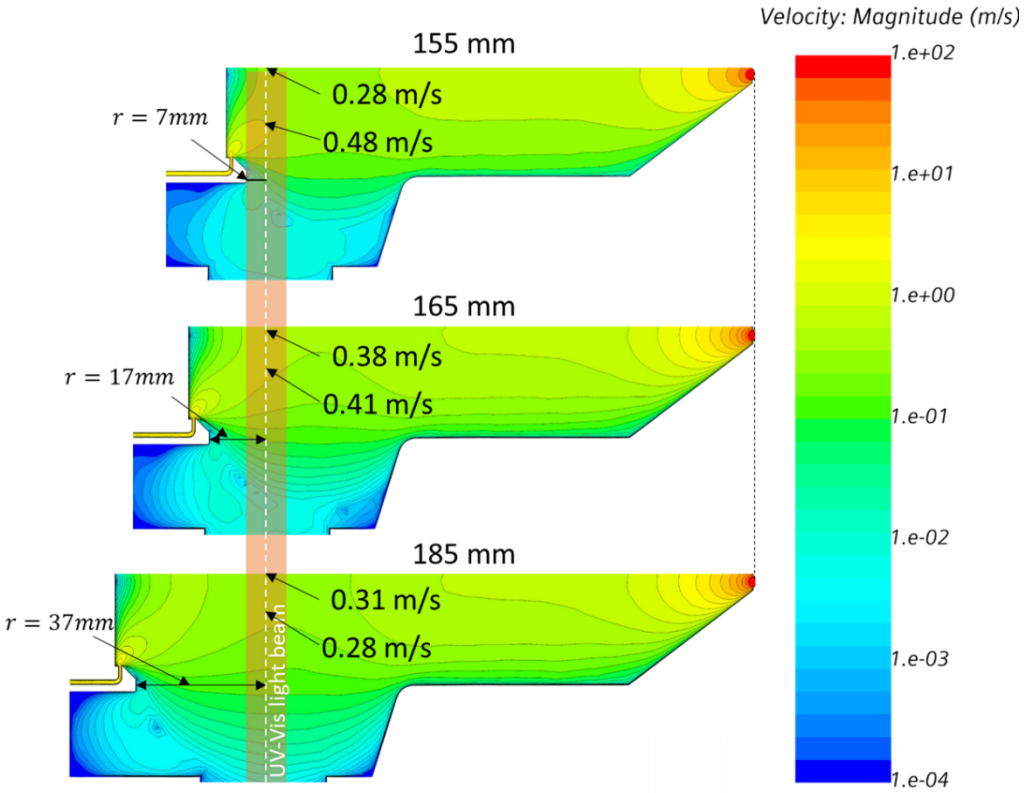

Figure 42. Gas flow velocity in magnetron inlet GAS configuration at 24 sccm, ~50 Pa, for different aggregation lengths. From top to bottom: 185mm, 195mm, 215 mm

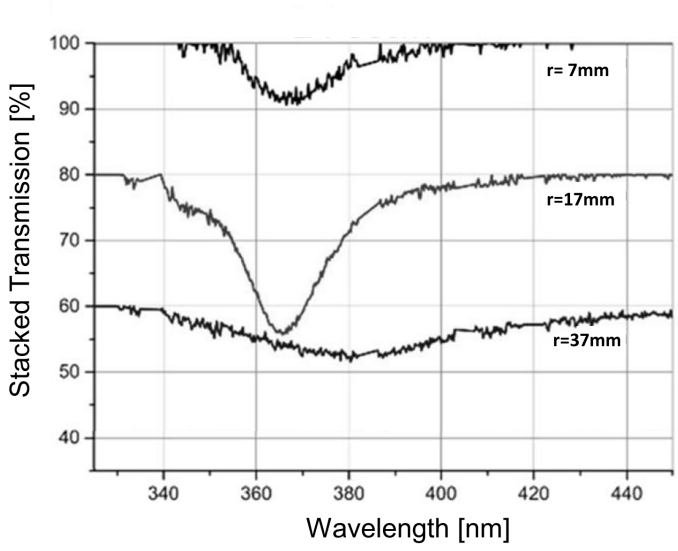

Figure 43. UV–Vis spectra at 24 sccm at different relative distances between the target and the light beam axis, r, for stabilised discharge. Adapted from [97].

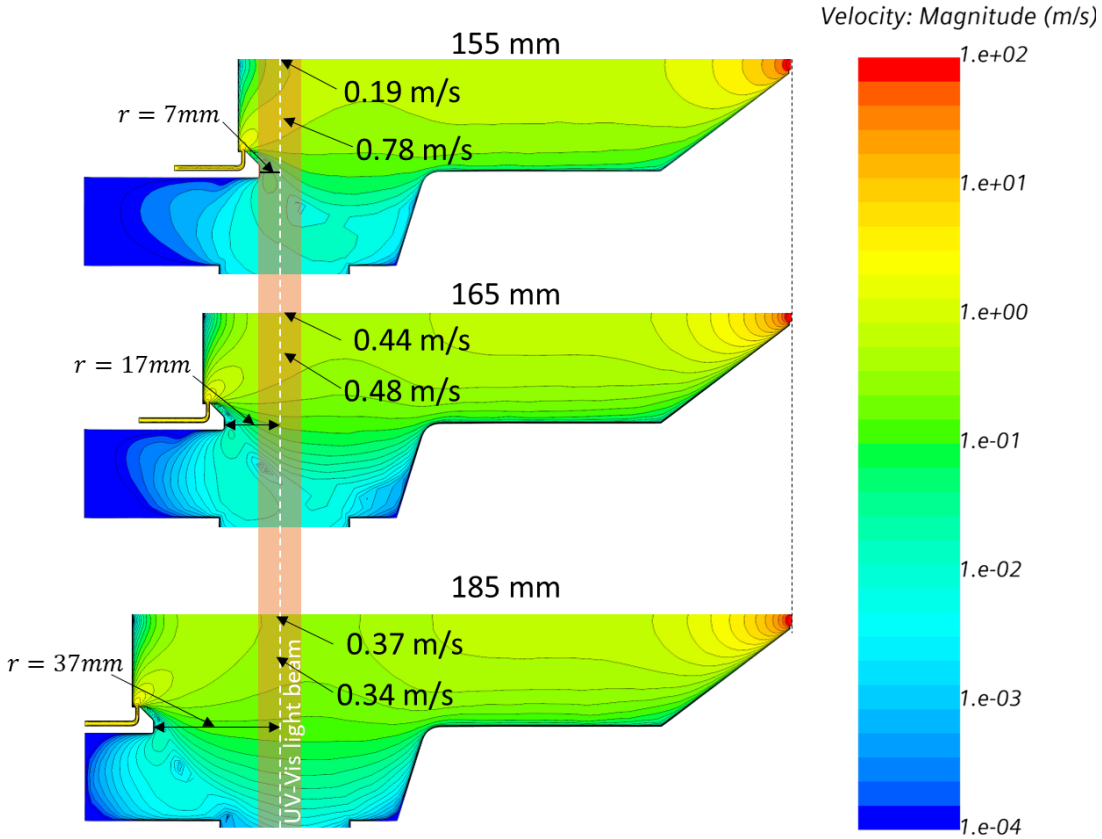

Figure 44. Gas flow velocity in magnetron inlet GAS configuration at 60 sccm, ~113 Pa, for different aggregation length. From top to bottom: 155mm, 165mm, and 185 mm

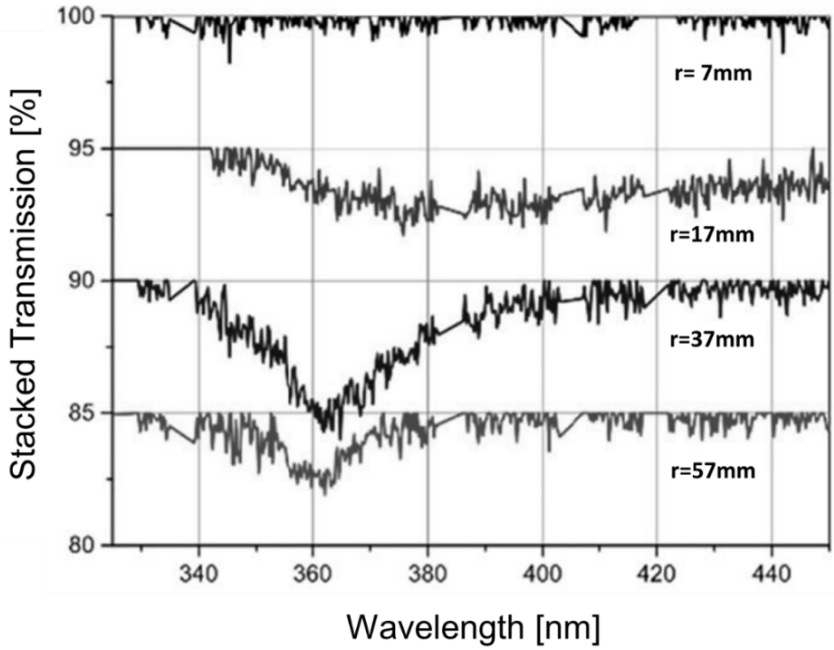

Figure 45. UV–Vis spectra at 60 sccm at different relative distances between target and light beam axis, r, for stabilised discharge. Adapted from [97]

Comparing UV-Vis spectra between 24 sccm and 60 sccm, we can clearly see that the trapping region moved towards the orifice, indicating that the gas flow velocity plays a vital role in trapping location. Here we must remember that the power supply to the magnetron (100 W), hence, discharge parameters remain the same for all inlet flow rate and aggregation lengths cases. This means only changed inlet flow rate (subsequently gas flow velocity and chamber pressure) is responsible for the trap region shift. Furthermore, analysing the SEM image of the substrate for NPs size distribution for 24 sccm and 60 sccm (Figure 46), we see that no particles of diameter > 40 nm were deposited. We can interpret that increasing the inlet flow rate (hence pressure) did not lead to bigger NPs being extracted from the Habreland-type GAS system under a given configuration. However, there was a benefit in increasing the inlet flow rate. QCM results (shown in Figure 47) show that the number of extracted/deposited NPs, with a diameter < 30 nm, increases with the increasing inlet flow rate.

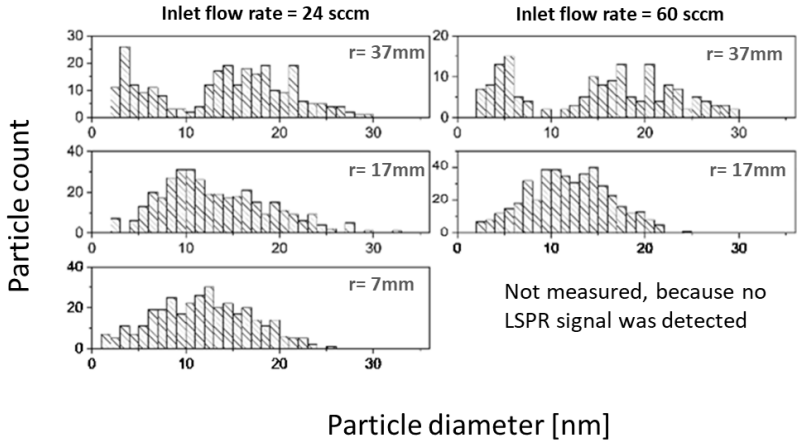

Figure 46. Size distributions of Ag NPs out of SEM images at different relative distances between target and light beam axis, r. The inlet flow rate of 24 sccm and 60 sccm, discharge power is 100 W. Adopted from [97]

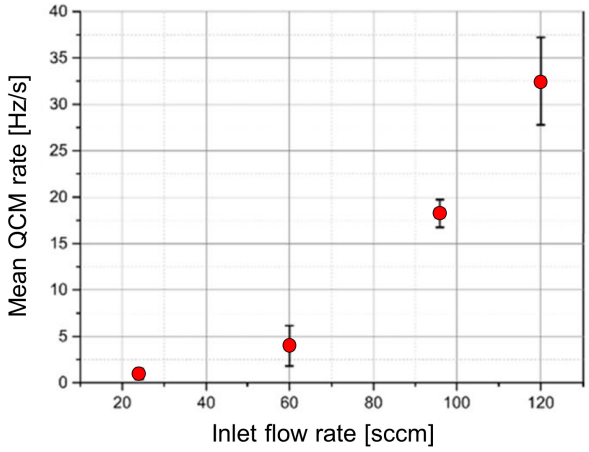

Figure 47. The deposition rate of Ag NPs measured by QCM vs inlet flow rate. Adopted from [97]

4.2.7. Analysis of CFD simulations for planar magnetron GAS

Intuitively, one may deduce that the carrier gas velocity increased by increasing the inlet flow rate. This is definitely true, however, if we analyse CFD results, we will see that the increase is not that abrupt. Let us measure the carrier gas velocity magnitude values in curves shown in Figure 48a, with results shown in Figure 48b,c, for 24 sccm and 60 sccm for two different aggregation lengths (hence the relative distance between the target and UV-Vis beam light). Please note that changing aggregation length also changes the relative distance r, between target and the light beam axis, and vice-versa. Hence, for example, for aggregation length of 165 mm corresponds to a $r = 17$mm relative distance, for 185 mm aggregation length $r = 37$mm.

From the Figure 48b (Curve 1), we see that the gas velocity is "zero" at the centre of the magnetron/target, which is expectable since, at this point, velocities from the radial inlet meet, cancelling each other's radial component of the velocity leaving only small fraction of axial component of the velocity. At the same time, Figure 48c (Curve 2) measures velocity from the inlet channels (the graph is adjusted to start from the closest to the target distance, right after the inlet channel). Therefore, at the proximity to the target gas flow velocity is not zero.

Now, let us look closely at Figure 48b (Curve 1), specifically at the dotted blue curve (24 sccm/165mm agg.len curve). At a 17 mm distance (according to Figure 43, at this point was a peak LSPR measured by UV-Vis for 24 sccm), the gas velocity is about ~0.4 m/s. Keeping it in our mind, let's focus now on the solid orange curve (60sccm/185mm agg.len curve). In this case, at a 37 mm distance (according to Figure 45, at this point was a peak LSPR measured by UV-Vis for 60 sccm), the velocity is ~0.35 m/s. We will obtain similar results from Figure 48c. This suggests that the drag force at 24 sccm developed at a 17 mm distance by 0.4 m/s gas velocity is in balance with other forces (Figure 35), trapping the NPs. When we increased the carrier gas velocity at this point (17mm), trapping was shifted to the region where again, we had the drag force corresponding to 0.4 m/s. Please note that the trapping region at $r = 37$ mm for 60sccm flow could appear slightly earlier than at 37mm. For instance, as Figure 48b and c) suggest us, the trapping could happen at a distance of around 31-35 mm distance from the magnetron. It is also important to note that force balance in the plasma environment is highly complex, and retaliation to the drag forces is not that

straightforward. However, some indications and trends CFD analysis may provide, which we are currently doing.

In magnetron sputtering systems, the plasma properties are not perfectly uniform. The plasma characteristics, such as density, temperature, and potential, vary significantly across the chamber. The degree of uniformity depends on various factors, including the aggregation length, target size, chamber geometry, and magnetic field properties. Generally, the plasma uniformity is better over distances on the order of a few centimetres from the target [131]–[137]. We may deduce that the spatial parameters of a stabilised plasma do not vary drastically within a few centimetres from the magnetron. For our experiments, we did not provide plasma characterisation. Therefore, the suggestion that the plasma properties at the distances of ¿37mm and ¿17mm are uniform remains hypothetical.

Looking at Figure 48c (which captures the velocity of the carrier gas near the erosion zone, see Figure 7), we see that the velocity is not rising from 0 m/s to higher values. Rather, velocity decreases from higher values (exit from inlet channel) to smaller values. Therefore trapping is not happening at closer distances. Perhaps, if the inlet flow rate, hence the carrier gas velocity, were decreased even more, then the trapping region distance from the planar magnetron would also decrease, assuming the plasma properties would remain the same.

In addition to our earlier observation, graphs in Figure 48 show that even though we increased the inlet flow rate from 24 sccm to 60 sccm, the carrier gas velocity did not increase at the same rate, hence the drag force too. That might help us to explain why with the increased inlet flow rate we did not see NPs of bigger size (>40nm, according to Figure 46). CFD analysis suggests that this could be because the velocity increased by approximately +0.1 m/s for 60 sccm compared to the 24 sccm inlet flow rate.

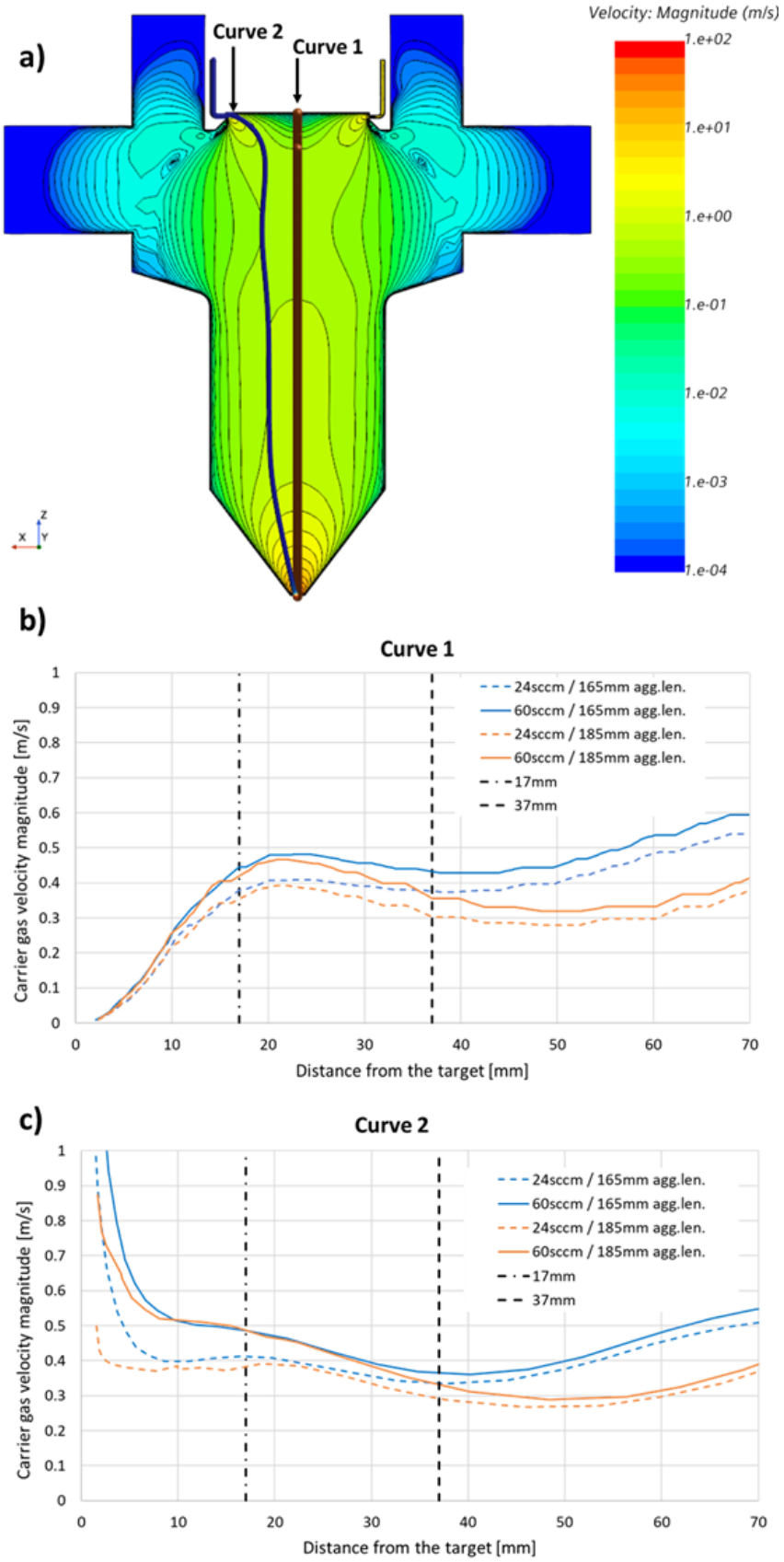

Figure 48. Carrier gas velocity analysis for 24 sccm (~50 Pa, dotted curves) and 60 sccm (~113 Pa, solid curves) for aggregation lengths 165 mm (blue curves) and 185 mm (orange curves). a) Curves, along which the gas velocity is measured, b) Curve 1 results, c) Curve 2 results.

4.3. Impact of Brownian force on NPs motion.

The definition of the Brownian force has already been given in Section 2.5.. It is essential to remind that the Brownian force depends on the random gaussian factor ς_i (see eq. (28)). Variables for ς_i over 1000 samples can be seen, as an example, on the Figure 49.

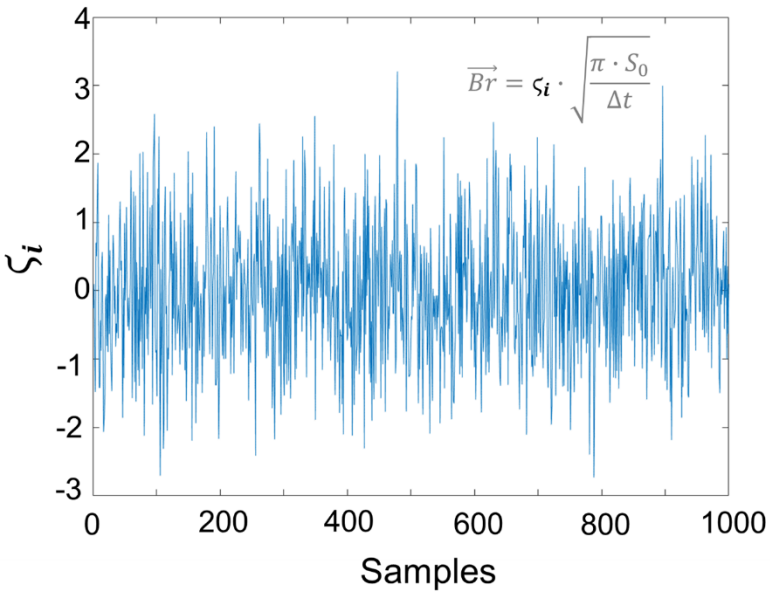

Figure 49. Random Gaussian factor values over 1000 samples.

Figure 50a shows the zero-mean unit variance Gaussian probability distribution, where the colour gradient and vertical axis indicate the probability of the value of the random gaussian factor ς_i. The highest probability of 40% (dark colour) corresponds to ς_i=0. At higher absolute values of ς_i, the probability decreases and approaches zero for $|\varsigma_i| > 3$ (white transparent colour).

Figure 50b shows the dependence of Brownian force and, for comparison, drag force (eq. (23)) on the size of NPs and Figure 50c shows the magnified region of small NPs. Solid curves represent various gas velocities, and the transparent colourmap corresponds to the Brownian force probability distribution. For instance, if an NP of 50 nm diameter is placed in the gas flow of 0.1 m/s, it experiences the drag and the Brownian force of approximately 10^{-16} N. However, the drag force is deterministic, whereas the Brownian force is stochastic. Brownian force value lies in the dark colour region, corresponding to high probability. Thus, the drag and the Brownian force contribute to the NP movement. If the same 50 nm NP is put into the gas flow of 1

m/s, both forces reach the value of 1.2×10^{-15} N; however, the Brownian force has a negligible probability (shown by the white colour and the dotted line corresponding to $|\varsigma_i| = 3$) and, therefore, the trajectory of NPs is contributed almost exclusively by the drag force.

Looking at Figure 50b and c from a broader perspective, it can be concluded that NPs of all sizes experience the drag and Brownian forces if the gas velocity is lower than 0.1 m/s. Higher gas velocities favour the drag force over the Brownian force, and the NPs will predominantly follow the gas stream. Expectedly, the drag force domination is more substantial for larger NPs. An almost similar impact of Brownian and drag forces was also shown by Zhang et al. [91], where NPs followed the gas flow but with significant disturbance due to the Brownian force. For a gas velocity > 1 m/s and the NP size > 20 nm, the drag force overcomes the Brownian force of the more probable magnitude, i.e., NPs will follow the gas stream. Therefore, the higher gas velocity is preferential for better control over the NP transport, while re-depositions on target or wall losses are less likely. In addition, bigger NPs are more controllable by the gas flow than smaller particles. Consequently, the gas velocity has to be as high as possible to limit the influence of the Brownian motion on NPs.

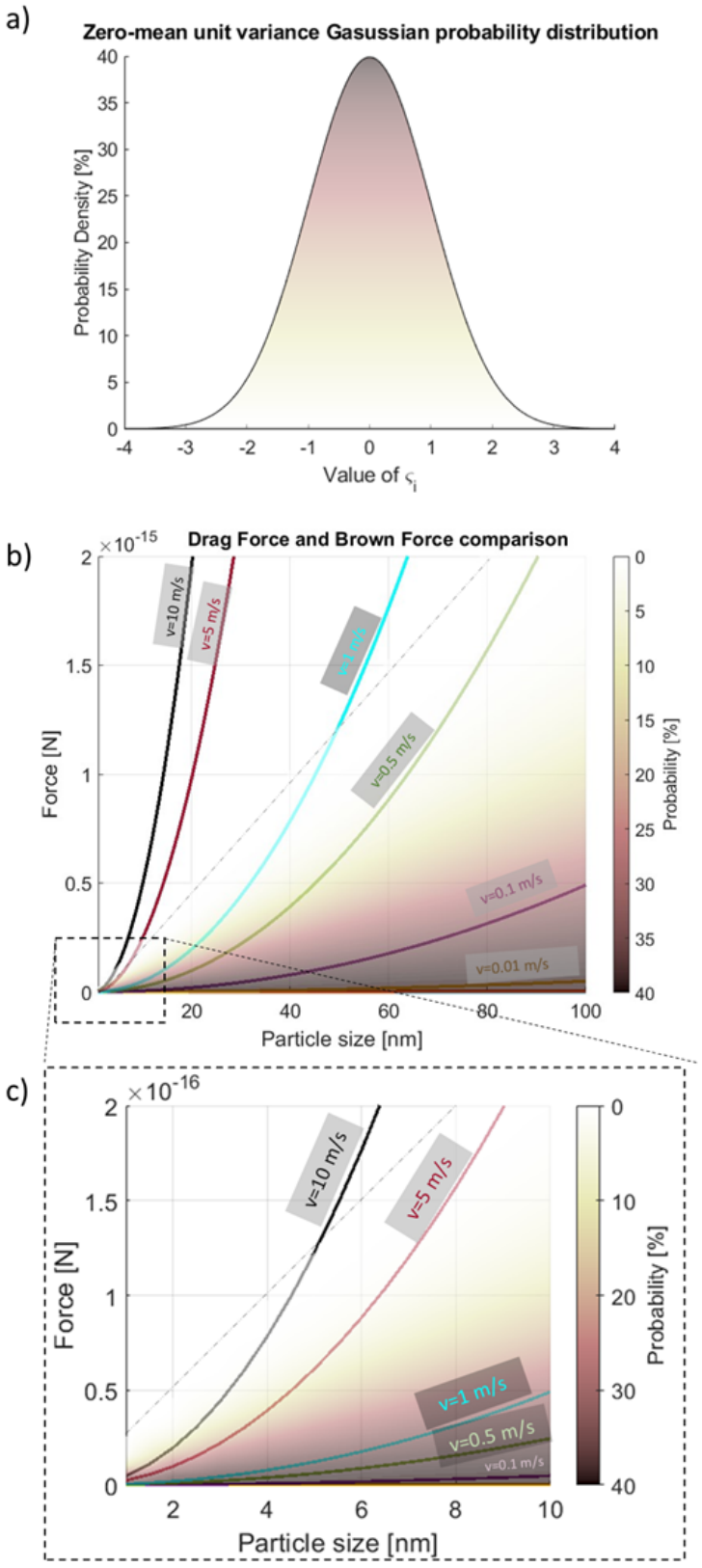

Figure 50. Comparison of the Brown force vs the drag force (Ar gas, the chamber pressure is 50 Pa, Tf is 293.15 K): a) Zero-mean unit variance Gaussian probability distribution (colourmap indicates probability); b) drag and Brownian forces acting on a Cu NP. Directions are neglected, and only scalar values are accounted for. For Brownian force, $\Delta t = 10^{-4}$ s was taken; c) close view of b). The dotted line shows the Brownian force with $\zeta_i = 3.0$ with a probability of 0.5% and is the edge of the colourmap. From ref. [99]

If we refer back to the results from the experiment shown in Figure 46 and Figure 47, we can see that the deposition rate of NPs is increased with an increased inlet flow rate. However, predominantly due to the increased number of NPs with diameters of 8-15 nm. Looking at Figure 48, we see that at the trapping region (according to CFD), the gas velocity is about 0.4 m/s. From Figure 50, we see that for NPs, e.g., of 10 nm, the probability of the Brownian force being the same magnitude as the drag force is relatively high and can be even bigger but less probable. Drag force points in the same direction as the gas flow, predominantly toward the orifice. At the same time, the Brownian force can point in any direction, which could knock the particle from its original position. Therefore, we can suggest that some deposited NPs were initially trapped but escaped the trapped region due to random Brownian motion.

For illustration, Figure 51 demonstrates the impact of the Brownian diffusion on NPs motion (Ø10nm) in the GAS with rear inlet configuration.

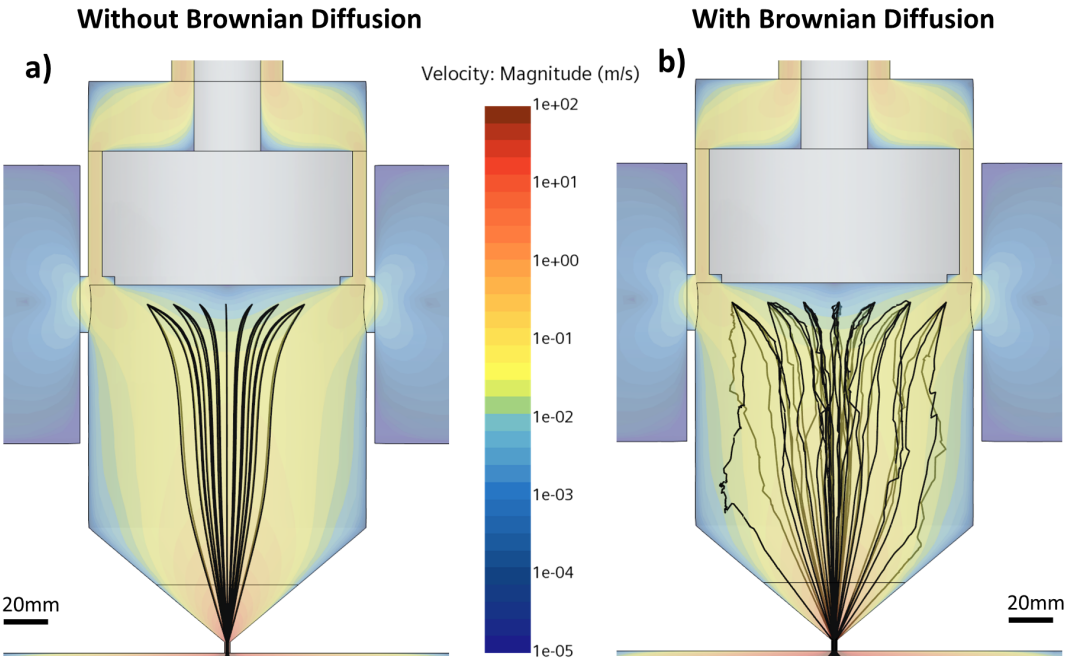

Figure 51. NPs track in planar magnetron GAS with rear inlet configuration. a) Ø10 nm Ag particles with drag force only b) Ø10 nm Ag particles with drag and Brownian force. Flow is siumulated for 18 sccm inlet flow rate, 133 Pa chamber pressure, and Tf is 293 K

4.4. Modelling of conditions for in-flight coating of NPs

As mentioned in Section 3.2.2., NPs leaving the GAS can be additionally modified by depositing a layer of secondary material in the auxiliary chamber. The geometrical dimensions of the two orifices should be chosen with extreme care to provide a higher

pressure in the GAS sufficient for the nucleation of primary NPs and a lower pressure in the auxiliary chamber to avoid the nucleation of the secondary material. At the same time, the pressure in the auxiliary chamber should not be too low to avoid an increase in NP velocity that might shorten the treatment time. CFD calculations (setup is described in Section 3.3.3.) were performed to analyse the gas flow in such a system. The experimental conditions were taken from the setup prototype that has been constructed in our laboratory, with a scheme shown in Figure 14. In this case, the auxiliary chamber was equipped with an additional pump outlet that could operate from the fully closed to the fully open state to regulate the pressure.

4.4.1. Auxiliary chamber with the support pump outlet

For the open support pump, the experimental conditions were as follows: the inlet flow rate of argon is 7 sccm; the pressure in the GAS is 40 Pa; the pressure in the mid chamber is 3.5 Pa; the pressure in the deposition chamber is 0.16 Pa; the orifice of the GAS is Ø4 mm and 20 mm in length, the orifice of the mid chamber is Ø7 mm and 25 mm in length. CFD simulation was done to accommodate these inputs. To precisely set 3.5 Pa for the mid-chamber, a boundary condition for the support pump outlet was set to be exactly this value. As the results of the CFD simulation shown in Figure 52, the pressure values match the experimental conditions.

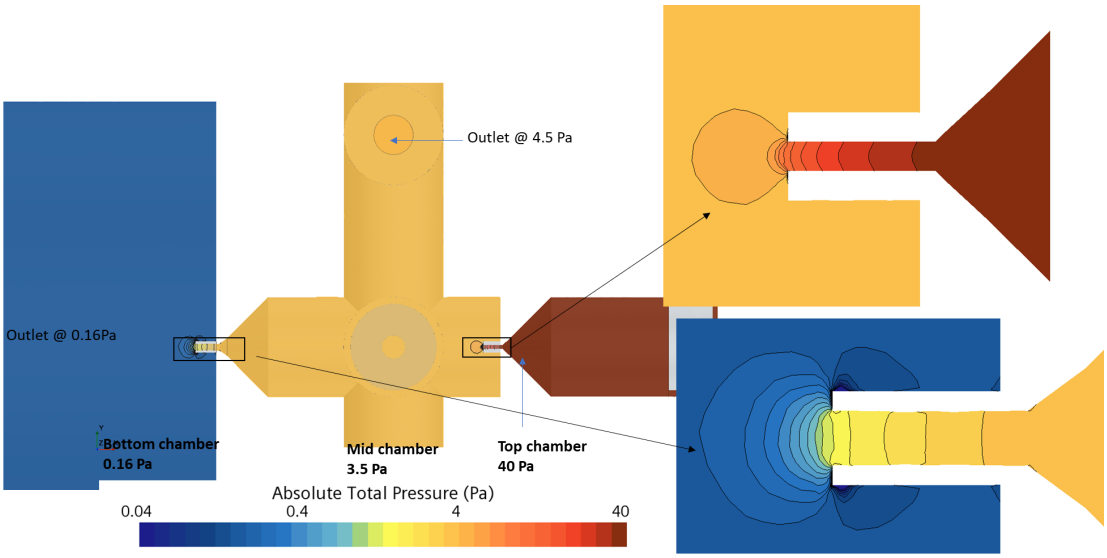

Figure 52. CFD simulation results for pressure for the GAS system for composite NPs fabrication. The inlet flow rate of Ar is 7 sccm. Outlet pressure boundary conditions are shown in the figure

NPs were inserted into the system to understand the impact of the support pump on the NP motion under the carrier gas flow. In the orifice region, a pressure drop is massive over the length of several millimetres, which leads to a substantial acceleration of the carrier gas flow as a result of the carrier gas expansion. Therefore, the Stokes drag approach with the Cunningham correction factor is no longer valid. In addition, it is reasonable to assume that Brownian diffusion does not significantly impact the NP transport. For simplicity, we also ignore the possible electrostatic trapping of NPs in the vicinity of the auxiliary magnetrons. Therefore, a different approach should be applied to solid particle forces. Here, we decided to accommodate the so-called aerodynamic lensing, which was already discussed at the end of Section 2.5.; thus, equation (34) should be used. The semi-transient approach was applied for the motion simulation of solid particles in the gas.

The results in Figure 53 indicate that the support pump in the mid-chamber has a significant influence on the carrier gas profile, hence on the NP trajectories. Due to the additional outlet, the neutral carrier gas tends to move toward the support outlet, which removes approximately 60% of the gas from the total flow toward the deposition chamber. As a consequence, smaller NPs (modelled as having Ø10 nm) lose their inertia gained from the gas expansion in the GAS orifice and then follow the carrier gas flow to the support pump outlet. Heavier NPs (modelled as having Ø50 nm) also lose inertia, but less drastically, allowing them to continue their path toward the deposition chamber. This finding may be important in the development of the mass separation of NPs, but, of course, this is not a desirable outcome if the entire set of NPs is needed to be collected in the deposition chamber.

A known downside of the GAS methodology is that part of NPs may become lost on the inner walls of the aggregation chamber. To investigate this effect, we introduced a sticking coefficient = 1 for NPs touching the wall (i.e., the NPs stick with 100% probability if they touch the wall). Only 50 nm NPs reach the deposition chamber, and we find that most of them stick to the walls in the vicinity of the second orifice. This correlates with the actual observations that deposits visible by the naked eye accumulate on the walls near the orifice. Sticking is also related to the higher inertia of heavier NPs because they do not perfectly follow the carrier gas flow.

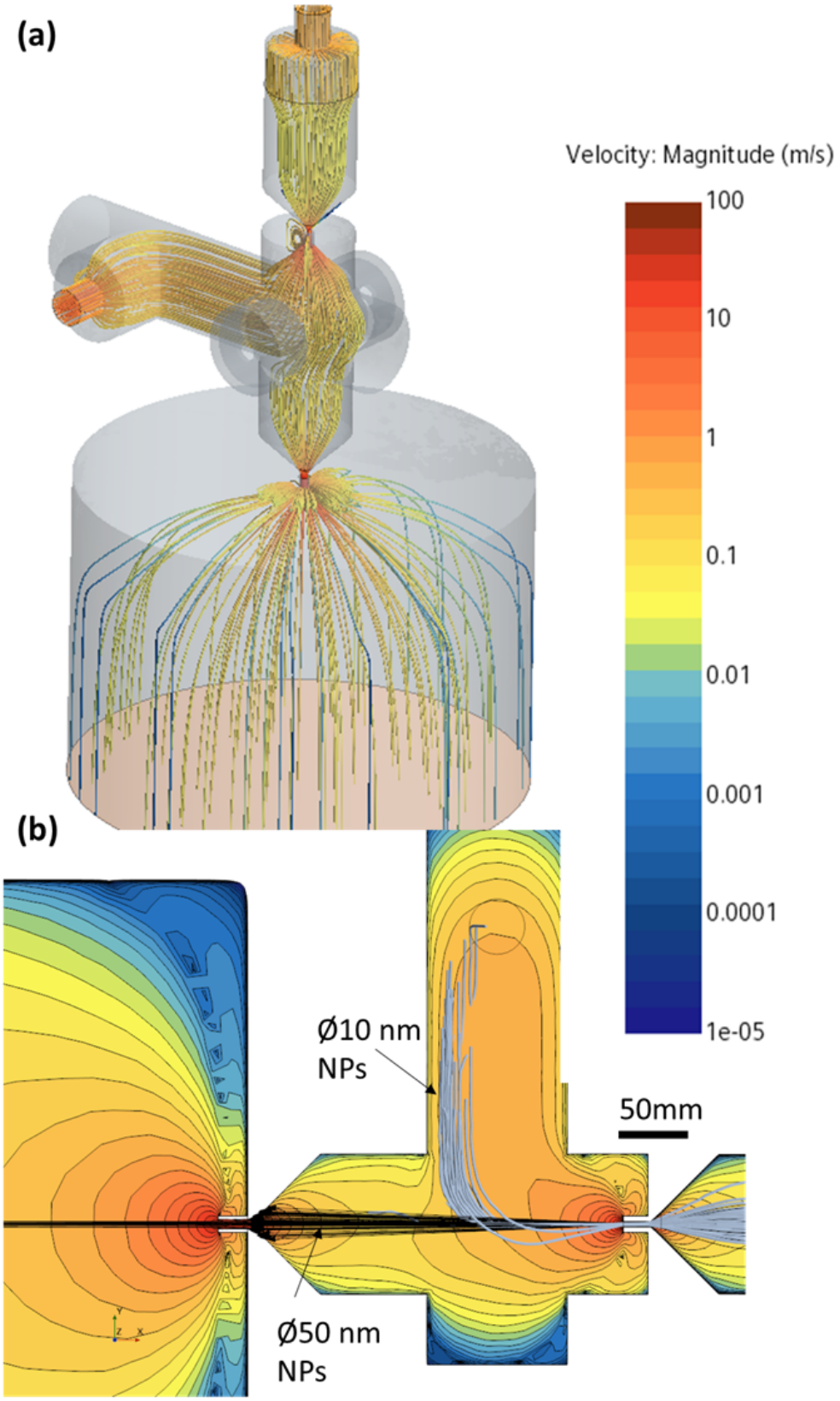

Figure 53. CFD simulation results for carrier gas velocity. (a) Velocity streamlines. (b) Section view of the velocity profile with solid particle trajectories. The grey track line corresponds to 10nm (with Brownian motion), and the Black track line corresponds to 50nm (without Brownian). The simulation was done for the system with the support pump at mid chamber set at 3.5 Pa, and the exit orifice is Ø7 mm and 25 mm in length. The top pressure chamber is 40 Pa, deposition chamber is 0.16 Pa. Inlet flow rate is 7 sccm of Ar gas

4.4.2. Auxiliary chamber without the support pump outlet

It was experimentally found that closing the valve for the support pump valve leads to an increase of the pressure in the mid chamber to 8.6 Pa, with all other experimental parameters remaining the same. As for the CFD simulation, we can either force the pressure in the mid-chamber to be 8.6 Pa by user input or let CFD determine the pressure by solving governing equations. Our goal is to optimise the system; therefore, we allow the CFD software to calculate the pressure values. After optimising the CFD model to be mesh insensitive, we obtain a pressure of 12.4 Pa. We accept this value as reasonably consistent with the experiment, considering that the calculations are made on the verge between a continuum medium and the transition regime (see the Knudsen number graph for the argon gas in Figure 9). The CFD pressure values are shown in Figure 54a, whereas Figure 54b and c show the section of the carrier gas velocity and velocity streamlines, respectively. The carrier gas flows predominantly toward the deposition chamber, creating less intensive vortices at the side ports. Therefore, even smaller NPs have a higher chance of not being captured by a bypass gas flow.

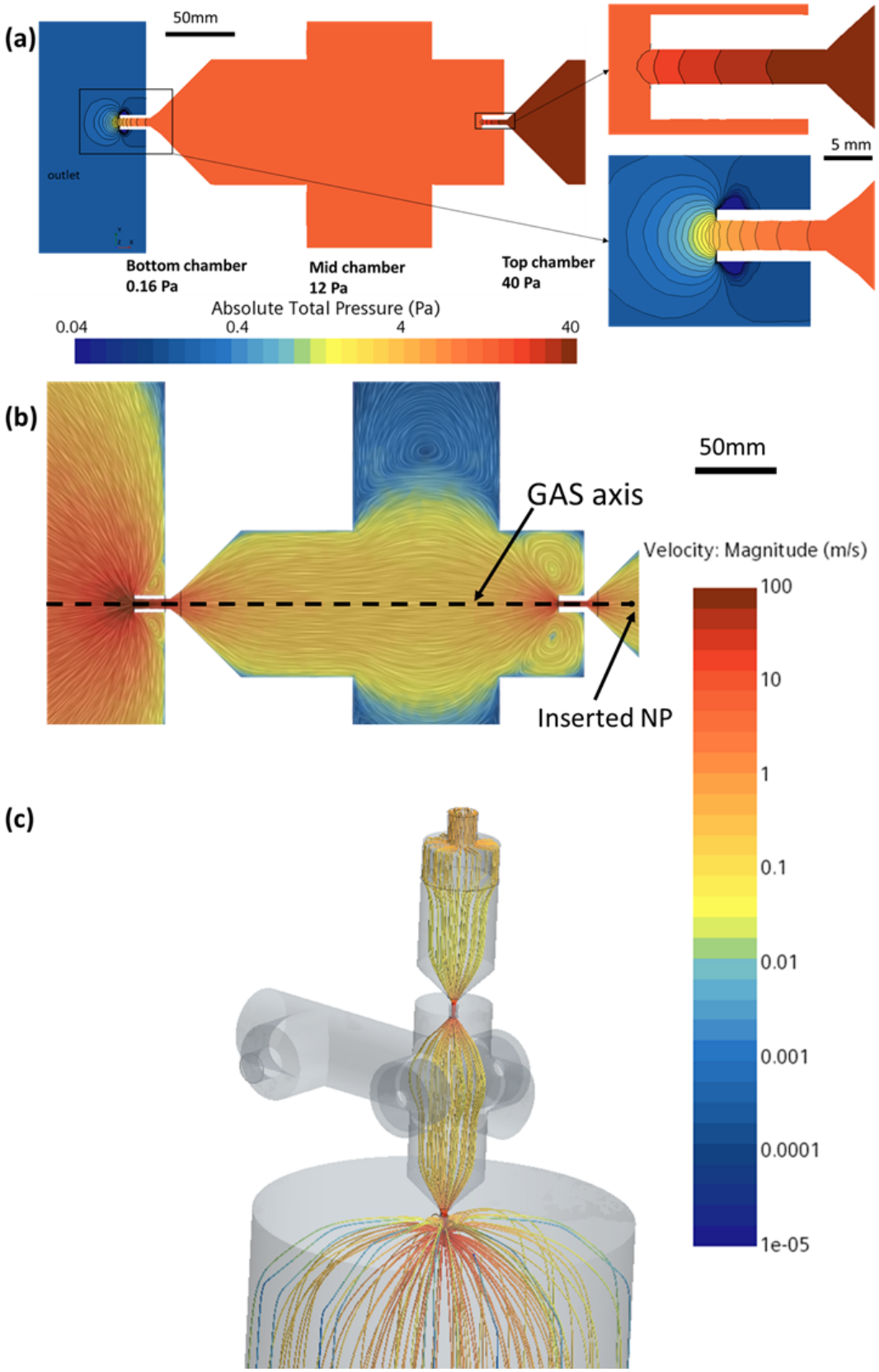

Figure 54. CFD simulation results for the GAS system for composite NPs fabrication without support pump at mid chamber. (a) Pressure scene; (b) Velocity convolute scene; (c) Velocity streamlines.

4.4.3. Orifice impact on NPs' in-flight modification

We note that the pressure of 8 - 12 Pa may not be optimal for the sputtering of secondary material because typical magnetron sputtering is conducted at lower pressures. One of the ways to reduce the pressure in the mid-chamber is to increase the diameter of the second orifice. We used CFD modelling to calculate the pressure in the mid-chamber for larger diameters of the second orifice of 11 and 15 mm. Indeed, the pressure decreases to 4.4 and 2.5 Pa, respectively, which are the values more consistent with conventional sputtering. However, one should bear in mind that a decrease in pressure is inevitably accompanied by an increase in gas velocity, which shortens the time that NPs spend in the treatment zone. To estimate the residence time of NPs, we put the NP precisely on the axis in the vicinity of the GAS orifice (which is schematically shown in Figure 54b) and performed six different simulations for three orifice diameters of Ø7, Ø11, and Ø15 mm, and two NP sizes of 10 nm and 50 nm. The results are summarized in Figure 55.

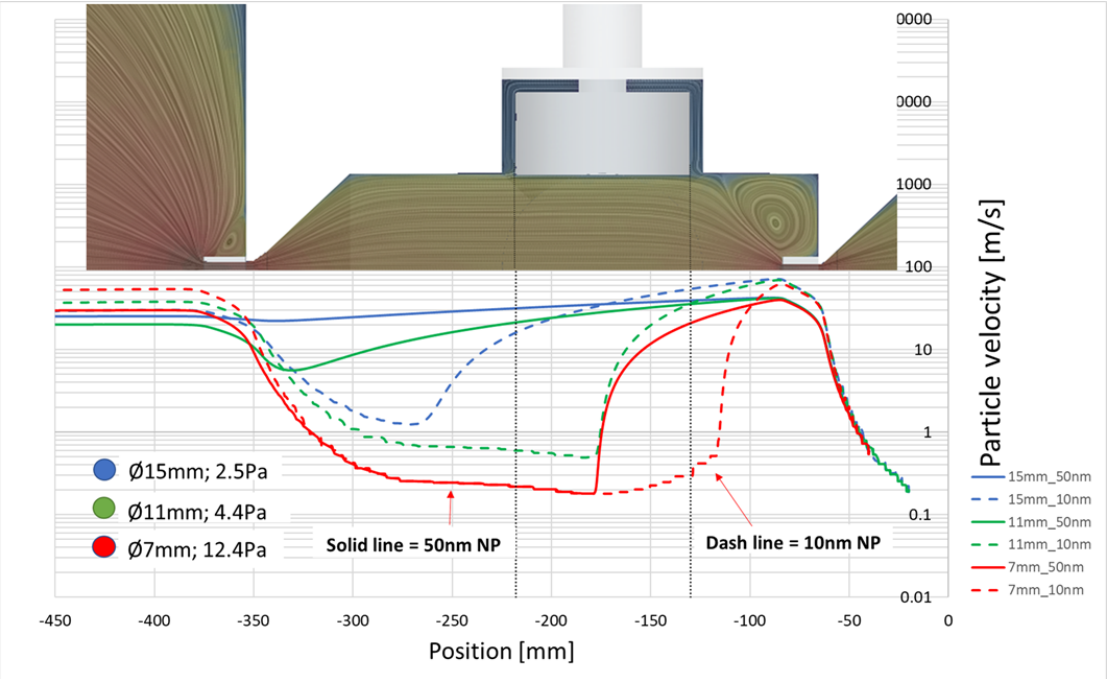

Figure 55. Comparison of NPs velocity for different orifices. Red colour corresponds to Ø7mm orifice@12.4 Pa; Green colour corresponds to Ø11mm orifice@4.4 Pa; Blue colour corresponds to Ø15mm orifice@2.5 Pa. Solid line corresponds to Ø50nm NP and dashed line for Ø10nm particle. Velocity scene is for Ø7mm orifice case, here for geometrical reference. All results are from CFD simulation.

According to simulations, 10 nm NPs gain twice as much velocity as 50 nm NPs, when passing through the GAS orifice; therefore, small NPs enter the GAS at a higher speed. However, they also lose the gained velocity faster. Suppose we simplify the model by assuming that the treatment zone is limited by the dimensions of the auxiliary magnetron (illustrated by the dotted vertical lines in Figure 58). In that case, the residence time of NPs in this zone can be calculated by performing numerical integration of the velocity over the given distance. The results of such calculations are shown in Table 5.

Table 5. Particle residence time in the assumed capture zone calculated from the CFD. The colours correspond to the ones used in Figure 55.

Particle residence time		
	NP: Ø10nm	NP: Ø50nm
Orifice Ø7mm (@12.4 Pa)	0.428 s	0.219 s
Orifice Ø11mm (@4.4 Pa)	0.084 s	0.0032 s
Orifice Ø15mm (@2.5 Pa)	0.0028 s	0.0024 s

It follows from Table 5 that the residence time of NPs decreases drastically with the decrease in pressure for larger orifices. Simple estimations give that the deposition of a 1 nm thick secondary coating over a 10 nm NP with the 7 mm orifice requires a deposition rate of about 2 nm/s, which imposes demanding yet reachable requirements on the operation of the auxiliary magnetron. However, for the largest orifice of 15 mm, the deposition rate would have to be about 400 nm/s, which goes far beyond the realistic value. Therefore, our calculations highlight the crucial importance of choosing the proper experimental design and geometry to achieve the goal of in-flight coating of NPs with secondary material.

It can be mentioned that other parameters may also influence the residence time. For instance, increasing the pressure in the GAS and keeping the pressure in the mid-chamber constant will increase the peak NP velocity after the GAS orifice and, hence, decrease the residence time. On the other hand, if one manages to reduce a pressure drop between the GAS and the mid-chamber, the residence time can be increased as NPs travel slower over the region of interest. Therefore, CFD proves to be a very useful tool that helps to optimise the system according to one's needs and decreases cost and time by performing fewer try-and-error steps.

4.5. Post-Cylindrical Magnetron GAS

Despite the popularity of the GAS in the scientific community, there are known issues in the GAS with planar magnetron that prevent its wide implementation in the industry. Trapping of NPs, which was discussed before, the uncertainties and lack of understanding of detailed physical processes, inefficient target material utilisation, high working gas consumption, low efficiency of the nucleation/growth of NPs, NP loss because of uncontrollable re-deposition on the target surface and escape to the walls, etc. [138], [139].

An attempt to resolve the issue of inefficient utilisation of the target and the long-term stability of the NPs formation in the planar magnetron was made by Huttel et al. [140]. They added a rotating magnetic circuit to the conventional planar magnetron.

4.5.1. Pre-development of the post-cylindrical magnetron GAS

Our group attempted to build a GAS with a post-cylindrical magnetron with a rotating magnetic circuit. For that, CFD was utilised as a pre-production optimisation tool, which helped to get "reference points" to understand the design performance. First, a prolonged cylindrical shape was designed and subsequently analysed in CFD. The baseline design of the chamber with prolonged cylindrical magnetron (post magnetron) is shown in Figure 56.

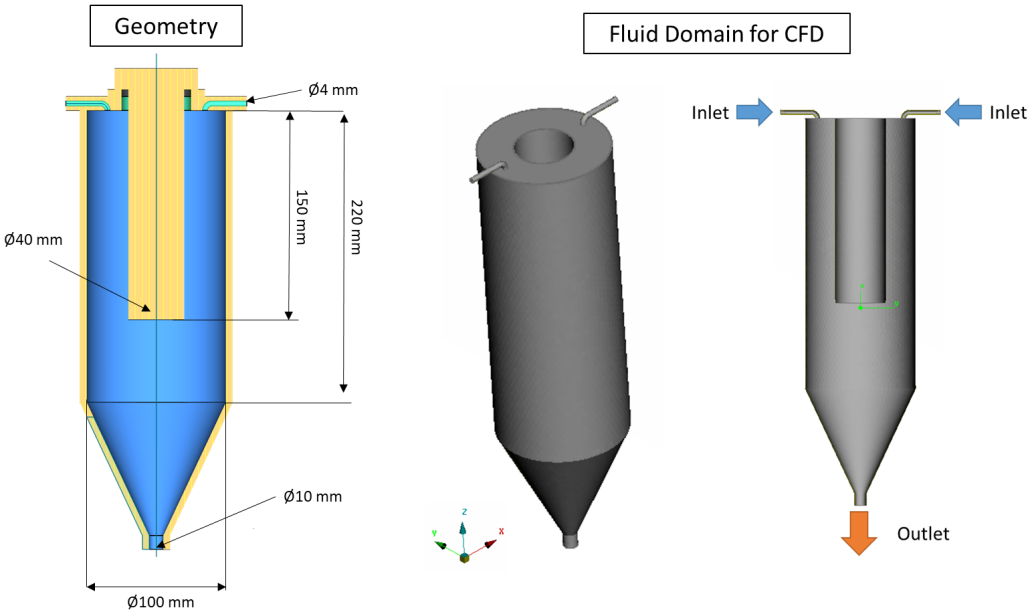

Figure 56. The baseline design for the post-cylindrical magnetron. The geometry and Fluid Domain required for CFD are shown

For the baseline design, a CFD simulation was provided under the following conditions: argon gas as a working gas; inlet flow rate 10 sccm (total, i.e., each 5 sccm); chamber pressure was assumed to be 100 Pa, outlet pressure was set to 1 Pa, fluid temperature is 293.15 K, as well as all walls temperature (including magnetron). The results of this simulation are shown in Figure 57.

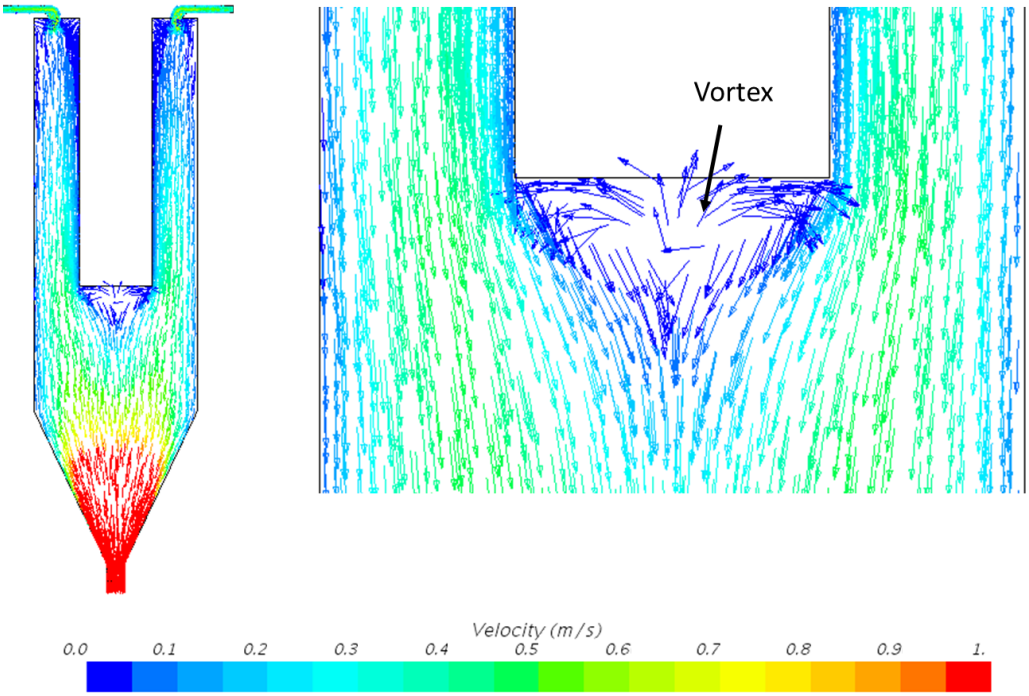

Figure 57. Results of the CFD simulation of the Baseline design of the post magnetron GAS. 10 sccm inlet flow rate, 100 Pa pressure, 293.15 K temperature of fluid and walls. Velocity vectors are shown.

Under assumed conditions, a vortex just beneath the magnetron is noticed. To eliminate the vortex, it was decided to add a geometric feature that could help to direct the flow so that the vortex would disappear. A conical body with a rounded tip is the best geometrical design to fulfil that purpose. The updated design, including a conical body at the end of the magnetron, is shown in Figure 58. CFD simulation results for the updated design (done under the same conditions as the baseline design) are shown in Figure 59.

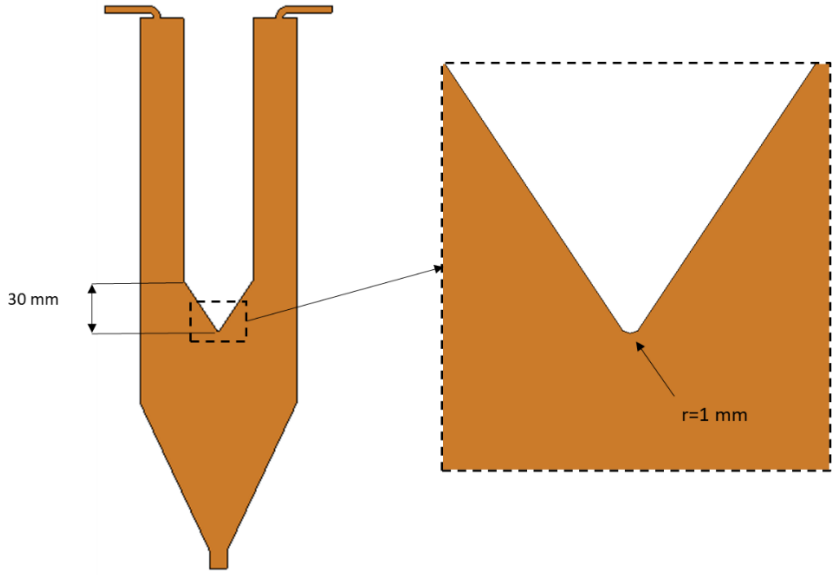

Figure 58. The updated baseline design of the post magnetron GAS introduced a conical tip for the magnetron.

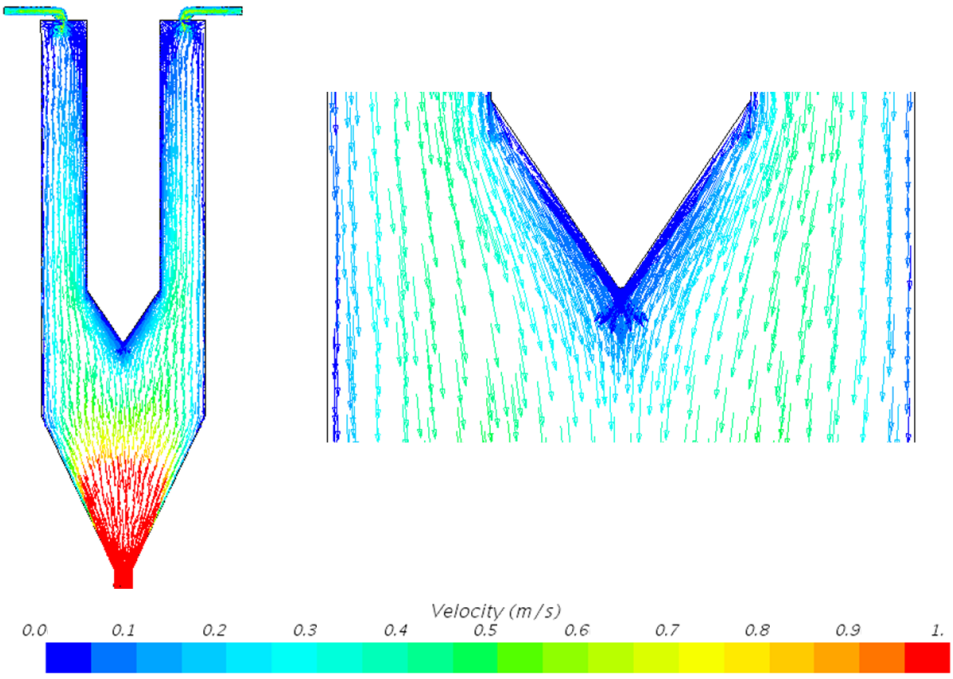

Figure 59. CFD results for the GAS with post magnetron that has a conical tip. Velocity vectors are shown.

Implementation of the conical tip to the post magnetron eliminated the presence of the vortex beneath the magnetron. After the approval of the concept, a production phase was initiated.

Due to technicalities, the final experimental build had some differences compared to the concept design, with the main one being an inlet channel on only one side of the magnetron instead of two inlets, as shown in Figure 56. The experimental build is

shown in the Experimental section of this work in Figure 15. Prior to the experiments, an additional CFD analysis was provided for the new geometry. For that case, the inlet flow rate was 20 sccm, pressure in the chamber was 117 Pa, and orifice diameter and length were Ø2 mm and 1 mm, respectively. The outlet pressure was set to be 0.2 Pa. CFD simulation results under given conditions are shown in Figure 60. There we can observe that the asymmetrical inlet (only on one side) at a 20 sccm inlet flow rate brings small vortices just at the entrance of the chamber. However, the position of these vortices is of no concern for experimental purposes. Overall the flow performance was estimated as satisfactory, and the experiment proceeded.

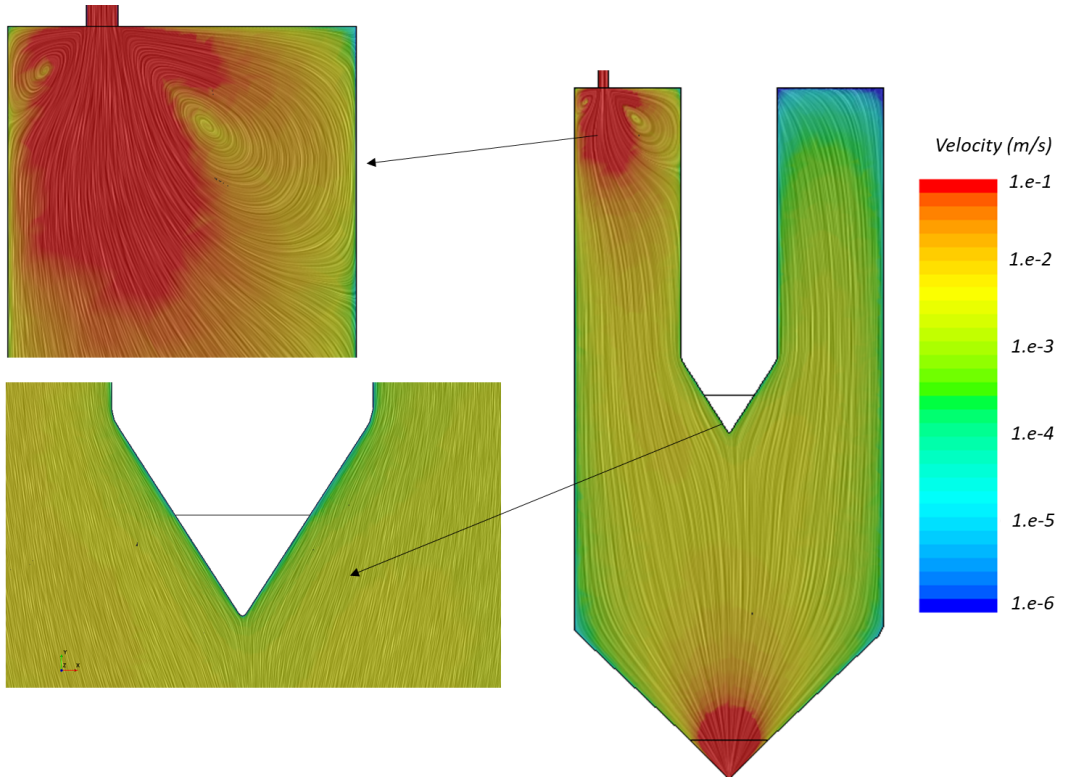

Figure 60. CFD simulation results for the experimental GAS build with post-cylindrical magnetron with conical tip. Inlet flow rate: 20 sccm; Chamber pressure: 117 Pa; Outlet pressure: 0.2 Pa, Temperature of the fluid and walls is 293.15 K. Velocity vector convolute results is shown.

4.5.2. Experiment results for post-cylindrical magnetron GAS

Experiments were provided under conditions reported in Section 3.2.3.. Two Ar inlet flow rates were tested under the same pressure of 160 Pa, which was achieved by using two different exit orifices. The magnetic circuit was rotating with the stepwise increase of speed and under a constant DC power supply. Photographs of the discharge at two different times are shown in Figure 61.

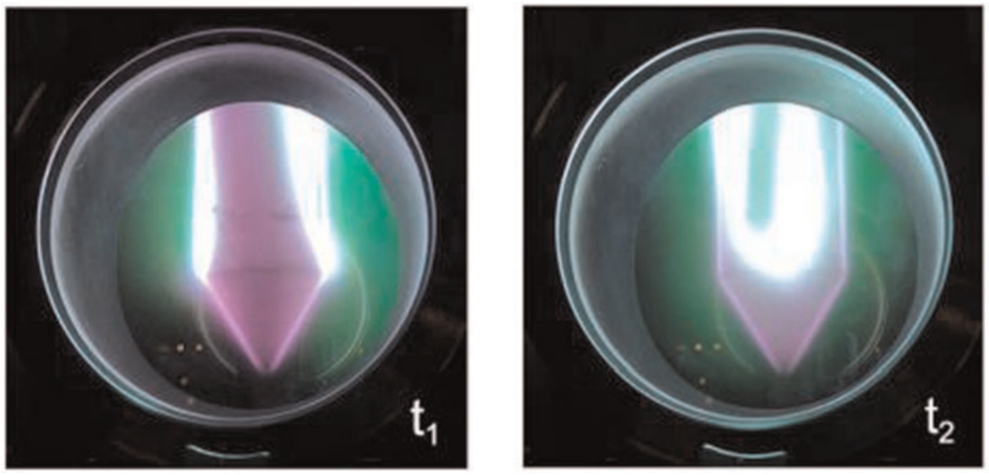

Figure 61. Photographs of discharge at two different time snaps, t1 and t2, during the rotation. From ref. [96]

QCM monitored the time-resolved instantaneous values of the deposition rate; its results are shown in Figure 62a and Figure 62b. Measurements show significant fluctuations in the instant deposition rate, with vigorous instabilities at lower rotation speeds and stabilisation at a higher rotation speed. This suggests a presence of a destabilizing factor that may impair the GAS performance at a low rotation speed. Similar fluctuations were reported for planar magnetron-sputtered Cu and Ag NPs as well in [73], [74], [98]. Fluctuations in deposition rate are possibly caused by the cycling trapping and release of NPs from the trapping zone in the region circumscribed by the plasma torus. The complex balance of forces acting on NPs constrains charged NPs to stay longer in the trapping region, grow to a larger size, acquire a larger charge, and be exerted by the electrostatic interactions after reaching a critical size. If we apply the same logic to the post-cylindrical magnetron case, then the trapping region is also presented in the vicinity of ellipsoidal plasma tunnels in proximity to the target/magnetron surface. At lower rotations of the magnetic circuit, the NP clouds follow the rotating trapping region and are expelled in cycling bursts after reaching the critical size.

Furthermore, post-cylindrical magnetron GAS, similar to planar magnetron GAS, also shows an abrupt burst of the deposition rate after switching off the discharge (at time 300s in Figure 62a). Indicating the trapped NPs are released from the trap due to a lack of the electromagnetic forces provided by the plasma environment. Released NPs are then dragged by the carrier gas toward the orifice and subsequently to the QCM. The time-lapse between the discharge extinction and the QCM burst perfectly correlates with the carrier gas velocity taken from the CFD simulation (Figure 65).

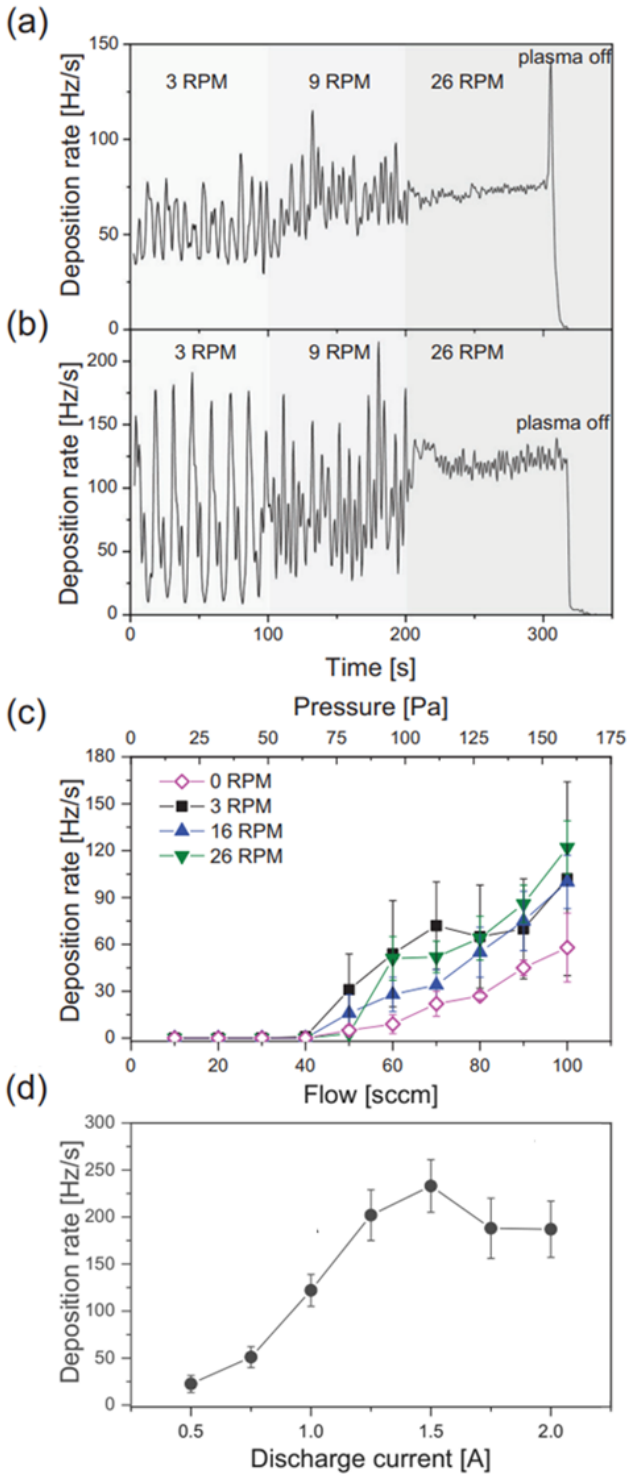

Figure 62. The Cu nanoparticle deposition rate: time evolution in dependence on the magnetic circuit rotation speed at DC 1 A and pressure 160 Pa for different flows: (a) 40 SCCM, orifice 2.5mm; (b) 100 SCCM, orifice 3.5mm; (c) averaged values in dependence on Ar flow and different pressure (fixed orifice of Ø3.5mm, DC 1 A); (d) in dependence on DC (26 RPM, 100 SCCM, orifice 3.5mm). Adapted from [96]

However, as shown in Figure 62b, no such burst is observed for a 100 sccm inlet flow rate. In that case, high Ar flow may disturb the trapping effects in plasma, providing a more effective release of NPs from the GAS. In general, if we look at Figure 62c, the

inlet flow rate is a crucial parameter that affects the GAS performance (in terms of deposition rate). Under low flows (<40 sccm), no deposition is detected by QCM for any magnetic circuit rotation speed. Gradually increasing the inlet flow rate helped us indicate that the flow rate >40sccm, the carrier gas is able to transport part of the NPs from the aggregation zone to the deposition chamber. The number of NPs extracted from the aggregation chamber increases with the flow rate, maximizing at 100 SCCM, due to technical limitations (pumping system). It is important to note that the inlet flow rate was changing while the diameter of the orifice remained fixed. Hence, the aggregation chamber pressure also increases with an increased inlet flow rate. In earlier studies done by our group ([141], [142]), it was shown that for planar magnetron GAS, NPs fabrication from Cu target was possible with the being pressure as low as 20 Pa. This suggests us that in the case of post-cylindrical magnetron GAS, the flow inside the GAS is insufficient to overcome other forces acting on particles and escape the trapping region. Presumably, an increase of the inlet gas flow rate above 100 SCCM may enhance the efficiency of the post-cylindrical GAS, but only under necessary conditions that pressure will be sufficiently small for a collisionless sheath.

The plasma region and electron trap (due to the effect of an ExB) in the post-cylindrical magnetron case have bigger geometrical dimensions. This presumably creates a bigger NPs trapping region, which does not allow even small NPs (< Ø30nm) to escape the trap by Brownian diffusion. Thus, a bigger drag force (higher flow rates) could be required even of the optimized systems to extract NPs from the source.

On the other hand, the rotation speed of the magnetic circuit does not provide such an increase in performance of the GAS as the inlet flow rate, as shown in Figure 62c. The deposition rate for the static magnetic circuit is lower than for any rotation cases. Results shown in Figure 62c indicate that increasing a magnetic circuit's rotational speed increases the deposition rate of NPs.

Figure 62d shows the dependence of the deposition rate on the discharge current, the magnetic circuit rotation speed of 26 rpm and the inlet flow rate of 100 sccm (the most effective combination in terms of deposition rate). At a low discharge current range (up to 1.5 A), there is an almost linear dependence between current and

deposition rate, which relates to the intensification of sputtering. However, after a threshold discharge current value and higher, the deposition rate saturates (possibly the deposition rate would go lower for even higher current). It could be due to the enhanced thermal load to the gas phase that shifts the nucleation conditions unfavourably.

If we compare deposition rates of GAS with post-cylindrical magnetron for Cu NPs (Figure 62d) against planar magnetron GAS (also with Cu target) from the [141], [142], we can see that the post-cylindrical magnetron (for 100 sccm and 26 rpm) provides several times higher deposition rates. Thus, the post-cylindrical magnetron GAS, even in its non-optimized configuration, provides the deposition rate reaching toward the upper range of the sputter-based NP synthesis. The proper optimization of the geometrical design and the experimental conditions are expected to lead to a system foreseeably competitive with higher-yield technologies.

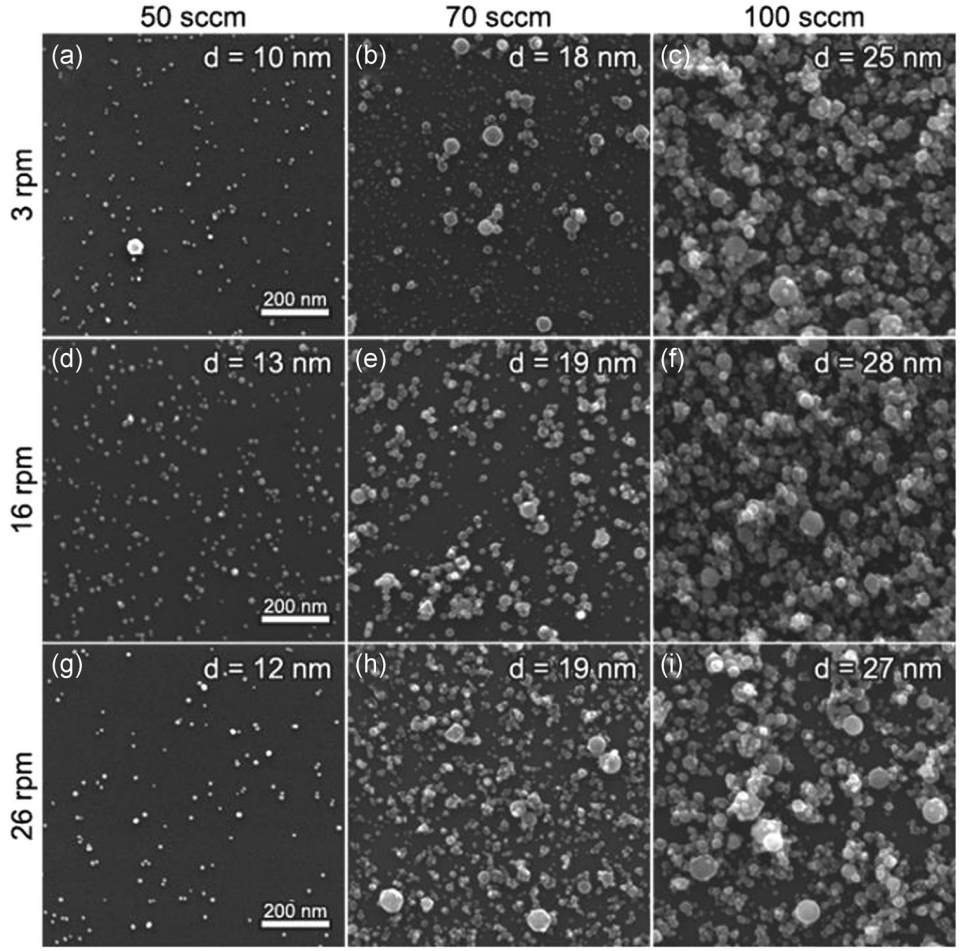

Figure 63. Scanning electron micrographs of Cu nanoparticles (NPs) deposited on Si substrates at different magnetic circuit rotation speeds and Ar inlet flow rates. The deposition time is 40 s, and d is the NP mean diameter. Corresponding pressure values can be found in Figure 62c. From ref. [96].

The impact of the inlet flow rate (of argon) and the magnetic circuit rotation speed on the NPs size were also studied. The SEM images of the deposited Cu NPs under various parameters of inlet flow rate and rotation speed of a magnetic circuit are shown in Figure 63. The size distributions were readily fitted by a log-normal function, and size histograms are shown in Figure 64. The mean NP diameter increases, and the size distribution broadens with the inlet flow rate for all RPMs tested. On the other hand, no dependence on RPM for a given inlet flow rate can be perceived. Figure 63 also demonstrates that the number of NPs increases with the inlet flow rate. In comparison, the increase of RPM of the magnetic circuit led to an increase in the number of NPs at a much lower rate than for the inlet flow rate change. The size distribution histograms shown in Figure 64 indicate that the larger size tail of the distribution is more populated for the slow rotation speed, though not significantly affecting the mean diameter of NPs.

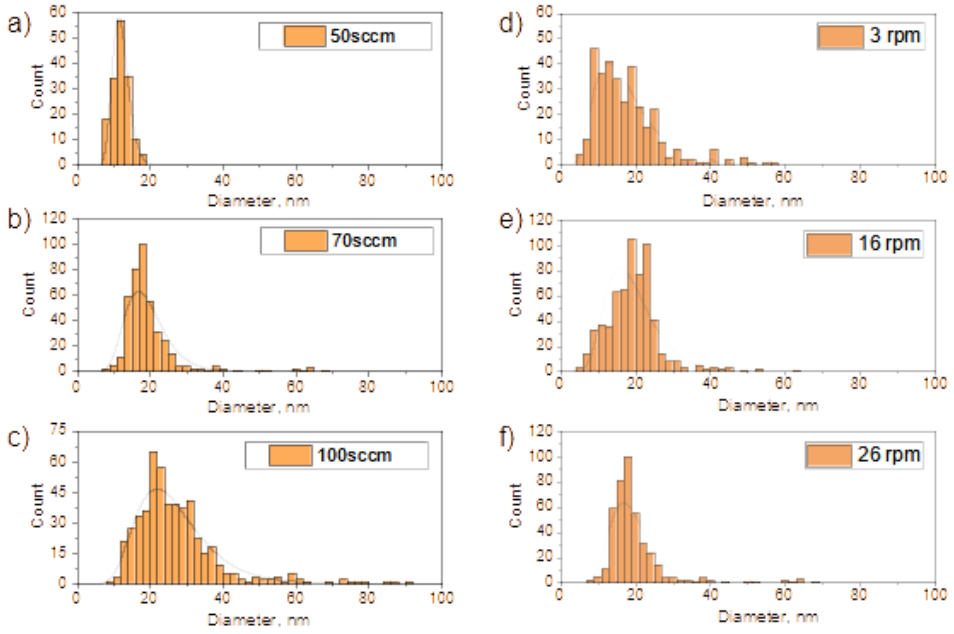

Figure 64. Size distributions of Cu NPs prepared at: (a-c) different Ar flow (DC = 1 A, speed of magnetic circuit rotation = 26 RPM); (d-f) different speed of magnetic circuit rotation (DC = 1 A, Ar flow = 70 sccm)

No erosion tracks were observed on the target by the visual inspection, even after several weeks of experiments. However, detailed measurements of the magnetron diameter revealed an overall decrease in the diameter of 0.3 mm along the whole axial length. This proves that the GAS with cylindrical post magnetron provides much better target utilisation than the GAS with the planar magnetron configuration.

4.5.3. CFD analysis of post-cylindrical magnetron GAS

To further explore the peculiarities observed in the NP deposition rate and size distribution, let's look at the CFD simulation results (model setup was discussed in Section 3.3.4.) for 40 sccm and 100 sccm inlet flow rates at constant pressure 160 Pa (Ø2.5 mm and Ø3.5 mm orifice diameter, respectively), shown on Figure 65. The crucial difference is emphasized by arrows, showing an averaged direction of the argon carrier gas flow.

For the 40 SCCM, the flow pattern is symmetric with respect to the magnetron axis and oriented downward, toward the exit orifice, on both sides of the magnetron, with the gas speed in the range of several cm/s and without significant vortices. For 40 sccm, an abrupt increase in the deposition rate after switching off the discharge was detected (see Figure 62a) associated with trapped NPs. Moreover, the sample placed on the inner wall within the GAS opposite to the discharge showed a substantial number of NPs (Figure 66a) at 40 sccm. This means that at lower inlet flow rates, hence carrier gas velocities, there is no sufficient drag force to extract the NPs from the trap and push it to the deposition chamber via a carrier gas. The NPs clouds are expected to be formed in the trapping zones close to the magnetron, undergoing periodic expelling by the electrostatic forces and acquired kinetic energy allows NPs to overcome the gas drag force and reach the walls.

In the case of an inlet flow rate of 100 SCCM, the gas flow inside the aggregation chamber is more perturbated, showing higher diversity in velocity vectors and introducing a giant vortex just beneath the conical tip of the post magnetron that extends its influence over all axial length of the magnetron. At 100 sccm inlet flow rates, carrier gas velocity values are, in general, an order higher than for the 40 sccm case. For the cross-section shown in Figure 65, the gas flow changes direction from downward at the left of the magnetron to an upward direction at its right, demonstrating an instance of an even more complex gas flow pattern in the entire volume of the GAS. No deposits were observed on the samples within the GAS (Figure 66b), whereas QCM detected a high deposition rate. Hence, the drag force from the higher gas flow prevents the NPs from reaching the walls, with the gas carrying them to the deposition chamber. In addition, an orientation of the carrier gas velocity could play a part in better NPs extraction performance.

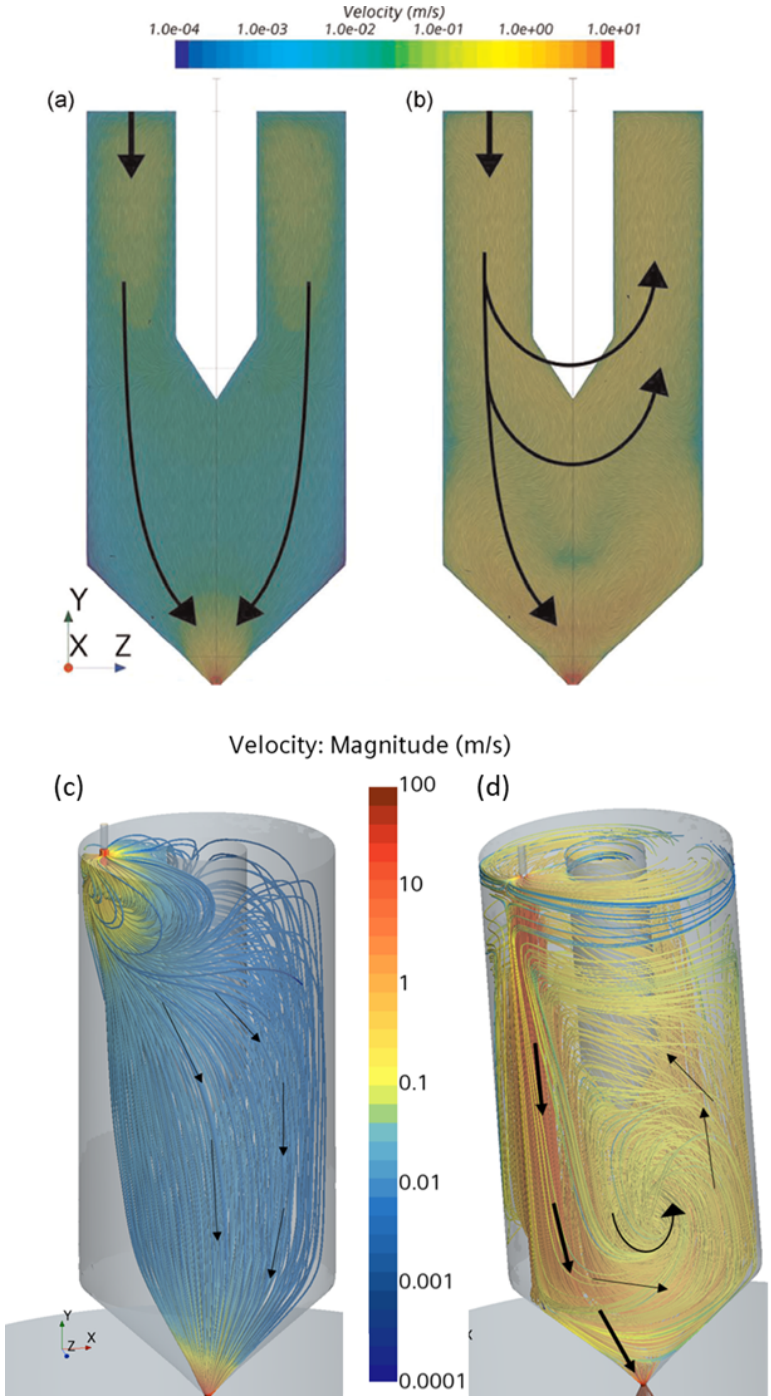

Figure 65. Models of the gas flow at constant pressure 160 Pa in the GAS: (a) Velocity vector convolute for 40 sccm, orifice 2.5 mm; (b) Velocity vector convolute for 100 sccm, orifice 3.5mm; (c) Velocity streamlines for the 40 sccm; (d) Velocity streamlines for 100 sccm. From ref. [96]

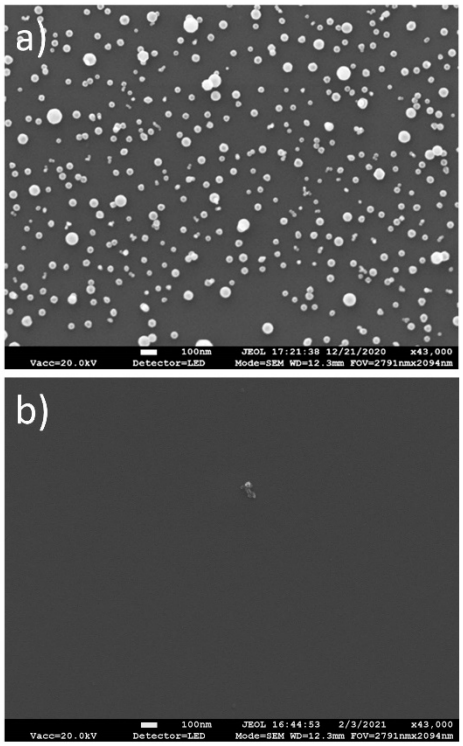

Figure 66. SEM images of samples placed on the wall of the aggregation chamber opposite to the discharge: a) inlet flow rate: 40 SCCM; b) inlet flow rate: 100 SCCM. For both, Pressure = 160 Pa, DC = 1 A, speed of the magnetic circuit rotation = 9 RPM, deposition time = 30s.

4.5.4. Optimisation of the carrier gas flow via CFD

The presence of the vortex beneath the magnetron cone is associated with very high inlet flow rates. During the design and production phases, high inlet flow rates were not accounted for in the simulations. The inlet configuration can be optimised using a CFD to make the carrier gas flow more 'symmetrical' and eliminate vortices in critical areas. The presence of an essential vortex was observed at 100 sccm inlet flow rate. Therefore, the optimisation was done assuming this flow rate. Cu NPs of Ø30 nm and Ø5 nm were added to the model using the semi-transient approach described in Section 2.5.1.. Tens of optimisation iterations were done, which, thankfully to CFD, was not that expensive. However, only two final and best approaches will be shown in this work (Figure 67).

In the case of the original geometry with a single rear inlet (Figure 67a), the CFD detects a massive vortex with a rotation centre beneath the magnetron and a few boundary layer separation regions on the magnetron. Optimisation variant 1 involves two side inlets positioned symmetrically with respect to the GAS axis on the rear side (Figure 67b). This inlet configuration demonstrates better gas flow symmetry in the

bottom part of the cylindrical magnetron; however, vortices can be observed in the vicinity of the inlets, propagating towards the upper side of the magnetron. Optimisation variant 2 involves an Ar supply in the form of a ring channel with two opposite inlets (Figure 67c). Here, Ar enters the GAS through the entire ring's circumference and flows along the post-magnetron surface. A highly symmetric gas flow was achieved within the GAS interior, with no vortexes or wakes observed and no boundary layer separation. The gas velocity vectors propagate along the lateral magnetron surface and should facilitate the coaxial drag of NPs toward the exit orifice.

Nevertheless, the effect is achieved at the expense of a decrease in the local gas velocity magnitude that drops by an order of magnitude compared to the un-optimised configuration. A lower gas velocity may result in a lower drag, which may negatively impact the NP deposition rate. Figure 68 shows motion tracks simulated for 30nm and 5nm Cu NPs. Larger 30 nm NPs follow the gas flow stream but undergo disturbances due to the Brownian diffusion. Smaller 5nm NPs travel primarily under the Brownian diffusion, resulting in chaotic track lines, as expected. Some of the small NPs attach (black dots) to the walls of the magnetron and chamber (the probability of sticking was defined as 1, which means - no rebound is possible).

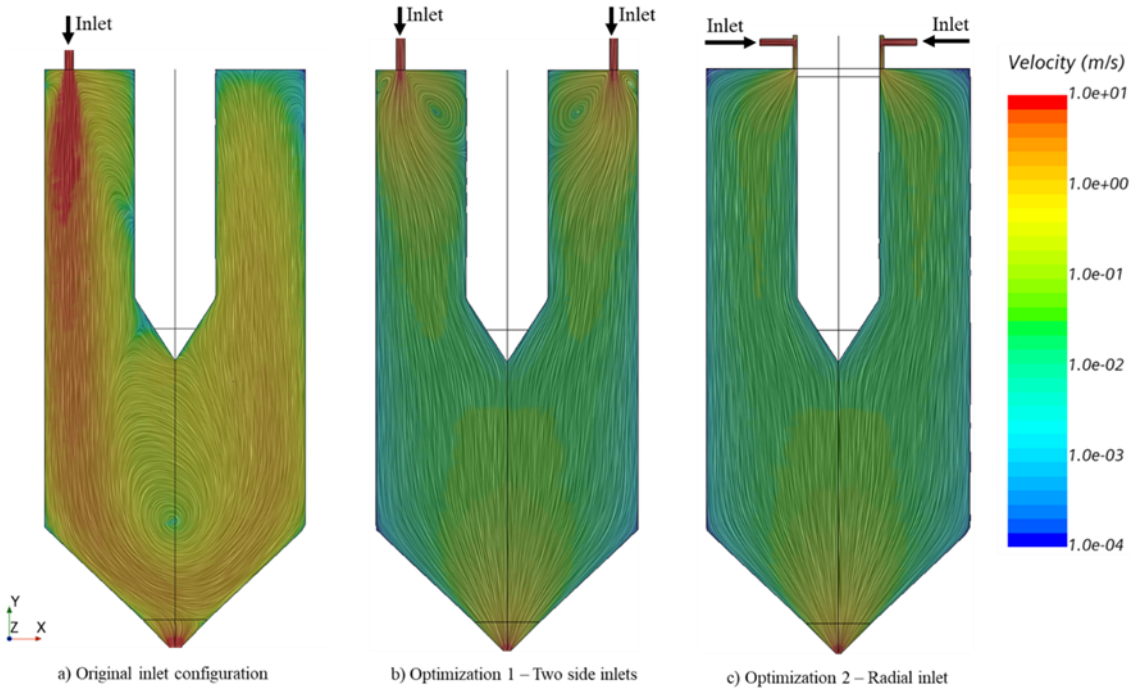

Figure 67. Ar flow simulations for the GAS with cylindrical post magnetron: a) original design with the asymmetrical placement of a single inlet, b) optimized variant I: - the two opposite inlets; c) optimized

variant II-Ar flows from the ring channel supplied from the two opposite inlets. Numbers show the velocity magnitude, with the vector plotted as convolute (integrated) lines. All simulations were done under the same conditions: inlet – 100 sccm, argon atmosphere, aggregation chamber pressure – 160 Pa, outlet pressure – 0.1 Pa, and the temperature of fluid and walls are set to 293.15 K. From ref. [99]

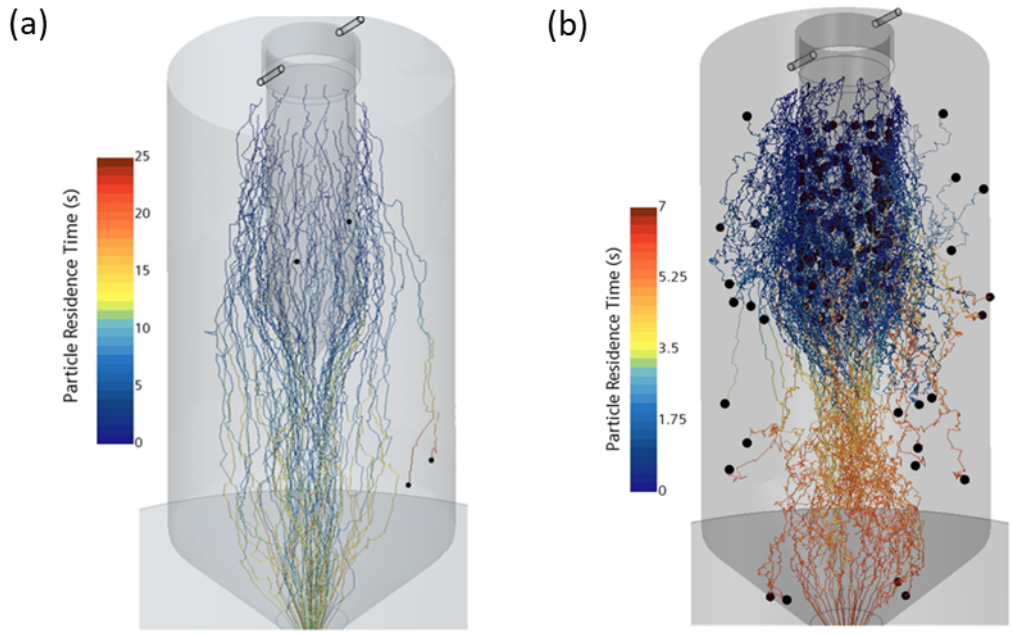

Figure 68. NPs track in the GAS with the post cylindrical magnetron: (a) 30 nm NPs; (b) 5 nm NPs. Both simulations were done under the same conditions: inlet Ar flow is 100 sccm, pressure in the GAS is 160 Pa, pressure behind the outlet is 0.1 Pa, and temperature of NPs is 293 K. From ref. [99]

It is important to remember that forces acting on NPs are of a very complex nature, and the simulations above only consider the isolated influence of specific forces, namely: aerodynamic drag, gravity, pressure gradient, and Brownian forces (all discussed in Section 2.5.). Electromagnetic forces, ion drag, thermophoretic forces, and others were not accounted for.

5. Conclusions

This PhD thesis can be concluded with the following points:

1. PLA, as a promising polymer material, can be used to create plasma polymer films. Deposition of thin films using magnetron sputtering of PLA has been demonstrated. It has been found that with RF power increasing, the deposition rate of the PLA target also increases. Dependency in the lower power region is almost linear, and compared to other polymers, such as PE and PP, the deposition rate is higher for PLA. XPS and FTIR analysis shows that with an increase of RF power, the concentration of C–C/C–H bonds in the films, on the expanse of C:O bonds.
2. PLA-based plasma polymer thin film can be used as an adhesion layer to deposit NPs on the substrate with a lower reflection probability. However, the NPs fabrication and transport control remains one of the crucial parameters, therefore, needs to be investigated deeper.
3. Using in-situ UV-Vis NPs trap region was detected in the planar magnetron GAS. The flow of the Ar as a carrier gas was characterized using CFD. It was found that the trap region distance from the magnetron strongly depends on the Ar gas flow velocity. It appears that novel, post-cylindrical magnetron-based GAS also has an NPs trap region.
4. Brownian diffusion could be one of the most impacted parameters that allow small NPs to escape the NPs trap. However, at the same time could be responsible for NPs loss in the GAS' aggregation chamber walls.
5. The velocity of the carrier gas strongly depends on the carrier gas inlet configuration in the GAS. This is true for planar magnetron-based GAS, as well as for post-cylindrical magnetron-based GAS.
6. Using the CFD, we could understand the carrier gas flow performance in systems for composite NPs fabrication. With this, it could help us control crucial parameters such as particle residence time in the plasma region.
7. Overall, CFD proved to be an excellent tool to visualise, understand, and optimise carrier gas flow performance in magnetron-based GAS systems. This could potentially contribute to the wide implementation of gas aggregation cluster sources in the industry.

Bibliography

[1] J. A. Bittencourt, "CHAPTER 1 - Introduction," in *Fundamentals of Plasma Physics*, J. A. Bittencourt, Ed., Amsterdam: Pergamon, 1986, pp. 1–32. doi: 10.1016/B978-0-08-033923-8.50005-7.

[2] P. Debye, "The theory of electrolytes. I. Freezing point depression and related phenomena (Translation)," *Zur Theorie der Elektrolyte. I. Gefrierpunktserniedrigung und verwandte Erscheinungen*, Jul. 2019, Accessed: Nov. 13, 2022. [Online]. Available: https://minds.wisconsin.edu/handle/1793/79225

[3] F. F. Chen, "Introduction," in *Introduction to Plasma Physics*, F. F. Chen, Ed., Boston, MA: Springer US, 1974, pp. 1–16. doi: 10.1007/978-1-4757-0459-4_1.

[4] "Basic Plasma Equations and Equilibrium," in *Principles of Plasma Discharges and Materials Processing*, John Wiley & Sons, Ltd, 2005, pp. 23–42. doi: 10.1002/0471724254.ch2.

[5] H. Biederman and Y. Osada, *Plasma Polymerization Processes*, 1st edition. Amsterdam ; New York : New York, N.Y., U.S.A: Elsevier Science, 1992.

[6] A. C. Cummings *et al.*, "GALACTIC COSMIC RAYS IN THE LOCAL INTERSTELLAR MEDIUM: VOYAGER 1 OBSERVATIONS AND MODEL RESULTS," *ApJ*, vol. 831, no. 1, p. 18, Oct. 2016, doi: 10.3847/0004-637X/831/1/18.

[7] K. M. Ferrière, "The interstellar environment of our galaxy," *Rev. Mod. Phys.*, vol. 73, no. 4, pp. 1031–1066, Dec. 2001, doi: 10.1103/RevModPhys.73.1031.

[8] I. R. Lindemuth and R. E. Siemon, "The fundamental parameter space of controlled thermonuclear fusion," *American Journal of Physics*, vol. 77, no. 5, pp. 407–416, May 2009, doi: 10.1119/1.3096646.

[9] R. Hippler, *Low temperature plasma physics: fundamental aspects and applications*, 1st ed. Berlin: Wiley-VCH, 2001. [Online]. Available: https://go.exlibris.link/fgN01hHj

[10] R. Eason, Ed., *Pulsed Laser Deposition of Thin Films: Applications-Led Growth of Functional Materials*, 1st edition. Hoboken, N.J: Wiley-Interscience, 2006.

[11] P. Sigmund, "Sputtering by ion bombardment theoretical concepts," in *Sputtering by Particle Bombardment I: Physical Sputtering of Single-Element Solids*, R. Behrisch, Ed., in Topics in Applied Physics. Berlin, Heidelberg: Springer, 1981, pp. 9–71. doi: 10.1007/3540105212_7.

[12] J. Bohdansky, "A universal relation for the sputtering yield of monatomic solids at normal ion incidence," *Nuclear Instruments and Methods in Physics Research Section B: Beam Interactions with Materials and Atoms*, vol. 2, no. 1, pp. 587–591, Mar. 1984, doi: 10.1016/0168-583X(84)90271-4.

[13] P. M. Morse, "Diatomic Molecules According to the Wave Mechanics. II. Vibrational Levels," *Phys. Rev.*, vol. 34, no. 1, pp. 57–64, Jul. 1929, doi: 10.1103/PhysRev.34.57.

[14] J. E. Jones and S. Chapman, "On the determination of molecular fields.—I. From the variation of the viscosity of a gas with temperature," *Proceedings of the Royal Society of London. Series A, Containing Papers of a Mathematical and Physical Character*, vol. 106, no. 738, pp. 441–462, Oct. 1924, doi: 10.1098/rspa.1924.0081.

[15] J. E. Jones and S. Chapman, "On the determination of molecular fields. —II. From the equation of state of a gas," *Proceedings of the Royal Society of London. Series A, Containing Papers of a Mathematical and Physical Character*, vol. 106, no. 738, pp. 463–477, Oct. 1924, doi: 10.1098/rspa.1924.0082.

[16] W. Eckstein, S. Hackel, D. Heinemann, and B. Fricke, "Influence of the interaction potential on simulated sputtering and reflection data," *Z Phys D - Atoms, Molecules and Clusters*, vol. 24, no. 2, pp. 171–176, Jun. 1992, doi: 10.1007/BF01426703.

[17] H. P. Bonzel and R. Ku, “Mechanisms of the catalytic carbon monoxide oxidation on Pt (110),” *Surface Science*, vol. 33, no. 1, pp. 91–106, Oct. 1972, doi: 10.1016/0039-6028(72)90101-X.
[18] W. Eckstein, “Computer simulation of ion surface collisions with special emphasis to the work by Yamamura,” *Nuclear instruments & methods in physics research. Section B, Beam interactions with materials and atoms*, vol. 232, no. 1, pp. 108–116, 2005, doi: 10.1016/j.nimb.2005.03.032.
[19] A. A. Dzhurakhalov, “Computer simulation of ion-solid interaction processes,” *Microelectronic Engineering*, vol. 69, no. 2, pp. 570–576, Sep. 2003, doi: 10.1016/S0167-9317(03)00348-4.
[20] Z. B. Güvenç, Y. Hundur, and R. Hippler, “Sputtering yield and dynamical analysis of Ni(100) surface: A comparison of four different Ar-surface interaction potentials,” *Nuclear Instruments and Methods in Physics Research Section B: Beam Interactions with Materials and Atoms*, vol. 164–165, pp. 854–860, Apr. 2000, doi: 10.1016/S0168-583X(99)01109-X.
[21] H. Yakup, Z. B. Güvenç, and H. Rainer, “Dynamical Analysis of Sputtering at Threshold Energy Range: Modelling of Ar+Ni(100) Collision System,” *Chinese Phys. Lett.*, vol. 25, no. 2, p. 730, Feb. 2008, doi: 10.1088/0256-307X/25/2/102.
[22] C. Jeynes, “Elastic Backscattering of Ions for Compositional Analysis,” in *Characterization of Materials*, John Wiley & Sons, Ltd, 2012, pp. 1–21. doi: 10.1002/0471266965.com092.pub2.
[23] I. A. E. Agency, “Atomic and Plasma–Material Interaction Data for Fusion,” vol. 1, p. 93, 1991.
[24] G. A. Somorjai and Y. Li, *Introduction to Surface Chemistry and Catalysis*, 2nd edition. Hoboken, N.J: Wiley, 2010.
[25] H. König and G. Helwig, “Über dünne aus Kohlenwasserstoffen durch Elektronen- oder Ionenbeschuß gebildete Schichten,” *Z. Physik*, vol. 129, no. 5, pp. 491–503, Sep. 1951, doi: 10.1007/BF01330048.
[26] H. Schüler and L. Reinebeck, “Über neue Spektren in der Glimmentladung mit Naphthalindampf,” *Zeitschrift für Naturforschung A*, vol. 6, no. 5, pp. 270–275, May 1951, doi: 10.1515/zna-1951-0509.
[27] H. Yasuda, Ed., “Front Matter,” in *Plasma Polymerization*, Academic Press, 1985, p. iii. doi: 10.1016/B978-0-12-768760-5.50001-3.
[28] N. Inagaki, *Plasma Surface Modification and Plasma Polymerization*. Technomic Publishing, 1996. doi: 10.1201/9781498710831.
[29] H. Biederman, Ed., *PLASMA POLYMER FILMS*. London: ICP, 2004.
[30] D. K. Lam, R. F. Baddour, and A. F. Stancell, “A Mechanisms and Kinetics Study of Polymeric Thin-Film Deposition in Glow Discharge,” *Journal of Macromolecular Science: Part A - Chemistry*, vol. 10, no. 3, pp. 421–450, Mar. 1976, doi: 10.1080/00222337608061191.
[31] H. Yasuda, *Plasma Polymerization*. Academic Press, 1985.
[32] R. d’Agostino, F. Cramarossa, V. Colaprico, and R. d’Ettole, “Mechanisms of etching and polymerization in radiofrequency discharges of CF4–H2, CF4–C2F4, C2F6–H2, C3F8–H2,” *Journal of Applied Physics*, vol. 54, no. 3, pp. 1284–1288, Mar. 1983, doi: 10.1063/1.332193.
[33] O. Kylián, A. Choukourov, and H. Biederman, “Nanostructured plasma polymers,” *Thin Solid Films*, vol. 548, pp. 1–17, Dec. 2013, doi: 10.1016/j.tsf.2013.09.003.
[34] H. S. Butler and G. S. Kino, “Plasma Sheath Formation by Radio-Frequency Fields,” *The Physics of Fluids*, vol. 6, no. 9, pp. 1346–1355, Sep. 1963, doi: 10.1063/1.1706905.

[35] I. H. Pratt and T. C. Lausman, “Some characteristics of sputtered polytetrafluoroethylene films,” *Thin Solid Films*, vol. 10, no. 1, pp. 151–154, Apr. 1972, doi: 10.1016/0040-6090(72)90281-7.
[36] J. M. Tibbitt, M. Shen, and A. T. Bell, “A comparison of r.f. sputtered and plasma polymerized thin films of tetrafluoroethylene,” *Thin Solid Films*, vol. 29, no. 2, pp. L43–L45, Oct. 1975, doi: 10.1016/0040-6090(75)90187-X.
[37] H. Biederman, S. M. Ojha, and L. Holland, “The properties of fluorocarbon films prepared by r.f. sputtering and plasma polymerization in inert and active gas,” *Thin Solid Films*, vol. 41, no. 3, pp. 329–339, Mar. 1977, doi: 10.1016/0040-6090(77)90319-4.
[38] H. Biederman, “Fluorocarbon films sputtered under various conditions,” *Thin Solid Films*, vol. 55, no. 3, pp. L11–L13, Dec. 1978, doi: 10.1016/0040-6090(78)90170-0.
[39] N. Maréchal and Y. Pauleau, “Radio frequency sputtering process of a polytetrafluoroethylene target and characterization of fluorocarbon polymer films,” *Journal of Vacuum Science & Technology A*, vol. 10, no. 3, pp. 477–483, May 1992, doi: 10.1116/1.578174.
[40] M. E. Ryan, J. L. C. Fonseca, S. Tasker, and J. P. S. Badyal, “Plasma Polymerization of Sputtered Poly(tetrafluoroethylene),” *J. Phys. Chem.*, vol. 99, no. 18, pp. 7060–7064, May 1995, doi: 10.1021/j100018a044.
[41] H. Biederman, P. Bílková, J. Ježek, P. Hlídek, and D. Slavínská, “RF magnetron sputtering of polymers,” *Journal of Non-Crystalline Solids*, vol. 218, pp. 44–49, Sep. 1997, doi: 10.1016/S0022-3093(97)00196-8.
[42] Y. Pihosh *et al.*, “Composite SiOx/fluorocarbon plasma polymer films prepared by r.f. magnetron sputtering of SiO2 and PTFE,” *Vacuum*, vol. 81, no. 1, pp. 38–44, Sep. 2006, doi: 10.1016/j.vacuum.2006.02.007.
[43] M. Drábik *et al.*, “Super-Hydrophobic Coatings Prepared by RF Magnetron Sputtering of PTFE,” *Plasma Processes and Polymers*, vol. 7, no. 7, pp. 544–551, 2010, doi: 10.1002/ppap.200900164.
[44] J. P. Youngblood and T. J. McCarthy, “Plasma polymerization using solid phase polymer reactants (non-classical sputtering of polymers),” *Thin Solid Films*, vol. 382, no. 1, pp. 95–100, Feb. 2001, doi: 10.1016/S0040-6090(00)01683-7.
[45] I. Kholodkov, H. Biederman, D. Slavínská, A. Choukourov, and M. Trchova, “Plasma polymers prepared by RF sputtering of polyethylene,” *Vacuum*, vol. 70, no. 4, pp. 505–509, Apr. 2003, doi: 10.1016/S0042-207X(02)00702-9.
[46] J. Hanus, J. Kousal, A. Choukourov, H. Biederman, and D. Slavinska, “RF Magnetron Sputtering of Poly(propylene) in a Mixture of Argon and Nitrogen,” *Plasma Processes and Polymers*, vol. 4, no. S1, pp. S806–S811, 2007, doi: 10.1002/ppap.200731910.
[47] V. Stelmashuk, H. Biederman, D. Slavínská, M. Trchová, and P. Hlidek, “Rf magnetron sputtering of polypropylene,” *Vacuum*, vol. 75, no. 3, pp. 207–215, Jul. 2004, doi: 10.1016/j.vacuum.2004.02.007.
[48] J. Kousal *et al.*, “RF magnetron sputtering and evaporation of polyisobutylene and low density polyethylene,” *Surface and Coatings Technology*, vol. 200, no. 1, pp. 472–475, Oct. 2005, doi: 10.1016/j.surfcoat.2005.02.107.
[49] Y. Yamada, K. Tanaka, and K. Saito, “Friction and damage of coatings formed by sputtering polytetrafluoroethylene and polyimide,” *Surface and Coatings Technology*, vol. 43–44, pp. 618–628, Dec. 1990, doi: 10.1016/0257-8972(90)90006-X.
[50] M. Kitoh and Y. Honda, “Preparation and tribological properties of sputtered polyimide film,” *Thin Solid Films*, vol. 271, no. 1, pp. 92–95, Dec. 1995, doi: 10.1016/0040-6090(95)06697-7.
[51] G. A. Hishmeh, T. L. Barr, A. Sklyarov, and S. Hardcastle, “Thin polymer films prepared by radio frequency plasma sputtering of polytetrafluoroethylene and polyetherimide

targets," *Journal of Vacuum Science & Technology A*, vol. 14, no. 3, pp. 1330–1338, May 1996, doi: 10.1116/1.579950.
[52] H. Biederman, "Organic films prepared by polymer sputtering," *Journal of Vacuum Science & Technology A*, vol. 18, no. 4, pp. 1642–1648, Jul. 2000, doi: 10.1116/1.582399.
[53] K. Fukushima, Y. Ikeda, T. Hayashi, N. Kikuchi, E. Kusano, and A. Kinbara, "Imidized organic thin films deposited on glass substrates," *Thin Solid Films*, vol. 392, no. 2, pp. 254–257, Jul. 2001, doi: 10.1016/S0040-6090(01)01037-9.
[54] A. Kinbara, T. Hayashi, K. Wakahara, N. Kikuchi, E. Kusano, and H. Nanto, "Polyimide-based organic thin films prepared by rf magnetron sputtering," *Thin Solid Films*, vol. 433, no. 1, pp. 274–276, Jun. 2003, doi: 10.1016/S0040-6090(03)00297-9.
[55] A. Choukourov *et al.*, "Plasma polymer films from sputtered polyimide," *Vacuum*, vol. 81, no. 4, pp. 517–526, Nov. 2006, doi: 10.1016/j.vacuum.2006.07.010.
[56] O. Kylián *et al.*, "Deposition of amino-rich coatings by RF magnetron sputtering of Nylon: In-situ characterization of the deposition process," *Surface and Coatings Technology*, vol. 205, pp. S558–S561, Jul. 2011, doi: 10.1016/j.surfcoat.2011.01.036.
[57] N. Menegazzo, D. Boyne, H. Bui, T. P. Beebe, and K. S. Booksh, "DC magnetron sputtered polyaniline-HCl thin films for chemical sensing applications," *Anal Chem*, vol. 84, no. 13, pp. 5770–5777, Jul. 2012, doi: 10.1021/ac301006f.
[58] Y. Wang, Y. Ye, H. Li, L. Ji, J. Chen, and H. Zhou, "A magnetron sputtering technique to prepare a-C:H films: Effect of substrate bias," *Applied Surface Science*, vol. 257, no. 6, pp. 1990–1995, Jan. 2011, doi: 10.1016/j.apsusc.2010.09.040.
[59] M. M. Hawkeye and M. J. Brett, "Glancing angle deposition: Fabrication, properties, and applications of micro- and nanostructured thin films," *Journal of Vacuum Science & Technology A*, vol. 25, no. 5, pp. 1317–1335, Sep. 2007, doi: 10.1116/1.2764082.
[60] O. Kylian *et al.*, "Plasma polymers: From thin films to nanocolumnar coatings," *Thin Solid Films*, vol. 630, pp. 86–91, May 2017, doi: 10.1016/j.tsf.2016.08.054.
[61] A. Choukourov *et al.*, "Structured Ti/Hydrocarbon Plasma Polymer Nanocomposites Produced By Magnetron Sputtering with Glancing Angle Deposition," *Plasma Processes and Polymers*, vol. 7, no. 1, pp. 25–32, 2010, doi: 10.1002/ppap.200900064.
[62] A. Grinevich *et al.*, "Nanocomposite Ti/hydrocarbon plasma polymer films from reactive magnetron sputtering as growth support for osteoblast-like and endothelial cells," *Journal of Biomedical Materials Research Part A*, vol. 88A, no. 4, pp. 952–966, 2009, doi: 10.1002/jbm.a.31918.
[63] K. Vasilev, "Nanoengineered Plasma Polymer Films for Biomaterial Applications," *Plasma Chem Plasma Process*, vol. 34, no. 3, pp. 545–558, May 2014, doi: 10.1007/s11090-013-9506-0.
[64] S. Seino, S. Sasaki, T. Owashi, K. Oya, and S. Iwamori, "Effects of copper interfacial layer on surface characteristics, adhesion and wear durability of fluorocarbon thin film sputtered onto polyimide film substrate," *Vacuum*, vol. 111, pp. 160–165, Jan. 2015, doi: 10.1016/j.vacuum.2014.10.001.
[65] A. Kuzminova, J. Kratochvíl, A. Shelemin, O. Kylián, H. Biederman, and J. Beranová, "Preparation of Antibacterial Silver Containing Nanocomposites," *WDS 2013*, pp. 102–107, 2014.
[66] H. Palza, "Antimicrobial Polymers with Metal Nanoparticles," *International Journal of Molecular Sciences*, vol. 16, no. 1, Art. no. 1, Jan. 2015, doi: 10.3390/ijms16012099.
[67] L. Tamayo, M. Azócar, M. Kogan, A. Riveros, and M. Páez, "Copper-polymer nanocomposites: An excellent and cost-effective biocide for use on antibacterial surfaces," *Materials Science and Engineering: C*, vol. 69, pp. 1391–1409, Dec. 2016, doi: 10.1016/j.msec.2016.08.041.

[68] A. H. Pfund, “BISMUTH BLACK AND ITS APPLICATIONS,” *Review of Scientific Instruments*, vol. 1, no. 7, pp. 397–399, Jul. 1930, doi: 10.1063/1.1748708.
[69] C. J. Duthler, S. E. Johnson, and H. P. Broida, “Plasma-Resonance Scattering from Small Sodium Particles Formed in a Flowing Gas Stream,” *Phys. Rev. Lett.*, vol. 26, no. 20, pp. 1236–1239, May 1971, doi: 10.1103/PhysRevLett.26.1236.
[70] F. Frank, W. Schulze, B. Tesche, J. Urban, and B. Winter, “Formation of metal clusters and molecules by means of the gas aggregation technique and characterisation of size distribution,” *Surface Science*, vol. 156, pp. 90–99, Jun. 1985, doi: 10.1016/0039-6028(85)90561-8.
[71] C. G. Granqvist and R. A. Buhrman, “Ultrafine metal particles,” *Journal of Applied Physics*, vol. 47, no. 5, pp. 2200–2219, May 1976, doi: 10.1063/1.322870.
[72] Y. Huttel, *Gas-Phase Synthesis of Nanoparticles*. John Wiley & Sons, 2017.
[73] J. Kousal *et al.*, “Magnetron-sputtered copper nanoparticles: lost in gas aggregation and found by in situ X-ray scattering,” *Nanoscale*, vol. 10, no. 38, pp. 18275–18281, Oct. 2018, doi: 10.1039/C8NR06155F.
[74] A. Shelemin *et al.*, “Nucleation and Growth of Magnetron-Sputtered Ag Nanoparticles as Witnessed by Time-Resolved Small Angle X-Ray Scattering,” *Particle & Particle Systems Characterization*, vol. 37, no. 2, p. 1900436, 2020, doi: 10.1002/ppsc.201900436.
[75] H. Haberland, M. Mall, M. Moseler, Y. Qiang, T. Reiners, and Y. Thurner, “Filling of micron-sized contact holes with copper by energetic cluster impact,” *Journal of Vacuum Science & Technology A*, vol. 12, no. 5, pp. 2925–2930, Sep. 1994, doi: 10.1116/1.578967.
[76] D. Datta, S. R. Bhattacharyya, I. Shyjumon, D. Ghose, and R. Hippler, “Production and deposition of energetic metal nanocluster ions of silver on Si substrates,” *Surface and Coatings Technology*, vol. 203, no. 17, pp. 2452–2457, Jun. 2009, doi: 10.1016/j.surfcoat.2009.02.114.
[77] V. Straňák *et al.*, “Size-controlled formation of Cu nanoclusters in pulsed magnetron sputtering system,” *Surface and Coatings Technology*, vol. 205, no. 8, pp. 2755–2762, Jan. 2011, doi: 10.1016/j.surfcoat.2010.10.030.
[78] A. Marek, J. Valter, S. Kadlec, and J. Vyskočil, “Gas aggregation nanocluster source — Reactive sputter deposition of copper and titanium nanoclusters,” *Surface and Coatings Technology*, vol. 205, pp. S573–S576, Jul. 2011, doi: 10.1016/j.surfcoat.2010.12.027.
[79] M. Gracia-Pinilla, E. Martínez, G. S. Vidaurri, and E. Pérez-Tijerina, “Deposition of Size-Selected Cu Nanoparticles by Inert Gas Condensation,” *Nanoscale Res Lett*, vol. 5, no. 1, Art. no. 1, Jan. 2010, doi: 10.1007/s11671-009-9462-z.
[80] T. Kretková *et al.*, “In-flight modification of Ni nanoparticles by tubular magnetron sputtering,” *J. Phys. D: Appl. Phys.*, vol. 52, no. 20, p. 205302, Mar. 2019, doi: 10.1088/1361-6463/ab00d0.
[81] O. Kylián *et al.*, “In-flight plasma modification of nanoparticles produced by means of gas aggregation sources as an effective route for the synthesis of core-satellite Ag/plasma polymer nanoparticles,” *Plasma Phys. Control. Fusion*, vol. 62, no. 1, p. 014005, Oct. 2019, doi: 10.1088/1361-6587/ab4115.
[82] O. Kylián *et al.*, “Deposition of Pt nanoclusters by means of gas aggregation cluster source,” *Materials Letters*, vol. 79, pp. 229–231, Jul. 2012, doi: 10.1016/j.matlet.2012.04.022.
[83] A. Shelemin *et al.*, “Preparation of metal oxide nanoparticles by gas aggregation cluster source,” *Vacuum*, vol. 120, pp. 162–169, Oct. 2015, doi: 10.1016/j.vacuum.2015.07.008.

[84] O. Polonskyi *et al.*, “Nylon-sputtered nanoparticles: fabrication and basic properties,” *J. Phys. D: Appl. Phys.*, vol. 45, no. 49, p. 495301, Nov. 2012, doi: 10.1088/0022-3727/45/49/495301.
[85] J. D. Anderson, Jr., *Computational Fluid Dynamics. The Basics with applications*, International Edition. New York: McGraw-Hill Education, 1995.
[86] J. H. Ferziger, M. Perić, and R. L. Street, *Computational Methods for Fluid Dynamics*, 4th ed. 2020 edition. Cham: Springer, 2019.
[87] T. H. Pulliam and D. W. Zingg, *Fundamental Algorithms in Computational Fluid Dynamics*, 2014th edition. Cham ; New York: Springer, 2014.
[88] R. Rudd *et al.*, “Manipulation of cluster formation through gas-wall boundary conditions in large area cluster sources,” *Surface and Coatings Technology*, vol. 314, pp. 125–130, Mar. 2017, doi: 10.1016/j.surfcoat.2016.10.058.
[89] Siemens Industry Software Inc. 2021, “Simcenter STAR-CCM+ - User Guide.” https://docs.sw.siemens.com/en-US/product/226870983/doc/PL20210730658209000.starccmp_userguide_html/custom/?audience=external (accessed Jan. 30, 2022).
[90] J. C. Maxwell, “VII. On stresses in rarified gases arising from inequalities of temperature,” *Philosophical Transactions of the Royal Society of London*, vol. 170, pp. 231–256, Jan. 1879, doi: 10.1098/rstl.1879.0067.
[91] L. Zhang, J. Shao, and X. Chen, “Numerical simulation of nanocluster motion through a DC magnetron nanocluster source,” *Vacuum*, vol. 128, pp. 137–145, Jun. 2016, doi: 10.1016/j.vacuum.2016.03.011.
[92] L. Zhang, J. Shao, and X. Chen, “CFD simulation of nozzle characteristics in a gas aggregation cluster source,” *Vacuum*, vol. 129, pp. 105–110, Jul. 2016, doi: 10.1016/j.vacuum.2016.04.020.
[93] R. Rudd *et al.*, “Plasma gas aggregation cluster source: Influence of gas inlet configuration and total surface area on the heterogeneous aggregation of silicon clusters,” *Surface and Coatings Technology*, vol. 364, pp. 1–6, Apr. 2019, doi: 10.1016/j.surfcoat.2019.02.074.
[94] G. Sanzone, J. Yin, K. Cooke, H. Sun, and P. Lievens, “Impact of the gas dynamics on the cluster flux in a magnetron cluster-source: Influence of the chamber shape and gas-inlet position,” *Review of Scientific Instruments*, vol. 92, no. 3, p. 033901, Mar. 2021, doi: 10.1063/5.0028854.
[95] Š. Batková, T. Kozák, S. Haviar, P. Mareš, and J. Čapek, “Effect of exit-orifice diameter on Cu nanoparticles produced by gas-aggregation source,” *Surface and Coatings Technology*, vol. 417, p. 127196, Jul. 2021, doi: 10.1016/j.surfcoat.2021.127196.
[96] D. Nikitin *et al.*, “Novel gas aggregation cluster source based on post magnetron,” *Plasma Processes and Polymers*, vol. 18, no. 9, p. 2100068, 2021, doi: 10.1002/ppap.202100068.
[97] J. Drewes *et al.*, “Impact of argon flow and pressure on the trapping behavior of nanoparticles inside a gas aggregation source,” *Plasma Processes and Polymers*, vol. 19, no. 1, p. 2100125, 2022, doi: 10.1002/ppap.202100125.
[98] D. Nikitin *et al.*, “The evolution of Ag nanoparticles inside a gas aggregation cluster source,” *Plasma Processes and Polymers*, vol. 16, no. 10, p. 1900079, 2019, doi: 10.1002/ppap.201900079.
[99] S. Ali-Ogly *et al.*, “Computational fluid dynamics predicts the nanoparticle transport in gas aggregation cluster sources,” *J. Phys. D: Appl. Phys.*, vol. 55, no. 44, p. 445203, Sep. 2022, doi: 10.1088/1361-6463/ac8c4e.
[100] F. Jimenez, S. Ekpe, and S. Dew, “Modeling of Low Pressure Magnetron Plasma Discharge,” presented at the Excerpt from the Proceedings of the COMSOL Conference, Boston, Boston, 2007. [Online]. Available:

https://www.researchgate.net/publication/265991858_Modeling_of_Low_Pressure_Magnetron_Plasma_Discharge
[101] S. Chuon, “Simulation numérique multi-échelles du procédé de dépôt par pulvérisation cathodique magnétron,” phdthesis, Université d’Orléans ; Universiteit Antwerpen, 2019. Accessed: Jan. 30, 2022. [Online]. Available: https://tel.archives-ouvertes.fr/tel-03128453
[102] M. C. Potter, D. C. Wiggert, and B. H. Ramadan, *Mechanics of Fluids SI Version*. Cengage Learning, 2012.
[103] “OpenFoam-User Guide.” https://www.openfoam.com/documentation/user-guide (accessed Feb. 19, 2022).
[104] E. Cunningham and J. Larmor, “On the velocity of steady fall of spherical particles through fluid medium,” *Proceedings of the Royal Society of London. Series A, Containing Papers of a Mathematical and Physical Character*, vol. 83, no. 563, pp. 357–365, Mar. 1910, doi: 10.1098/rspa.1910.0024.
[105] A. Li and G. Ahmadi, “Dispersion and Deposition of Spherical Particles from Point Sources in a Turbulent Channel Flow,” *Aerosol Science and Technology*, vol. 16, no. 4, pp. 209–226, Jan. 1992, doi: 10.1080/02786829208959550.
[106] M. D. Allen and O. G. Raabe, “Slip Correction Measurements of Spherical Solid Aerosol Particles in an Improved Millikan Apparatus,” *Aerosol Science and Technology*, vol. 4, no. 3, pp. 269–286, Jan. 1985, doi: 10.1080/02786828508959055.
[107] C. N. Davies, “Definitive equations for the fluid resistance of spheres,” *Proc. Phys. Soc.*, vol. 57, no. 4, pp. 259–270, Jul. 1945, doi: 10.1088/0959-5309/57/4/301.
[108] G. Marsaglia and T. A. Bray, “A Convenient Method for Generating Normal Variables,” *SIAM Review*, vol. 6, no. 3, pp. 260–264, 1964.
[109] J. Kousal *et al.*, “Characterization of nanoparticle flow produced by gas aggregation source,” *Vacuum*, vol. 96, pp. 32–38, Oct. 2013, doi: 10.1016/j.vacuum.2013.02.015.
[110] B. M. Smirnov, I. Shyjumon, and R. Hippler, “Flow of nanosize cluster-containing plasma in a magnetron discharge,” *Phys. Rev. E*, vol. 75, no. 6, p. 066402, Jun. 2007, doi: 10.1103/PhysRevE.75.066402.
[111] F. Di Fonzo *et al.*, “Focused nanoparticle-beam deposition of patterned microstructures,” *Applied Physics Letters*, vol. 77, no. 6, pp. 910–912, 2000, doi: 10.1063/1.1306638.
[112] P. Piseri, A. Podestà, E. Barborini, and P. Milani, “Production and characterization of highly intense and collimated cluster beams by inertial focusing in supersonic expansions,” *Review of Scientific Instruments*, vol. 72, no. 5, pp. 2261–2267, 2001, doi: 10.1063/1.1361082.
[113] J. Kousal, “Diagnostika procesu plazmové polymerace,” PhD Dissertation, Univerzita Karlova (Charles University), 2006.
[114] A. M. Ahadi *et al.*, “Core@shell nanoparticles by inflight controlled coating,” *J. Phys. D: Appl. Phys.*, vol. 55, no. 21, p. 215201, Feb. 2022, doi: 10.1088/1361-6463/ac5559.
[115] C. Lu and A. W. Czanderna, *Applications of Piezoelectric Quartz Crystal Microbalances / edited by C. Lu and A.W. Czanderna.* in Methods and Phenomena. Oxford: Elsevier Science, 1984.
[116] B. H. Stuart, *Infrared Spectroscopy: Fundamentals and Applications*, 1st edition. Chichester, West Sussex, England ; Hoboken, NJ: Wiley, 2004.
[117] H. Fujiwara, *Spectroscopic Ellipsometry: Principles and Applications*, 1st edition. Chichester, England ; Hoboken, NJ: Wiley, 2007.
[118] L. Reimer, *Scanning Electron Microscopy: Physics of Image Formation and Microanalysis*. Berlin Heidelberg: Springer, 2010.
[119] T. Sunaoshi, K. Kaji, Y. Orai, C. T. Schamp, and E. Voelkl, “STEM/SEM, Chemical Analysis, Atomic Resolution and Surface Imaging At ≤ 30 kV with No Aberration

Correction for Nanomaterials on Graphene Support," *Microscopy and Microanalysis*, vol. 22, no. S3, pp. 604–605, Jul. 2016, doi: 10.1017/S1431927616003871.
[120] V. Kazmiruk, *Scanning Electron Microscopy*. 2012. doi: 10.5772/1973.
[121] O. Martin and L. Avérous, "Poly(lactic acid): plasticization and properties of biodegradable multiphase systems," *Polymer*, vol. 42, no. 14, pp. 6209–6219, Jun. 2001, doi: 10.1016/S0032-3861(01)00086-6.
[122] R. P. Pawar, S. U. Tekale, S. U. Shisodia, J. T. Totre, and A. J. Domb, "Biomedical Applications of Poly(Lactic Acid)," *Recent Patents on Regenerative Medicine*, vol. 4, no. 1, pp. 40–51.
[123] V. DeStefano, S. Khan, and A. Tabada, "Applications of PLA in modern medicine," *Engineered Regeneration*, vol. 1, pp. 76–87, Jan. 2020, doi: 10.1016/j.engreg.2020.08.002.
[124] G. Beamson and D. R. Briggs, "High Resolution XPS of Organic Polymers: The Scienta ESCA300 Database," 1992.
[125] Z. Krtouš *et al.*, "Thin films of cross-linked polylactic acid as tailored platforms for controlled drug release," *Surface and Coatings Technology*, vol. 421, p. 127402, Sep. 2021, doi: 10.1016/j.surfcoat.2021.127402.
[126] P. Solař, J. Kousal, J. Hanuš, K. Škorvánková, A. Kuzminova, and O. Kylián, "Mechanical time-of-flight filter based on slotted disks and helical rotor for measurement of velocities of nanoparticles," *Sci Rep*, vol. 11, no. 1, Art. no. 1, Mar. 2021, doi: 10.1038/s41598-021-85533-7.
[127] J. G. Partridge *et al.*, "Templated-assembly of conducting antimony cluster wires," *Nanotechnology*, vol. 15, no. 9, p. 1382, Aug. 2004, doi: 10.1088/0957-4484/15/9/045.
[128] R. Reichel *et al.*, "From the adhesion of atomic clusters to the fabrication of nanodevices," *Appl. Phys. Lett.*, vol. 89, no. 21, p. 213105, Nov. 2006, doi: 10.1063/1.2387894.
[129] R. Reichel, J. G. Partridge, and S. A. Brown, "Characterization of a template process for conducting cluster-assembled wires," *Appl. Phys. A*, vol. 97, no. 2, pp. 315–321, Nov. 2009, doi: 10.1007/s00339-009-5385-x.
[130] J. Kratochvíl, A. Kuzminova, O. Kylián, and H. Biederman, "Comparison of magnetron sputtering and gas aggregation nanoparticle source used for fabrication of silver nanoparticle films," *Surface and Coatings Technology*, vol. 275, pp. 296–302, Aug. 2015, doi: 10.1016/j.surfcoat.2015.05.003.
[131] A. Palmero, E. D. van Hattum, W. M. Arnoldbik, A. M. Vredenberg, and F. H. P. M. Habraken, "Characterization of the plasma in a radio-frequency magnetron sputtering system," *Journal of Applied Physics*, vol. 95, no. 12, pp. 7611–7618, Jun. 2004, doi: 10.1063/1.1728295.
[132] A. Palmero, E. D. van Hattum, W. M. Arnoldbik, and F. H. P. M. Habraken, "Argon plasma modelling in a RF magnetron sputtering system," *Surface and Coatings Technology*, vol. 188–189, pp. 392–398, Nov. 2004, doi: 10.1016/j.surfcoat.2004.08.032.
[133] P. Sigurjonsson and J. T. Gudmundsson, "Plasma parameters in a planar dc magnetron sputtering discharge of argon and krypton," *J. Phys.: Conf. Ser.*, vol. 100, no. 6, p. 062018, Mar. 2008, doi: 10.1088/1742-6596/100/6/062018.
[134] D. J. Field, S. K. Dew, and R. E. Burrell, "Spatial survey of a magnetron plasma sputtering system using a Langmuir probe," *Journal of Vacuum Science & Technology A*, vol. 20, no. 6, pp. 2032–2041, Nov. 2002, doi: 10.1116/1.1515800.
[135] M. A. Lieberman and A. J. Lichtenberg, *Principles of Plasma Discharges and Materials Processing*, 2nd edition. Wiley-Interscience, 2005.

[136] A. Kolpaková, A. Shelemin, J. Kousal, P. Kudrna, M. Tichý, and H. Biederman, "Langmuir Probe Diagnostic in Gas Aggregation Cluster Source," *WDS'16 Proceedings of Contributed Papers - Physics*, pp. 155–160, 2016.
[137] A. Kolpaková, A. Shelemin, P. Kudrna, M. Tichý, and H. Biederman, "Study of Gas Aggregation Cluster Source by Means of Probe Diagnostic," *WDS'17 Proceedings of Contributed Papers - Physics*, pp. 121–126, 2017.
[138] M. Ganeva, A. V. Pipa, and R. Hippler, "The influence of target erosion on the mass spectra of clusters formed in the planar DC magnetron sputtering source," *Surface and Coatings Technology*, vol. 213, pp. 41–47, Dec. 2012, doi: 10.1016/j.surfcoat.2012.10.012.
[139] J. Vernieres *et al.*, "Gas Phase Synthesis of Multifunctional Fe-Based Nanocubes," *Advanced Functional Materials*, vol. 27, no. 11, p. 1605328, 2017, doi: 10.1002/adfm.201605328.
[140] Y. Huttel, L. Martínez, A. Mayoral, and I. Fernández, "Gas-phase synthesis of nanoparticles: present status and perspectives," *MRS Communications*, vol. 8, no. 3, pp. 947–954, Sep. 2018, doi: 10.1557/mrc.2018.169.
[141] O. Kylián, J. Kratochvíl, J. Hanuš, O. Polonskyi, P. Solař, and H. Biederman, "Fabrication of Cu nanoclusters and their use for production of Cu/plasma polymer nanocomposite thin films," *Thin Solid Films*, vol. 550, pp. 46–52, Jan. 2014, doi: 10.1016/j.tsf.2013.10.029.
[142] J. Hanuš *et al.*, "Deposition of Cu/a-C:H Nanocomposite Films," *Plasma Processes and Polymers*, vol. 13, no. 9, pp. 879–887, 2016, doi: 10.1002/ppap.201500208.

List of Publications

Reviewed journals

1. **Ali-Ogly, S**.; Kučerová, L.; Krtouš, Z.; Kousal, J. Surface Modification by Plasma-Based and Related Methods Demonstrated on Magnetron Sputtering of Polylactic Acid. In WDS'19 Proceedings of Contributed Papers — Physics; MATFYZPRESS, 2019; pp 39–44.

2. Shelemin, A.; Pleskunov, P.; Kousal, J.; Drewes, J.; Hanuš, J.; **Ali-Ogly, S**.; Nikitin, D.; Solař, P.; Kratochvíl, J.; Vaidulych, M.; Schwartzkopf, M.; Kylián, O.; Polonskyi, O.; Strunskus, T.; Faupel, F.; Roth, S. V.; Biederman, H.; Choukourov, A. Nucleation and Growth of Magnetron-Sputtered Ag Nanoparticles as Witnessed by Time-Resolved Small Angle X-Ray Scattering. Particle & Particle Systems Characterization 2020, 37 (2), 1900436.

3. Nikitin, D.; Hanuš, J.; **Ali-Ogly, S**.; Polonskyi, O.; Drewes, J.; Faupel, F.; Biederman, H.; Choukourov, A. The Evolution of Ag Nanoparticles inside a Gas Aggregation Cluster Source. Plasma Processes and Polymers 2019, 16 (10), 1900079.

4. Krtouš, Z.; Kousal, J.; Sedlaříková, J.; Kolářová Rašková, Z.; Kučerová, L.; Krakovský, I.; Kučera, J.; **Ali-Ogly, S**.; Pleskunov, P.; Choukourov, A. Thin Films of Cross-Linked Polylactic Acid as Tailored Platforms for Controlled Drug Release. Surface and Coatings Technology 2021, 421, 127402.

5. Pleskunov, P.; Košutová, T.; Vaidulych, M.; Nikitin, D.; Krtouš, Z.; **Ali-Ogly, S**.; Kishenina, K.; Tafiichuk, R.; Biederman, H.; Gordeev, I.; Drewes, J.; Barg, I.; Faupel, F.; Cieslar, M.; Yatskiv, R.; Pihosh, Y.; Nandal, V.; Seki, K.; Domen, K.; Choukourov, A. The Sputter-Based Synthesis of Tantalum Oxynitride Nanoparticles with Architecture and Bandgap Controlled by Design. Applied Surface Science 2021, 559, 149974.

6. Nikitin, D.; Hanuš, J.; Pleskunov, P.; Krtouš, Z.; **Ali-Ogly, S**.; Tafiichuk, R.; Biliak, K.; Protsak, M.; Valter, J.; Vyskočil, J.; Choukourov, A.; Biederman, H. Novel Gas Aggregation Cluster Source Based on Post Magnetron. Plasma Processes and Polymers 2021, 18 (9), 2100068.

7. Pleskunov, P.; Prysiazhnyi, V.; Nikitin, D.; Košutová, T.; Cieslar, M.; Gordeev, I.; Krtouš, Z.; **Ali-Ogly, S**.; Šomvársky, J.; Protsak, M.; Biliak, K.; Kishenina, K.; Bednařík, A.; Dopita, M.; Preisler, J.; Choukourov, A. Magnetron-Sputtered Niobium Nanoparticles for Molecular Imaging of Brain Tissues through Surface-Assisted Laser Desorption/Ionization Mass Spectrometry. ACS Appl. Nano Mater. 2022, 5 (9), 12865–12875.

8. Drewes, J.; **Ali-Ogly, S**.; Strunskus, T.; Polonskyi, O.; Biederman, H.; Faupel, F.; Vahl, A. Impact of Argon Flow and Pressure on the Trapping Behavior of Nanoparticles inside a Gas Aggregation Source. Plasma Processes and Polymers 2022, 19 (1), 2100125.

9. **Ali-Ogly, S**.; Kousal, J.; Nikitin, D.; Pleskunov, P.; Hanuš, J.; Choukourov, A.; Biederman, H. Computational Fluid Dynamics Predicts the Nanoparticle Transport in Gas Aggregation Cluster Sources. J. Phys. D: Appl. Phys. 2022, 55 (44), 445203.

10. Biliak, K.; Nikitin, D.; **Ali-Ogly, S**.; Protsak, M.; Pleskunov, P.; Tosca, M.; Sergievskaya, A.; Cornil, D.; Cornil, J.; Konstantinidis, S.; Košutová, T.; Cernochova, Z.; Štěpánek, P.; Hanuš, J.; Kousal, J.; Hanykova, L.; Krakovský, I.; Choukourov, A. Plasmonic Ag/Cu/PEG Nanofluids Prepared When Solids Meet Liquid in the Gas Phase. Nanoscale Adv. 2022.

11. Kylián, O.; Nikitin, D.; Hanuš, J.; **Ali-Ogly, S**.; Pleskunov, P.; Biederman, H. Plasma-assisted gas-phase aggregation of clusters for functional nanomaterials. J. Vac. Sci. Technol. A 41, 020802, 2023

Conferences contributions presented by the author

1. **Ali-Ogly, S**.; Kučerová, L.; Krtouš, Z.; Kousal, J. "Surface Modification by Plasma-Based and Related Methods Demonstrated on Magnetron Sputtering of Polylactic Acid". 28th Annual Conference of Doctoral Students – WDS 2019, Prague, Czech Republic, June 4–6, 2019, *oral presentation*
2. **Ali-Ogly, S**., Nikitin, D., Choukourov, A., Biederman, H., "Flow simulation of silver nanoparticles inside gas aggregation cluster source". 9th International Workshop on Polymer-Metal Nanocomposites, Espoo, Finland, July 22-24, 2019
3. **Ali-Ogly, S**., Nikitin, D., Hanuš, J., Choukourov, A., Biederman, H., "The importance of a gas flow pattern in cluster sources". 29th session in Recent developments in Gas Phase Synthesis of Nanoparticles and applications, online, 15th September 2021, *oral presentation*

List of Abbreviations

AC	Alternating current
BE	Binding energy
BSE	Back-scattered electrons
DC	Direct current
DR	Deposition rate
FTIR	Fourier Transform Infra-Red Spectroscopy
GAS	Gas Aggregation Cluster Source
HAS	Hemispherical analyzer
IR	Infra-Red Spectroscopy
LDPE	Low-density polyethylene
MF	Magnetic field
NPs	Nanoparticles
OES	Optical emission spectroscopy
PAVTD	Plasma-Assisted Vapour Thermal Deposition
PE	Polyethylene
PECVD	Plasma enhanced chemical vapor deposition
PIB	Polyisobutylene
PLA	Poly-lactic acid
PP	Polypropylene
PTFE	Polytetrafluoroethylene
PVD	Physical Vapour deposition
QCM	Quartz crystal microbalance
RF	Radio frequency
RMS	Root mean square
SAXS	small angle X-ray scattering
SCCM	Standard cubic centimeters per minute
SE	Secondary electrons
SEM	Scanning electron microscopy
UHV	Ultra-high vacuum
UV-Vis	Ultraviolet-visible spectroscopy
XPS	X-ray photoelectron spectroscopy

List of Tables

List of Figures

Appendix A

Navier-Stokes Equations for Viscous Flow

Governing equations (in conservation form) for an unsteady, three-dimensional, compressible, viscous flow are:

Continuity equation

$$\frac{\partial \rho}{\partial t}+\nabla \cdot(\rho \cdot \vec{v})=0 \quad \textbf{(A.1)}$$

Momentum equations

x-component

$$\frac{\partial(\rho u)}{\partial t}+\nabla \cdot(\rho u \cdot \vec{v})=\frac{-\partial p}{\partial x}+\frac{\partial \tau_{xx}}{\partial x}+\frac{\partial \tau_{yx}}{\partial y}+\frac{\partial \tau_{zx}}{\partial z}+\rho f_x \quad \textbf{(A.2)}$$

y-component

$$\frac{\partial(\rho v)}{\partial t}+\nabla \cdot(\rho v \cdot \vec{v})=\frac{-\partial p}{\partial y}+\frac{\partial \tau_{xy}}{\partial x}+\frac{\partial \tau_{yy}}{\partial y}+\frac{\partial \tau_{zy}}{\partial z}+\rho f_y \quad \textbf{(A.3)}$$

z-component

$$\frac{\partial(\rho w)}{\partial t}+\nabla \cdot(\rho w \cdot \vec{v})=\frac{-\partial p}{\partial z}+\frac{\partial \tau_{xz}}{\partial x}+\frac{\partial \tau_{yz}}{\partial y}+\frac{\partial z}{\partial z}+\rho f_z \quad \textbf{(A.4)}$$

Where f_i is a fluid element body force per unit mass for a specific coordinate component, τ_{ij} is a shear stress component.

Energy equation

$$\frac{\partial}{\partial t}\left[\rho\left(e+V^2\right)\right]+\nabla \cdot\left[\rho\left(e+\frac{V^2}{2}\right)\vec{v}\right]=\rho \dot{q}+\frac{\partial}{\partial x}\left(k\frac{\partial T}{\partial x}\right)+\frac{\partial}{\partial y}\left(k\frac{\partial T}{\partial y}\right)+\frac{\partial}{\partial z}\left(k\frac{\partial T}{\partial z}\right. \quad \textbf{(A.5)}$$

Where $\vec{f}$ is a fluid element body force per unit mass, τ_{ii} is a normal stress component (e.g. τ_{xx}), τ_{ij} is a shear stress component, $\dot{q}$ is a heat transferred, T is the temperature, e is the internal energy per unit mass due to random molecular motion, $\frac{V^2}{2}$ is a kinetic energy per unit mass due to fluid translation motion.